ARL-TR-9296 ● SEP 2021

Hybrid Experimental Modeling Computational (HEMC) Skullcap Simulation: Elemental to Layer Simplification and Application to Microstructural Stochasticity

by Stephen L Alexander, Timothy Baumer, Brian Fagan and Tusit Weerasooriya

NOTICES

Disclaimers

The research reported in this document was performed in connection with contract/instrument W911QX-16-D-0014 with the Combat Capabilities Development Command (DEVCOM) Army Research Laboratory.

The findings in this report are not to be construed as an official Department of the Army position unless so designated by other authorized documents. The views and conclusions contained in this document are those of SURVICE Engineering Company and the DEVCOM Army Research Laboratory.

ARL-TR-9296 ● SEP 2021

Hybrid Experimental Modeling Computational (HEMC) Skullcap Simulation: Elemental to Layer Simplification and Application to Microstructural Stochasticity

Stephen L Alexander and Timothy Baumer
SURVICE Engineering Company

Brian Fagan and Tusit Weerasooriya
Weapons and Materials Research Directorate,
DEVCOM Army Research Laboratory

REPORT DOCUMENTATION PAGE	*Form Approved* *OMB No. 0704-0188*

1. REPORT DATE *(DD-MM-YYYY)* September 2021	**2. REPORT TYPE** Technical Report	**3. DATES COVERED (From - To)** 12/1/20–03/31/21

4. TITLE AND SUBTITLE Hybrid Experimental Modeling Computational (HEMC) Skullcap Simulation: Elemental to Layer Simplification and Application to Microstructural Stochasticity	**5a. CONTRACT NUMBER** W911QX-16-D-0014
	5b. GRANT NUMBER
	5c. PROGRAM ELEMENT NUMBER
6. AUTHOR(S) Stephen L Alexander, Timothy Baumer, Brian Fagan, and Tusit Weerasooriya	**5d. PROJECT NUMBER**
	5e. TASK NUMBER
	5f. WORK UNIT NUMBER
7. PERFORMING ORGANIZATION NAME(S) AND ADDRESS(ES) DEVCOM Army Research Laboratory ATTN: FCDD-RLW-TB Aberdeen Proving Ground, MD 21005	**8. PERFORMING ORGANIZATION REPORT NUMBER** ARL-TR-9296
9. SPONSORING/MONITORING AGENCY NAME(S) AND ADDRESS(ES)	**10. SPONSOR/MONITOR'S ACRONYM(S)**
	11. SPONSOR/MONITOR'S REPORT NUMBER(S)

12. DISTRIBUTION/AVAILABILITY STATEMENT

Approved for public release: distribution unlimited.

13. SUPPLEMENTARY NOTES

ORCID ID: Tusit Weerasooriya, 0000-0003-3299-2166

14. ABSTRACT

During impact on Soldiers' heads, such as in behind-helmet blunt trauma (BHBT), skull fractures can indicate injury. We previously developed a concept for simulating skull fracture with an Elemental Approach using microstructure-inspired mechanism-based (MIMB) method, and simulated fracture patterns matched well with the experiment. However, application to BHBT simulations was hindered by the necessary use of relatively small elements and the deterministic nature of the simulations. Here, possible solutions were evaluated. The Three-Layer Approach represented the skull by a sandwich structure—defined previously as 70% bone volume fraction (BVF) thresholds—near impact and by a single homogeneous material elsewhere. New layering and improved failure algorithms were developed to aid BHBT researchers implementing this approach. Stochasticity was introduced by randomly redistributing element-BVF values within layers, providing a high-throughput method for approximating biovariability. The Three-Layer Approach satisfactorily represented the experiment's load-displacement response, but skull failure occurred by different mechanisms dominating the final failure. In contrast, hybrid Three-Layer–Elemental simulations reasonably approximated both deformation and failure response, including the final dominant mechanism of failure, whenever the inner table was represented by the Elemental Approach. Initiated back-surface crack patterns from different stochasticities showed the method can evaluate probabilities associated with brain-injury scenarios from cracking.

15. SUBJECT TERMS

skull fracture, skull mechanics, skull failure, back-face deformation, behind-helmet blunt trauma, head simulation, head impact, head injury

16. SECURITY CLASSIFICATION OF:			**17. LIMITATION OF ABSTRACT**	**18. NUMBER OF PAGES**	**19a. NAME OF RESPONSIBLE PERSON** Tusit Weerasooriya
a. REPORT Unclassified	**b. ABSTRACT** Unclassified	**c. THIS PAGE** Unclassified	UU	93	**19b. TELEPHONE NUMBER (Include area code)** (410) 652-9450

Contents

List of Figures

List of Tables

Acknowledgments

We gratefully acknowledge the assistance of Richard Becker of DEVCOM Army Research Laboratory. His suggestion of deleting elements based on strain rate allowed us to continue simulations beyond local failures up to the catastrophic failure. In addition, he provided an in-depth, critical, constructive secondary technical review, which greatly improved the report and the conclusions.

1. Introduction

1.1 Background: Recent Approaches to Model Skull Fracture

Head-protection design and evaluation involves determining whether Soldiers' injuries would have occurred under a certain set of impact conditions. For example, behind-helmet blunt trauma (BHBT) occurs when the inner surface of the helmet deforms under nonpenetrating impact and strikes the head. BHBT researchers need a means of assessing whether a given set of forces acting on a particular helmet configuration would have injured the Soldier. One of the most commonly researched types of head injury is traumatic brain injury (TBI). Determination of TBI would ideally be made by comparing measurements of stress and strain in the brain against a set of validated thresholds at the cellular or tissue scale. However, currently such multiaxial, comprehensive detailed measurements at the cellular or tissues scale are often not available to the BHBT researcher. Even if they were, the corresponding injury thresholds are still being researched without a definitive set available at this time (e.g., Abderezaei et al. 2019; Hajiaghamemar et al. 2020). Meanwhile, skull fracture serves as another prominent indicator of head injury that is a more readily identifiable, practical indicator. Furthermore, skull fracture may have implications for injuries that are not specific to injury mechanisms in the brain, such as hemorrhaging due to soft-tissue damage caused by the fracture, which can produce serious outcomes. Therefore, the ability to predict skull fracture can provide a tool to evaluate the effectiveness of current and future head-protection concepts.

Modeling fracture under multiaxial stress-states of even the most common engineering materials is an ongoing area of research. This task is further complicated in a complex heterogeneous biomaterial such as the skull. One challenge is the large range of porosity within a single skull specimen. The porosity varies from the inner to the outer surface as a Gaussian bell-shaped curve (Alexander et al. 2019). This heterogeneity has significant implications on skull failure, since failure of skull bone has been shown to exponentially scale with the bone volume fraction (BVF), the opposite measure of porosity (Boruah et al. 2017; Alexander et al. 2020a; Brown et al. 2021). Another challenge is biovariability: the significant variation in skull microstructure observed among individuals.

We previously proposed these challenges could be overcome with microstructurally inspired mechanism-based (MIMB) failure models, which modeled failure at the local, element-by-element scale (Alexander and Weerasooriya 2021; Weerasooriya and Alexander 2021). This approach, referred to as the Elemental Approach, was most recently demonstrated in modeling and experimentally indenting a human skull specimen (Weerasooriya and Alexander 2021). The so-called “skullcap” specimen was purposely chosen to be at an intermediate length-scale (between uniaxial and simple-shear coupon, and full skull specimens) to aid in development of hybrid experimental modeling computational (HEMC) concept. An overview of the different length-scales of human skull specimens was provided in Table 1 of Gunnarsson et al. 2021a, which details the advantages and disadvantages of each length-scale for purposes of comprehensive model development. The simulation implementing the Elemental Approach with MIMB failure thresholds well-matched the failure patterns observed experimentally.

1.2 Problem Addressed by Current Study and Proposed Solutions

There were at least two limitations to implementing our previous Elemental Approach in BHBT simulations involving the entire head. The first was that the mesh of the skullcap specimen consisted of >200,000 elements for a part of the skull measuring only approximately 80 mm × 70 mm on the outer surface. We did not use larger element configuration because element size will not be in the order of pores (Weerasooriya and Alexander 2021), but this element density was likely necessary with the Elemental Approach for the elements to be sufficiently small to model the BVF variation within the skull. However, using similar-sized elements in BHBT simulations of the whole skull would result in a very large number of elements in the skull alone, which is very computationally expensive. In addition, the element size could not be increased too much while still using the Elemental Approach. Increasing the element size would increase the volume over which the BVF was averaged when calculating the BVF of the element, thereby coarsening the averaging. If the size was increased too much, the porous distribution within the skull would no longer be accurately represented by the element-BVF assignments.

Here, a less computationally expensive method was evaluated. The approach is referred to as the Three-Layer Approach. An action zone (AZ) within the skull mesh is identified near the point of indentation/impact (POI). In the AZ, the skull is represented with three layers from the outer to the inner surface, modeling the outer table (OT), mid-diploe (MD), and inner table (IT) of the skull. Away from the AZ, the skull is represented as a single continuous layer with appropriate homogenized mechanical properties. Elements within the AZ can be much larger than in the Elemental Approach as long as there is a sufficient number of elements through the thickness so as to divide the thickness into the three layers. Elements outside the AZ can be yet larger. Thus, the Three-Layer Approach advantageously combines previous methods of modeling the skull either as a single homogeneous material (e.g., Tse et al. 2014) or as a three-layer sandwich structure (e.g., Deck and Willinger 2008; Cotton et al. 2016; Lozano-Mínguez et al. 2018; Ptak et al. 2018).

We previously demonstrated the Three-Layer Approach, but only focused on the initial linear response of the skull bone at that time (Alexander et al. 2020b). In addition, the implementation of the layering in the skull mesh was completed by a time- and labor-intensive process, which would discourage the adoption of such an approach in BHBT simulations of the whole skull. More automated preprocessing methods would make the Three-Layer Approach a practical solution.

The second limitation to implementing the Elemental Approach in BHBT simulations was that skullcap simulation represented a single specimen from a particular donor. In particular, the geometry of the mesh and the element-BVF assignments in the skullcap simulation were based on representing a single skull specimen and the distribution of pores within it. However, BHBT simulations must be applicable to the broader Soldier community. Simulations with details pertaining to a single specimen/donor are not directly applicable. A method of accounting for biovariability is required. The current study proposes the effect of biovariability in the skull microstructure can be studied by keeping the geometry of the skull mesh unchanged but then randomly assigning a known distribution of BVF values—in this case based on a single specimen, but ideally based on a population—among the elements.

1.3 Goals and Outline of this Work

This study aimed to transition the skullcap simulation from the detailed Elemental Approach we had previously developed to the Three-Layer Approach, to be more easily implementable in large-scale simulations such as in BHBT research. Then, biovariability was simulated by randomly redistributing the element-BVF assignments among various subsets of elements in the Elemental and Three-Layer Approaches. Updated computational methods were also developed to enable the Elemental Approach to more closely match the experimental response, compared with our previous studies.

First, Section 2 briefly overviews the skullcap simulation using the Element Approach from our previous study. Next, Section 3 details the computational methods developed in the process of accomplishing the above-mentioned goals. Section 4 describes the application of these computational methods to simulating the response of the skull: the previous skullcap simulation using the Elemental Approach was updated, the simulation was transitioned to the Three-Layer Approach, and biovariability was simulated. Finally, Section 5 compares the

Elemental with the Three-Layer Approach and discusses the effects of randomization, and conclusions are drawn in Section 6.

2. Background of Finite Element (FE) Simulations of Human Skull Specimens in this Study

The simulations described in this document were based on a previously published FE simulation of the quasi-static indentation of a human skullcap specimen. The indentation experiment was previously documented with details regarding the specimen source, extraction, geometry, loading conditions, and microstructural imaging (Gunnarsson et al. 2021b). The original FE simulation has likewise been documented in full (Weerasooriya and Alexander 2020) and is referred to in the present study as the Original Skullcap Simulation (OSS). For clarity, a brief overview of the FE simulation is provided here; the reader is referred to the original publications for information on the experiment and for additional information on the OSS.

Numerical analysis was completed in Abaqus Explicit (Dassault Systèmes Simulia Corp; Johnston, Rhode Island). The mesh of the skullcap specimen was developed in collaboration with Materialise USA LLC using the Mimics Innovation Suite (MIS; Materialise USA LLC, Plymouth, Michigan). The skullcap specimen was micro-computed-tomography (CT) scanned at an isotropic voxel resolution of 27 μm^3, both prior to the indentation/impact experiment (pretest) and after the experiment (post-test). The skullcap mesh was constructed in MIS using the geometry of the specimen from the pretest images and approximately 230 k of 4-noded, linear tetrahedral elements (C3D4 in Abaqus notation). Figure 1 shows the skullcap mesh. As evident in the cross section (Fig. 1B), the skullcap specimen had a dome shape with the outer surface (nearest the skin) on the top of the dome and the inner surface (nearest the brain) on the bottom of the dome. The inner surface is referred to as the specimen back face (BF). The mesh was selectively refined near the point of indentation/impact (POI), which was nominally located at the apex of the dome structure on the outer surface. Element side length increased as a function of distance from the POI (Fig. 1B).

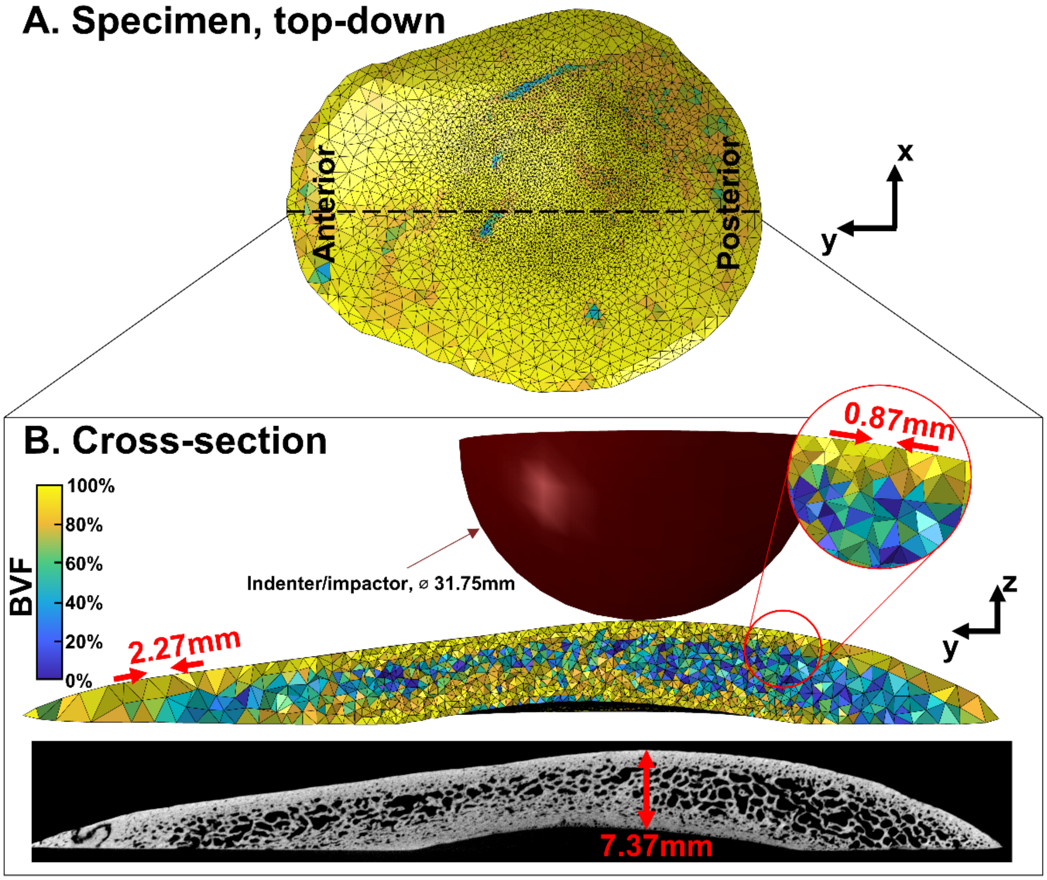

Fig. 1 **Skullcap mesh used in previous skullcap simulation (Weerasooriya and Alexander 2021). All skullcap elements are color-coded by BVF according to scale shown in B. (A) Top-down view showing outer surface of skullcap, which would be nearest to skin. (B) Cross-sectional view comparing BVF of elements with corresponding pretest micro-CT image and showing POI. In micro-CT image, grey/white represents bone. Position of cross section within skull is indicated in (A) by dashed line across anterior–posterior axis.**

In addition, MIS was used to map each element in the FE mesh to the micro-CT data set to calculate the BVF of the physical space the element represented, $f_{BV,0}$. This value of $f_{BV,0}$ was used to calculate the microstructure-dependent material properties of each element. The mass density (ρ), Young's modulus (E) and failure strengths in compression (σ_f^c), tension (σ_f^t), and shear (σ_f^s) were calculated as shown in Table 1. These material properties of the element were then used to calculate the stress of the element according to a custom-written user subroutine: VUMAT in Abaqus notation. The VUMAT algorithm used in the OSS was fully described in the previous publication and is referred to here as VUMAT_A. Figure 2 is reproduced here to summarize VUMAT_A.

Table 1 BVF-dependent properties assigned to skullcap elements in previous skullcap simulation (OSS)

Property	BVF relationship	Units
Young's modulus	$E = 3.0 \cdot (f_{BV,0})^{1.6}$	GPa
Density	$\rho_0 = 1.8 \cdot (f_{BV,0})$	g/cm^3
Compressive failure	$\sigma_f^c = 175.0 \cdot (f_{BV,0})^{2.0}$	MPa
Tensile failure	$\sigma_f^t = 269.4 \cdot (f_{BV,0})^{2.0}$	MPa
Shear failure	$\sigma_f^s = 150.0 \cdot (f_{BV,0})^{2.0}$	MPa

Note: Additional information and discussion are in Weerasooriya and Alexander (2021), which details the iterative process for deriving these parameters and compares their values with literature.

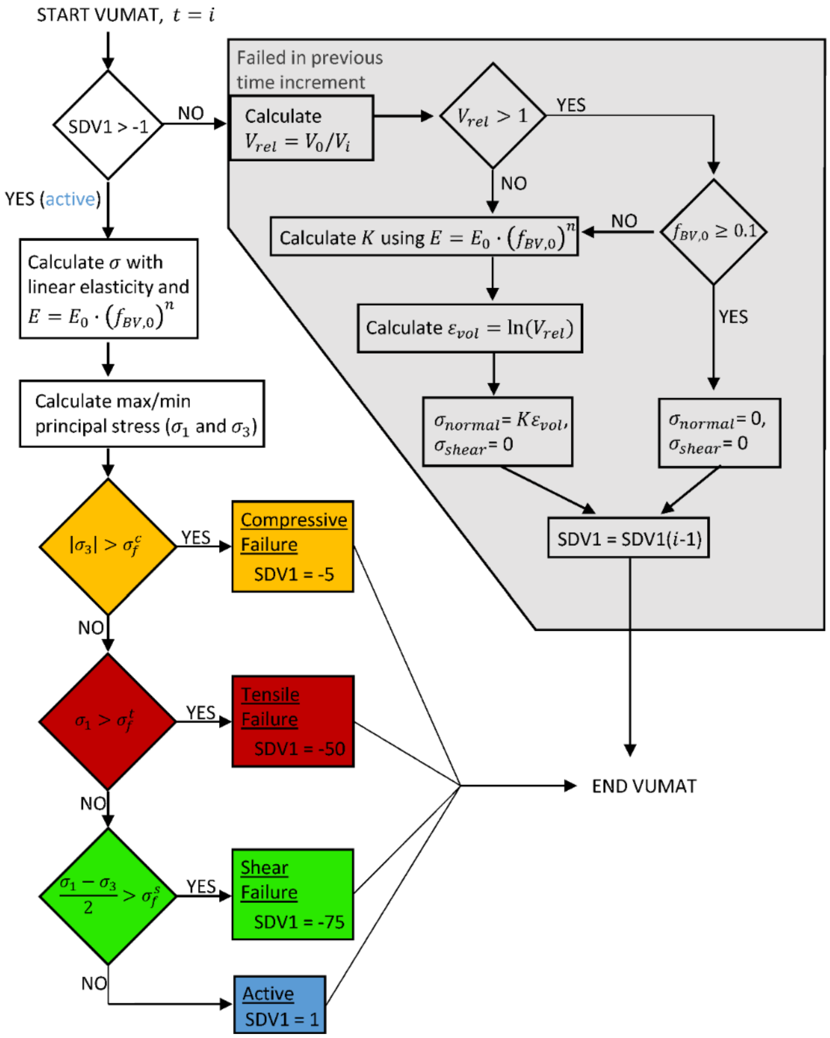

Fig. 2 Overview of VUMAT_A algorithm used to calculate stress of skullcap elements in OSS; reproduced from Weerasooriya and Alexander (2021)

The remaining preprocessing tasks were executed in the Abaqus pre-/post-processing environment (Abaqus CAE). The backing plate was meshed using reduced-order 8-node brick elements (C3D8R in Abaqus notation) and was assigned elastic material properties of aluminum. Plate displacement in all directions was constrained at four locations near the corners of the plate, modeling the experimental setup where the plate was supported by four through-thickness bolts near the corners. The indenter/impactor was modeled as a rigid solid hemisphere with diameter 31.75 mm, as shown in Fig. 1. The indenter/impactor was constrained in all degrees of freedom apart from displacement in the z-direction, which was specified to increase from 0 to 3.3 mm in 10 ms.

The skullcap mesh was imported into Abaqus CAE where it was positioned over the backing plate, and the indenter/impactor was positioned to the POI. As shown in Fig. 3, the backing plate had a hole over where the skullcap was positioned. The hole served in the experimental setup as a viewing port, enabling the specimen BF to be imaged during indentation/impact. These BF images were used to calculate the out-of-plane displacement, corresponding to displacement in the z-direction based on the coordinate system of Fig. 3. This out-of-plane displacement is referred to as the back-face displacement (BFD). In the simulations, the Abaqus formulation for hard general contact was used for all interacting bodies, with a friction coefficient of 0.1.

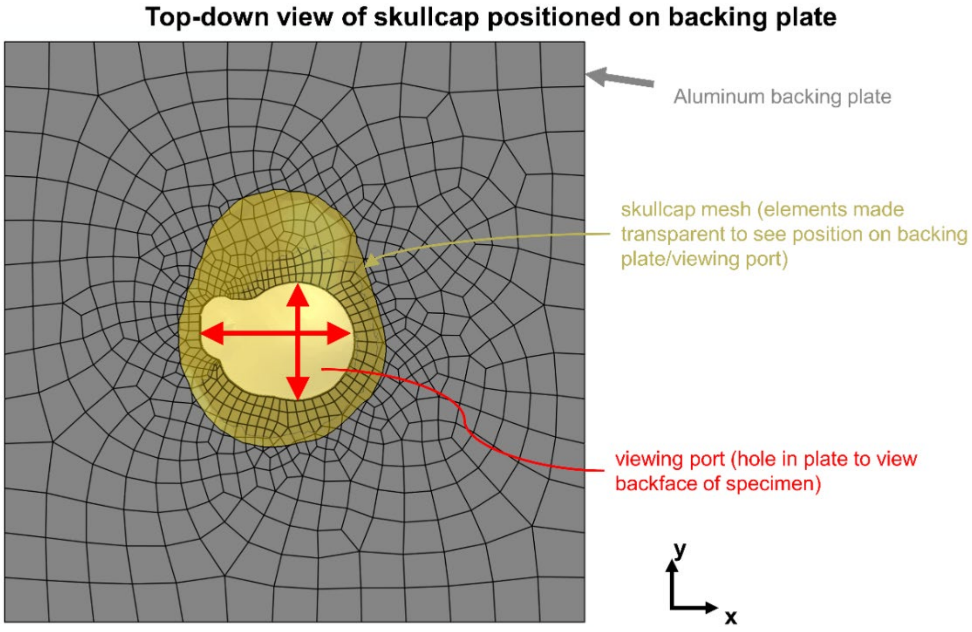

Fig. 3 **Top-down view of backing plate with skullcap positioned over the viewing port; indenter/impactor is not shown, and skullcap is made semitransparent so as to see relative position on the backing plate and viewing port. Reader is referred to original publications for additional information on the experiment (Gunnarsson et al. 2021b) or simulation (Weerasooriya and Alexander 2021).**

3. Updated FE Methods

This section details the computational methods that were developed to accomplish the goals of the present study. First are presented methods for dividing the skullcap mesh into regions of interest (Section 3.1), segregating an AZ under/near the POI from the rest of the mesh and then further identifying layers within the AZ based on relative thickness. The remaining sections (3.2 and 3.3) describe updates to the VUMAT algorithm to improve the load-displacement response of the simulation. The updated VUMAT is referred to as VUMAT_B. Section 4 describes the application of these methods and the VUMAT_B.

3.1 Dividing Skull Mesh into Regions of Interest

This section describes algorithms developed to automatically group elements of the skullcap mesh based on their position. These algorithms were used to transition from the Elemental Approach to the Three-Layer Approach, as is described in Section 4.

3.1.1 Common Terms and Background Information

The x, y, z coordinate system was defined with the backing plate in the x–y plane and the direction of indentation/impact in the z-direction, as illustrated in Figs. 1 and 3. A node was defined by two attributes: its **nodal ID** and **nodal coordinates**. The nodal ID was the unique identification number of the node. The nodal coordinates defined the x, y, and z position of the node within the mesh. For the purposes of the algorithms described here, the term nodal coordinates always referred to the x, y, and z position of the node within the undeformed mesh at the start of the simulation (undeformed configuration).

A **node set** referred to a collection of nodes. The nodes within the node set were identified by their nodal IDs.

The elements considered in this report were first-order, 4-noded tetrahedral elements (C3D4 in Abaqus notation). Such elements were defined by two attributes: **element number** and **nodal connectivity**. The element number was the unique identification number of the element. The nodal connectivity specified the nodal IDs of the four vertices at the four corners of the tetrahedral.

An **element set** was a collection of elements. Analogously to the node set, the elements within the element set were identified by their element numbers.

The algorithms described here operated in an object-oriented framework. Element objects were constructed from the FE input file (.inp in Abaqus notation). These objects were defined by their element number and nodal connectivity. They were also assigned additional attributes as needed by the various algorithms, described as follows.

3.1.2 Algorithm for Segregating Impact Zone from Far Zone (FZ)

First, the centroid of each element was calculated based on the nodal coordinates of the element. The x, y, and z coordinates of the centroid of Element E are referred to here as E_X^C, E_Y^C, and E_Z^C.

Next, the node on the skullcap nearest to the POI was identified using the preprocessing/visualization software (Abaqus CAE). This node are referred to here as Node P, with x, y, and z coordinates of P_X, P_Y, and P_Z.

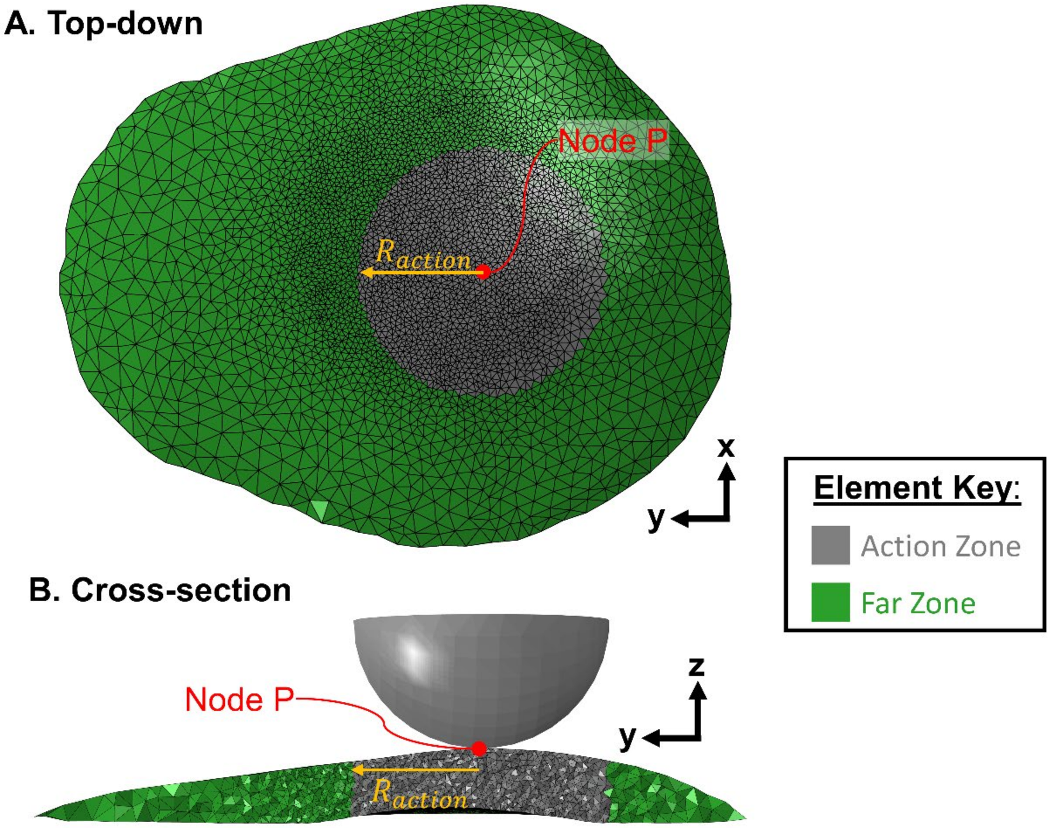

Fig. 4 Dividing skullcap into AZ under POI, and FZ farther away from POI. Node P is node of skullcap mesh closest to POI. AZ consisted of elements falling within region of cylinder with long axis in z-direction and radius of R_{action} in x–y plane.

Then, for each element, the distance in the x–y plane from the centroid of the element to Node P was calculated. This distance is referred to here as d_{XY}. For a given element E, this distance was calculated as

$$d_{XY} = \sqrt{(E_X^C - P_X)^2 + (E_Y^C - P_Y)^2} \tag{1}$$

The AZ was defined by an impact radius in the x–y plane, R_{action}. An element was considered to be in the AZ if $d_{XY} \leq R_{action}$. If this condition was not met, the element was considered to be in the FZ. For purposes of the skullcap simulations described here, R_{action} was set to 16 mm. Figure 4 shows the AZ and FZ elements in the mesh.

3.1.3 Algorithm for Automatically Dividing Skull Mesh into N-Number of Layers within AZ

An algorithm was developed to automatically divide the skull within the AZ into a user-defined number of layers, N. The layers are referred to here with the convention that Layer 1 was on the outer surface and Layer N was on the inner surface. The algorithm was only applied to the elements within the AZ for the following reasons. The outer and inner surfaces of the skull were intact within the AZ, under the POI. In the skullcap specimen considered here, the outer and inner surfaces were not intact farther away from the POI, near the perimeter of the specimen. In addition, the AZ was naturally the region of the skull mesh where refinement was desired to increase the biofidelity of the simulated response.

Preliminary steps were executed prior to running the algorithm. The preprocessing/visualization software was used to construct a node set containing all of the nodes on the outer surface. This node set is referred to here as the Outer Node Set. The node set was created in Abaqus CAE by selecting a single node on the outer surface and allowing the program to automatically populate the node set with all of the nodes found within a user-specified angle from the originally selected node. Likewise, a node set was also constructed containing all of the nodes on the inner surface, and this node set is referred to as the Inner Node Set.

3.1.3.1 Classification for Elements Touching Outer/Inner Surfaces

The first step within the algorithm was identifying elements that touched the outer or inner surfaces. These elements were identified as satisfying the condition of having one or more nodes within the Inner or Outer Node Sets. This condition was evaluated for each element using the `intersect1d` function of Numpy, which finds common members of two input arrays (https://numpy.org/doc/stable/reference/generated/numpy.intersect1d.html). The `intersect1d` function was used to find common members between the Outer Node Set and the nodes of the element. If there was at least one common member (node), the element was classified as belonging to Layer 1 (defined as closest to the outer surface). If there were no common members, then the `intersect1d` function was next used to find common members between the Inner Node Set and the nodes of the element. If there was at least one common node between them, the element was classified as belonging to Layer N (defined as closest to the inner surface). Elements that did not have a single node in either the Outer Node Set or the Inner Node Set were put into an element set referred to here as Interior Element Set to be classified according to the secondary classification.

3.1.3.2 Classification for All Other Elements (Not Touching Outer/Inner Surfaces)

The secondary classification was applied to the elements in the Interior Element Set identified previously. The description of this classification is written in terms of any given element in the Interior Element Set, Element E, and was applied for all of the elements within the Interior Element Set. An illustration of the process is provided in Fig. 5. For Element E, the node in the Outer Node Set nearest to the centroid of the element was identified. This node is referred to here as Node Outer, with coordinates O_X, O_Y, and O_Z. Likewise, the node in the Inner Node Set nearest to the centroid of the element was identified, and is referred to here as Node Inner with coordinates I_X, I_Y, and I_Z.

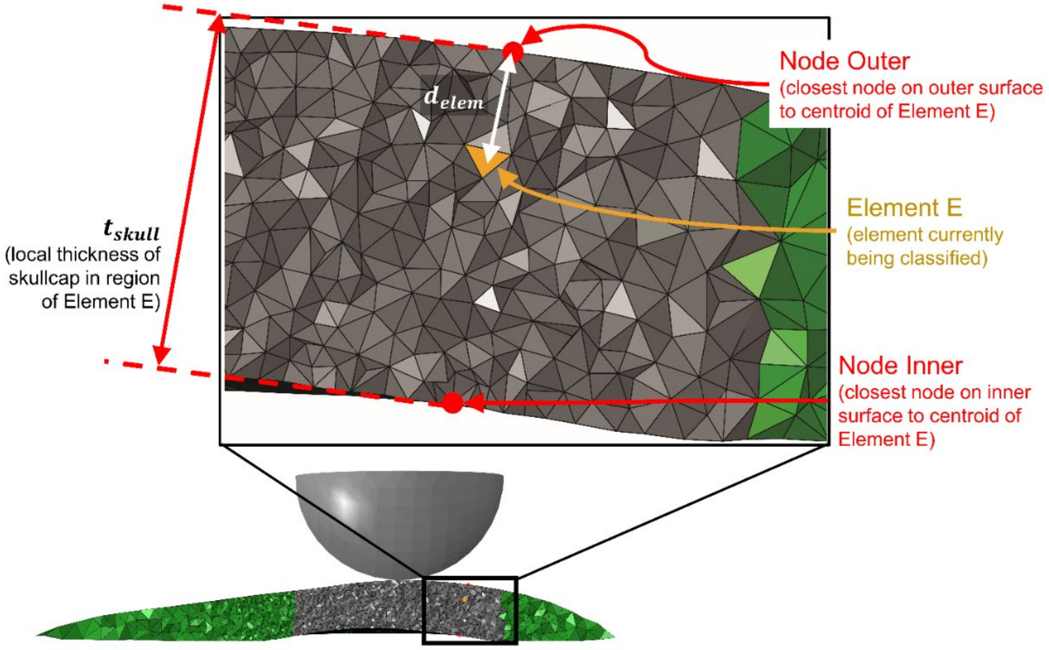

Fig. 5 Process of determining normalized depth of an interior element, marked as Element E, within thickness of the skullcap. Normalized depth of element was calculated as d_{elem}/t_{skull}.

Nodes Outer and Inner were identified using the scipy.spatial.cKDTree class from SciPy (https://docs.scipy.org/doc/scipy/reference/generated/scipy.spatial.cKDTree.html). This class was used to produce one KDTree from the nodal coordinates of the nodes in the Outer Node Set and another KDTree from the nodal coordinates of the nodal coordinates of the nodes in the Inner Node Set. The query method of these KDTrees was then used to find the nearest nodes to the centroid of Element E.

Table 2 Example of assigning an element to a layer based on normalized depth of element (d_{elem}^{norm}). Example is for mesh with 10 layers of equal thickness.

Value of d_{elem}^{norm}	Layer assignment
$0 \le d_{elem}^{norm} < 0.1$	1
$0.1 \le d_{elem}^{norm} < 0.2$	2
$0.2 \le d_{elem}^{norm} < 0.3$	3
$0.3 \le d_{elem}^{norm} < 0.4$	4
$0.4 \le d_{elem}^{norm} < 0.5$	5
$0.5 \le d_{elem}^{norm} < 0.6$	6
$0.6 \le d_{elem}^{norm} < 0.7$	7
$0.7 \le d_{elem}^{norm} < 0.8$	8
$0.8 \le d_{elem}^{norm} < 0.9$	9
$0.9 \le d_{elem}^{norm} < 1.0$	10

Next, the local thickness of the skullcap in the region of Element E, t_{skull}, was approximated* as the 3-D Euclidean distance between Node Outer and Node Inner:

$$t_{skull} = \sqrt{(O_X - I_X)^2 + (O_Y - I_Y)^2 + (O_Z - I_Z)^2} \tag{2}$$

Then, the distance from the centroid of Element E to Node Outer was calculated as d_{elem}. The calculation was based on the centroid of Element E, which had coordinates of E_X^C, E_Y^C, and E_Z^C:

$$d_{elem} = \sqrt{(O_X - E_X^C)^2 + (O_Y - E_Y^C)^2 + (O_Z - E_Z^C)^2} \tag{3}$$

The relative position of Element E within the skull was characterized by the normalized depth, d_{elem}^{norm}, of its centroid:

$$d_{elem}^{norm} = d_{elem}/t_{skull} \tag{4}$$

Finally, d_{elem}^{norm} was used to classify the element according to the number of user-specified layers and the relative thickness of each layer. An example for 10 layers of equal thickness is presented in Table 2.

---

* If the outer and inner surfaces are not parallel, this method of finding t_skull may not give the exact thickness and may introduce a small error.

3.2 Automatic Removal of Elements Based on Strain Rate

The simulation iterations described in Weerasooriya and Alexander (2021) were prone to have severely distorted elements. In some cases, elements became so distorted that Abaqus ended the simulation early. To avoid the simulation from aborting early, the updated VUMAT (referred to here as VUMAT_B) included an additional subroutine to delete elements if the strain rate of the element exceeded 1×10^7. The strain rate of an element at time increment *i* was calculated as

$$\dot{\varepsilon}_i = \sqrt{{}^{2}/_{3}\, \dot{\varepsilon} : \dot{\varepsilon}} \tag{5}$$

The right-hand side of Eq. 5 was calculated from the strain-increment tensor of the element ($\Delta\varepsilon_{xx}$, $\Delta\varepsilon_{yy}$, $\Delta\varepsilon_{zz}$, $\Delta\varepsilon_{xy}$, $\Delta\varepsilon_{xz}$, $\Delta\varepsilon_{yz}$) and the time-increment size, Δt, as

$$\dot{\varepsilon}_i = \frac{1}{\Delta t}\sqrt{\frac{2}{3}\left(\Delta\varepsilon_{xx}^2 + \Delta\varepsilon_{yy}^2 + \Delta\varepsilon_{zz}^2 + 2\left(\Delta\varepsilon_{xy}^2 + \Delta\varepsilon_{yz}^2 + \Delta\varepsilon_{xz}^2\right)\right)} \tag{6}$$

3.3 Algorithm Preventing Artificial Load Drops Due to Cascades of Tensile Failure in FE Simulation of Skull Loading

3.3.1 Background on the Problem

The stress of each element in the skullcap simulations was calculated using a custom-written user subroutine (VUMAT in Abaqus). The VUMAT algorithm used in the OSS (VUMAT_A) caused the simulations to be prone to large drops in the force, which were unrealistic. An example from Weerasooriya and Alexander (2020) is provided in Fig. 6 to illustrate this problem. The problem was analyzed by tracking the number of elements that failed by each mechanism during the simulation. This analysis indicated the force drops were due to many high-BVF elements failing in tension within a relatively short time. Therefore, the algorithm was updated to prevent these cascades of elements failing in tension.

In VUMAT_A, the stress state of the element was calculated prior to failure using the relationship between BVF and Young's modulus shown in Table 1. The element was considered to have failed in tension during the time increment $t = t_f^t$ if the maximum principal stress of the element, σ_1, exceeded the tensile failure stress of the element, σ_f^t (red diamond in the VUMAT_A flowchart, Fig. 2). The value of σ_f^t was also element-BVF-specific and was calculated using the relationship shown in Table 1.

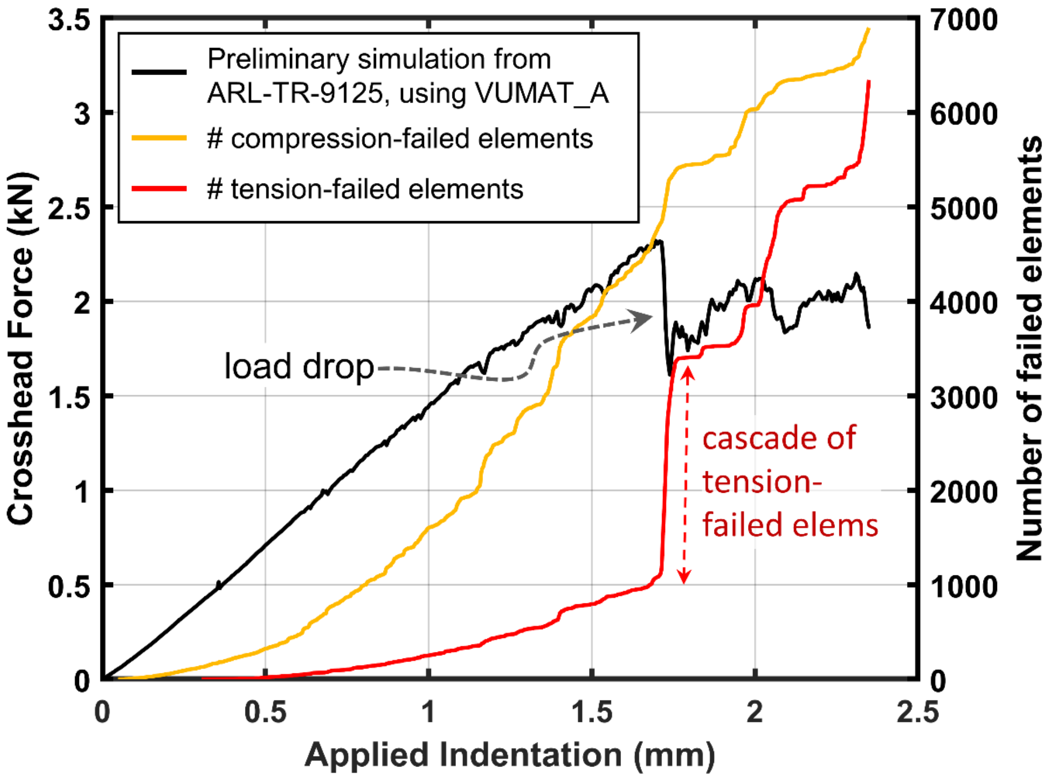

Fig. 6 Example of problem of large load drops caused by cascade of elements failing in tension when using VUMAT_A; adapted from Fig. A-3 in Weerasooriya and Alexander (2020).

An element having failed in tension would only start to be treated as a failed element in the next time increment, $t_f^t + 1$. Elements that had previously failed and were subsequently in a state of tension were assigned a stress of zero, provided that the BVF was greater than 10%. An element that had failed in tension was likely to still be in a state of tension for $t_f^t + 1$. Therefore, the method resulted in high-BVF elements that failed in tension being assigned zero stress for $t_f^t + 1$. This particular category of elements is referred to here as tension-failed-high-BVF (TFHB) elements.

3.3.2 Solution

The hypothesis was that immediately setting the stress of the TFHB elements to zero at $t = t_f^t + 1$ was causing a chain reaction of many elements to fail within a short time period, a cascade of element failures. It was further hypothesized these cascades could be mitigated if the stress of a TFHB element was gradually reduced to zero over many time increments rather than over a single time increment (some of the specialized advanced codes include some variations of this concept). The updated algorithm in VUMAT_B implemented this hypothesis by decrementing the Young's modulus of the failed element over a period of time after the element had exceeded its tensile failure strength. The changes are summarized in Table 3 and explained as follows.

Table 3 Comparing calculation of Young's modulus in TFHB elements in previous and current VUMATs

Time increments	VUMAT_A (no algorithm for load drops)	VUMAT_B (implementing algorithm to avoid load drops)
Before stress reaches σ_f^t $(t < t_f^t)$	$E = E_0 \cdot (f_{BV,0})^n$	$E = E_0 \cdot (f_{BV,0})^n$
Increment when stress reaches σ_f^t $(t = t_f^t)$	$E = E_0 \cdot (f_{BV,0})^n$	$E = DE_0 \cdot (f_{BV,0})^n$, where D is calculated according to Eq. 8.
Subsequent increments $(t = t_i > t_f^t)$	$E = 0$	$E = D_i E_0 \cdot (f_{BV,0})^n$ where D_i is calculated as $D_i = A \cdot D_{i-1}$

In the updated algorithm, for time $t \geq t_f^t$, the Young's modulus of a TFHB element was set to

$$E = DE_0 \cdot (f_{BV,0})^n \tag{7}$$

In Eq. 7, D corresponded to a damage parameter. The damage parameter changed as a function of time and σ_1 as described in the following.

3.3.2.1 Stress at the Time of Failure ($t = t_f^t$)

The damage parameter was calculated in the time increment $t = t_f^t$ as

$$D(t = t_f^t) = \begin{cases} \frac{\sigma_R - \sigma_1}{\sigma_R - \sigma_f^t}, & \text{if } \sigma_1 \leq \sigma_R \\ 0, & \text{otherwise} \end{cases} \tag{8}$$

In Eq. 8, σ_R was an additional buffer stress threshold calculated analogously to σ_f^t by also being a function of the BVF:

$$\sigma_R = \sigma_{R,0} \cdot (f_{BV,0})^2 \tag{9}$$

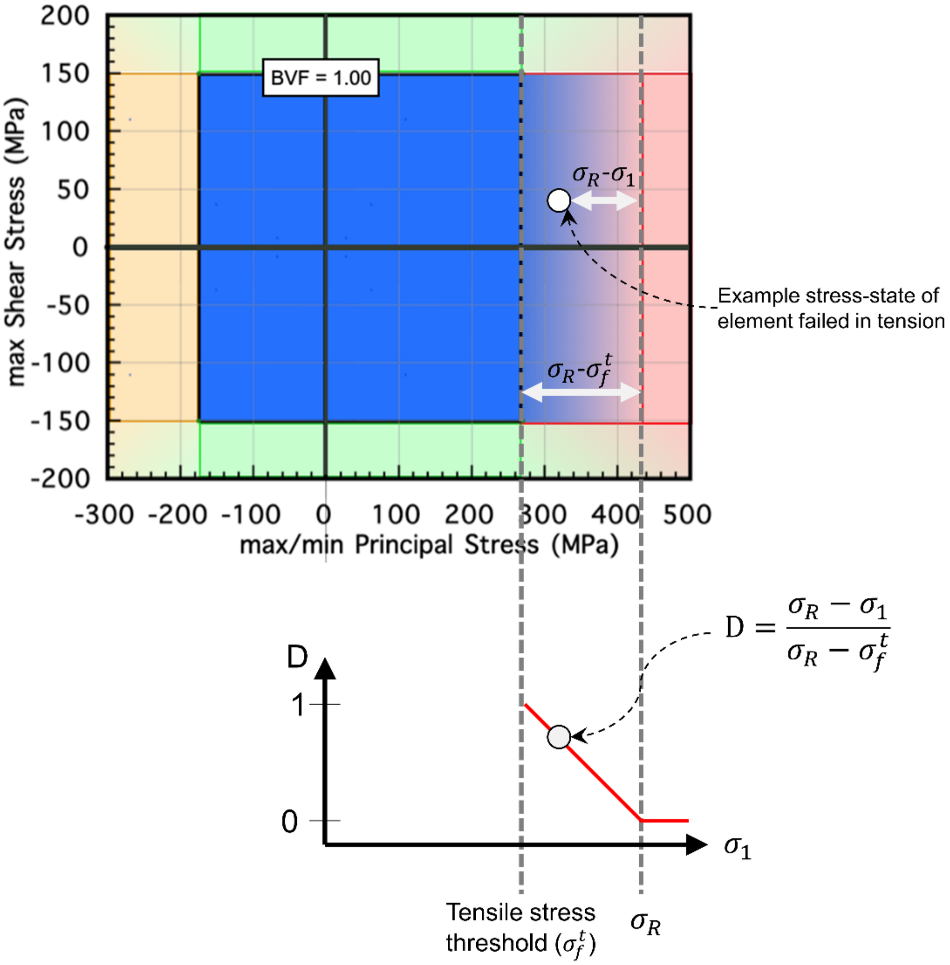

Fig. 7 How damage parameter *D* was initially calculated at time of failure, including an example stress state of a TFHB element: (top) Failure locus for an element with $f_{BV,0}$ = 100%, adapted from Weerasooriya and Alexander (2021, Fig. 7). Position of element within locus was based on principal stresses of the element. An element falling inside blue box remained active, but would fail if outside it. Element was to right of box, thus failing in tension, if maximum principal stress of the element (σ_1) was greater than tensile stress threshold of the element (σ_f^t). In VUMAT_B, buffer zone was created between σ_f^t and σ_R. (bottom) Scaling of *D* with position of element within buffer zone. A TFHB element falling inside buffer zone would be assigned a value of *D*, which scaled modulus of the element by Eq. 7.

Figure 7 illustrates how σ_R created a buffer zone for tensile failure. It also shows how D was an indication of how far beyond σ_f^t was the σ_1 of the element, relative to the distance between σ_R and σ_f^t. As indicated by Eq. 7, the Young's modulus of the TFHB element also scaled with D. Therefore, three illustrative cases can be considered:

- For the case when the maximum principal stress of the element only slightly exceeded its tensile failure threshold ($\sigma_1 \sim \sigma_f^t$), D would be nearly 1 and the Young's modulus would remain nearly the same as it was prior to failure.

- For the opposite extreme, when the maximum principal stress of the element was very large and also exceeded the buffer stress threshold ($\sigma_1 > \sigma_R > \sigma_f^t$), then D would be 0 and the element would have no stress.
- For the case when the maximum principal stress of the element was still large but slightly smaller than the buffer stress threshold ($\sigma_1 {\sim} \sigma_R > \sigma_f^t$), then *D* would be very small, the Young's modulus would also be very small, and the element would have very little stress.

The calculated D was checked against D_{floor}. If the calculated D was less than D_{floor}, then D was set to be 0 and the element was thereafter treated as carrying zero stress.

3.3.2.2 Stress in Subsequent Time Increments ($t > t_f^t$)

The damage parameter in time increments subsequent to $t = t_f^t$ was calculated based on D from the previous time increment. For a time increment *i* after failure ($i > t_f^t$), the damage parameter, D_i, was calculated by scaling the value from the previous time increment, D_{i-1}, by a factor A:

$$D_i\left(t > t_f^t\right) = A \cdot D_{i-1} \tag{10}$$

In Eq. 10 the factor A was a floating-point number less than 1, such that D continued to decrease with subsequent time increments. This process continued until D was sufficiently small, less than D_{floor}. If the calculated D was less than D_{floor}, then D was set to be 0 and the element was thereafter treated as carrying zero stress.

3.3.3 Summary of Algorithm

In summary, the algorithm gradually brought the stress of the TFHB element to zero by gradually scaling down the modulus of the TFHB element. The modulus was scaled by the damage parameter, D, where ($0 < D < 1$). At the time of failure, the initial value of D was determined by the magnitude of the maximum principal stress of the TFHB element (Eq. 8). The value of D was decreased in subsequent time increments after failure by multiplying the value from the previous increment by the factor A, where A<1 (Eq. 10). The D parameter was thus continuously decreased with each time increment until falling below D_{floor}, at which point the element was considered to have totally failed.

The performance of the algorithm depended on the following three inputs, which were adjusted to tune the load-displacement response:

- $\sigma_{R,0}$, which was used to calculate the buffer stress threshold σ_R (Eq. 9)

- the factor A, which was used to calculate D for all time increments subsequent to failure (Eq. 10)
- D_{floor}, which determined the value after which the TFHB element was considered to have totally failed and would henceforth carry zero stress. In this study, D_{floor} was always set as 1e-4.

4. Application of Updated Methods to Skullcap Simulations

The algorithms and methods described in the previous section were used to rerun the OSS to more closely match the experimental load-displacement response (detailed in Section 4.1). They were also used to transition the simulation from an Elemental Approach to a Three-Layer Approach (Section 4.2). Then, biovariability was studied by randomly reassigning the BVF values across elements using simulations based solely on the Elemental Approach (Section 4.3.1) and in hybrid simulations combining the Elemental and Three-Layer Approaches (Section 4.3.2). Finally, the POI was updated to match the experiment, and the resulting BF contours were compared with the experiment (Section 4.4).

The load-displacement responses of the various simulations were compared with the experiment by plotting crosshead force as a function of applied indentation. The load from the simulations was measured as the reaction force on the rigid indenter/impactor in the direction of displacement.

4.1 Elemental Simulation with Updated VUMAT Algorithm

The OSS was rerun using the updated algorithm, VUMAT_B. This updated simulation is referred to here as the Elemental Simulation. The parameters $\sigma_{R,0}$ and A (Section 3.3.3) were set as 480 MPa and 0.9980, respectively. The load-displacement curve from the simulation is compared with the experiment in Fig. 8. The patterns of failed elements are included in Appendix B, where they are compared with the failure patterns from the other simulations described in Section 4.2.

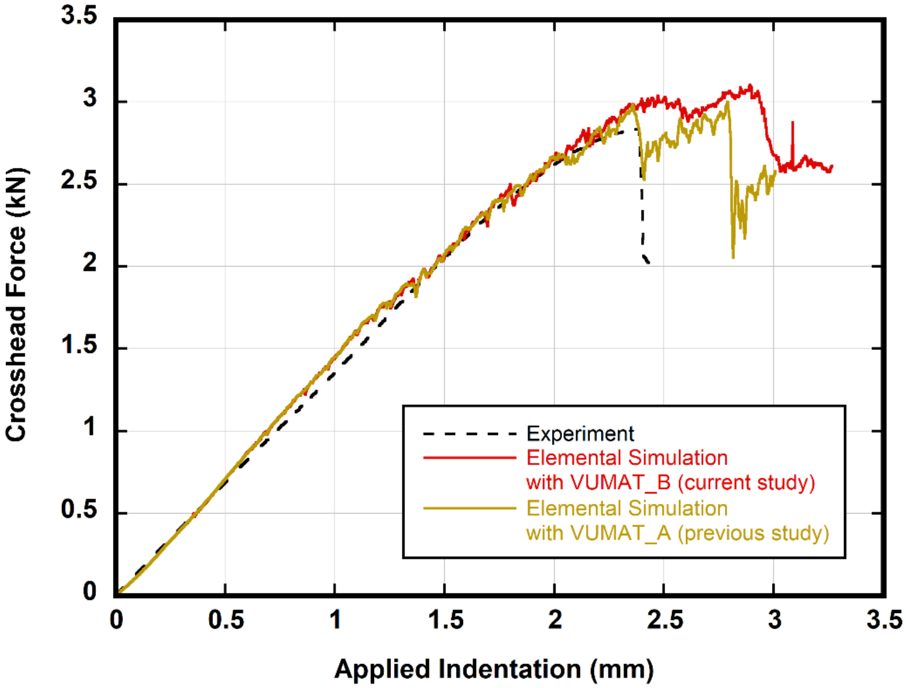

Fig. 8 Comparing load-displacement response between indentation experiment and Elemental Simulations from OSS (which used original VUMAT_A) and from current study (which used updated VUMAT_B). OSS is reproduced from Weerasooriya and Alexander (2021, Fig. 6) where it is marked as Simulation 4.

4.2 Three-Layer Simulation: Representing AZ with Three Layers

The skullcap from the Elemental Simulation was transitioned into a system that segregated the AZ from the FZ and further divided the AZ into three layers, corresponding to the OT, MD, and IT. This simulation is referred to as the Three-Layer Simulation. The goal was to identify the material properties for the four different skullcap materials in the Three-Layer Simulation and to demonstrate the process of transitioning from the more detailed Elemental Simulation to the simpler Three-Layer Simulation.

First, the algorithm described in Section 3.1.3 was used to divide the skullcap mesh in the Elemental Simulation into the AZ and FZ zones, specifying R_{action} to be 16 mm. Next, the normalized depth of the OT, MD, and IT layers within the AZ was identified. The normalized depth of the layer was the thickness of the layer in proportion to the thickness of the skullcap, which was the distance from the inner to the outer surface. The normalized depths of the three layers were found by dividing the AZ into 10 layers using the algorithm described in Section 3.1.4 and layer assignments shown in Table 2. Then, the average and standard deviation of the BVF for all of the elements within each layer was calculated. Figure 9 plots these layer BVF values as a function of normalized depth, where normalized depth was defined as 0% at the outer surface and 100% at the inner surface. In Fig. 9, the mean BVF values from the layers are connected with a solid black line, referred to as the mean-BVF line, and were taken as an approximation of the change of BVF with normalized depth. The boundaries among the three layers were identified using the quantitative procedure defined by Alexander et al. (2019). Starting from the outer table, the point at which the mean-BVF line first fell below 70% was identified as the transition from the OT to the MD. This transition was calculated to occur at a normalized depth of 21%. Continuing along the x-axis, the next point at which the mean BVF line again rose above 70% was identified as the transition from the MD to the IT. This transition was calculated to occur at a normalized depth of 72%.

The algorithm described in Section 3.1.4 was then used to divide the AZ of the elemental mesh into three layers. The OT–MD and MD–IT transitions identified previously were used to define the layer assignments in the algorithm as shown in Table 4. Figure 10 shows the resulting 3-layer mesh.

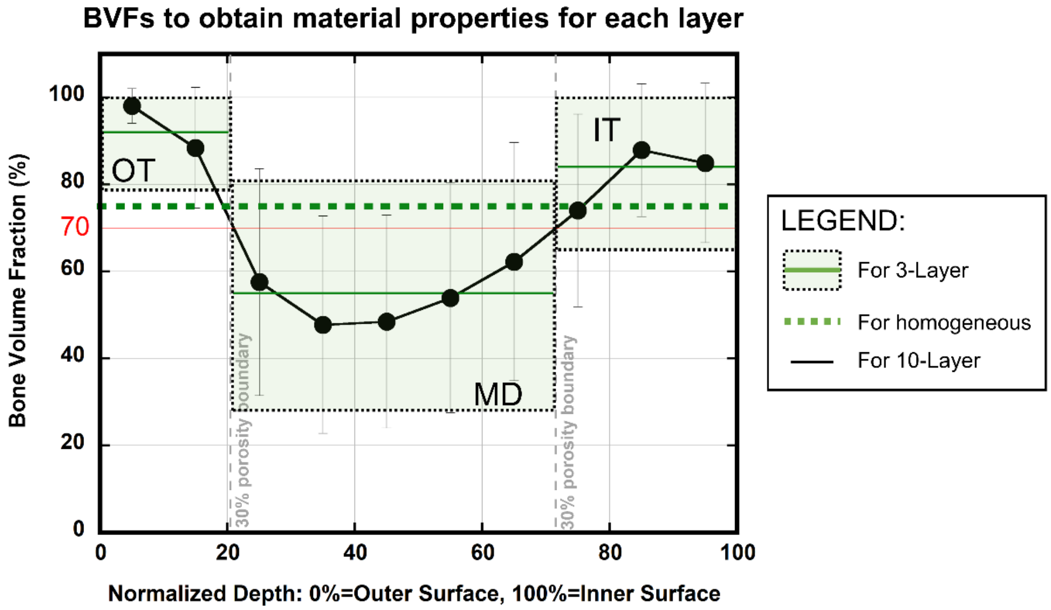

Fig. 9 BVFs to obtain material properties for each layer: Black dots in plot show mean and standard deviation (std) of BVF of each layer in 10-layer system. Black line connecting dots is mean-BVF line. Red line shows 30% porosity threshold (corresponding to BVF = 70%) to identify normalized depth boundaries of OT, MD, and IT layers based on method of Alexander et al. (2019). Green solid lines indicate mean BVF of each layer, with green shaded boxes extending to 1 std. Green dotted line indicates BVF value for use when modeling entire thickness of skull as single homogeneous material, as in FZ.

Table 4 **Assignment of three layers in AZ based on normalized depth of element (d_{elem}^{norm})**

Value of d_{elem}^{norm}	Layer assignment
$0 \le d_{elem}^{norm} < 0.21$	OT
$0.21 \le d_{elem}^{norm} < 0.72$	MD
$0.72 \le d_{elem}^{norm}$	IT

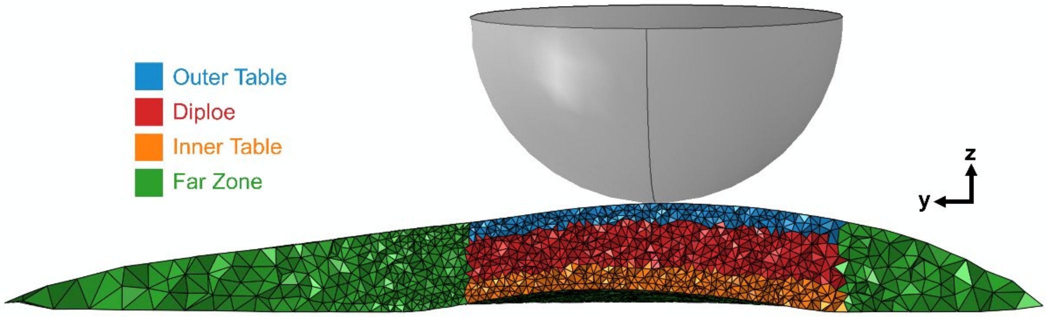

Fig. 10 **Cross-sectional view of skullcap mesh in Three-Layer Simulation, with elements color-coded by material**

An iterative process then identified BVF values and VUMAT_B algorithm parameters. As an initial approximation, the average BVF for each of the regions in the 3-layer mesh (OT, MD, IT, and FZ) was calculated by averaging the BVF for all of the elements in each region. These initial BVF values are shown by the green lines in Fig. 9 and were OT = 92%, MD = 55%, IT = 84%, and FZ = 75%. Then the 3-layer system was simulated and the computed load-displacement response was compared with the experiment. The BVF and algorithm values were then adjusted and the simulation was rerun. This process was repeated, by systematically changing the BVFs, until the numerical load-displacement response satisfactorily approximated the experiment while keeping the change in BVFs within ±5%. Even though we did not optimize to minimize the sum of mean squares of error, we believe we obtained closer to the best set of BVFs while not deviating from the experimentally measured average BVF. The final BVF values were OT = 90%, MD = 52.5%, IT = 80%, and FZ = 75%. The BVF-dependent properties resulting from these BVF values are summarized in Table 5. The VUMAT_B algorithm parameters were the same as in the Elemental Simulation: A = 0.9980, $\sigma_{R,0}$= 480 MPa. Figure 11 compares the load-displacement curve for the Three-Layer Simulation run with these final parameter values with the experimental response and the Elemental Simulation. The pattern of failed elements in the Three-Layer Simulation are included in Appendix B, where they are compared with the failure patterns from the Elemental Simulation and the hybrid simulations described as follows.

Table 5 Optimized BVF-Dependent properties assigned to skullcap elements in Three-Layer Simulation

Property	OT	MD	IT	FZ	Units
Averaged BVF	90	52.5	80	75	%
Young's modulus	2.53	1.07	2.10	1.89	GPa
Density	1.62	0.95	1.44	1.35	g/cm^3
Compressive failure strength	141.75	48.23	112.00	98.44	MPa
Tensile failure strength	218.21	74.25	172.42	151.54	MPa
Shear failure strength	121.50	41.34	96.00	84.38	MPa

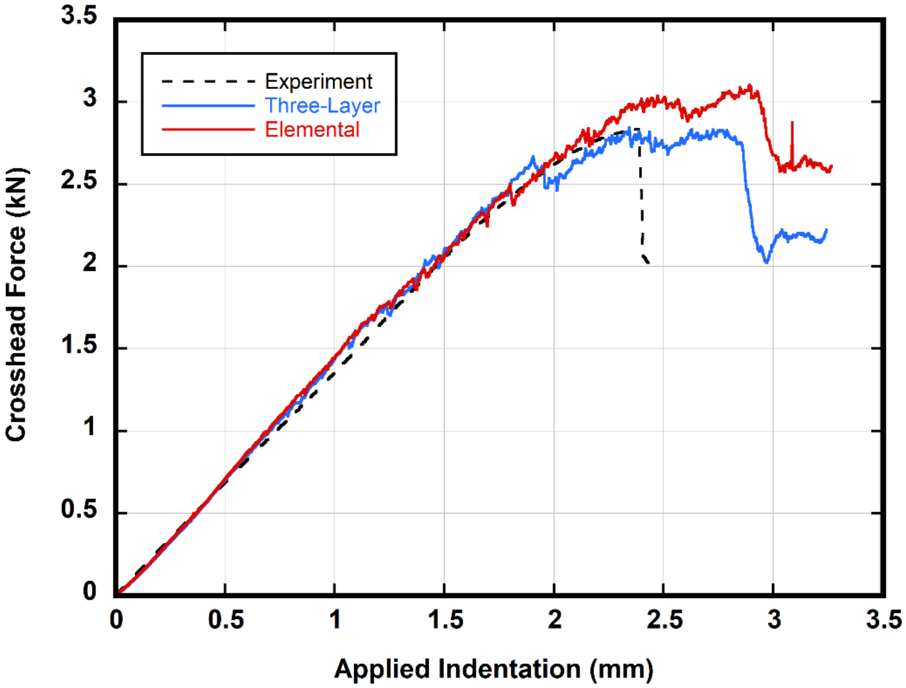

Fig. 11 Load-displacement from Three-Layer simulation compared with Elemental Simulation (Section 4.1) and experimental response

4.3 Randomizing BVF Assignments

Biovariability was simulated by randomly redistributing the BVF assignments in the Elemental and Three-Layer simulations as described below. Section 4.3.1 describes simulations that started from the Elemental Simulation and randomly redistributed the element-BVF assignments of a particular subset of elements. Section 4.3.2 describes simulations characterized as hybrids between the Three-Layer and Elemental simulations.

4.3.1 Randomizing BVF Assignments in Elemental Simulation

The simulations in this section started from the Elemental Simulation where each element in the skullcap mesh had a particular BVF assignment, $f_{BV,0}$. Here, these element-BVF assignments were randomized across all elements based on a critical threshold value of $f_{BV,0}$=70%. One set of five simulations randomized the element-BVF assignments for all elements with $f_{BV,0} < 70\%$. These five simulations are referred to as Randomized #1 BVF<70% through Randomized #5 BVF<70%.

The randomized redistribution of element-BVF assignments was implemented in Python by creating a matrix with three columns: Column 0, Column 1, and Column 2. For each element with $f_{BV,0}$ < 70%, a new row was appended to the matrix with the element number stored in Column 1 and the $f_{BV,0}$ value stored in Column 2. After iterating over all of the elements, the number of rows in the matrix corresponded to the number of elements with a BVF < 70%. Then, a list of randomly arranged integers ranging from 1 to the number of rows of the matrix was instantiated using the `random.sample()` function from The Python Standard Library (https://docs.python.org/3/library/random.html). This list was inserted into the matrix as Column 0. Then, Columns 0 and 1 were sorted based on Column 0, while leaving the original BVF assignments in Column 2 unmoved. This is demonstrated in the example shown in Fig. 12. After the matrix was sorted, each row contained a BVF value (Column 2) and the newly assigned element number (Column 1). The Abaqus input file was then updated with the new element-BVF assignments.

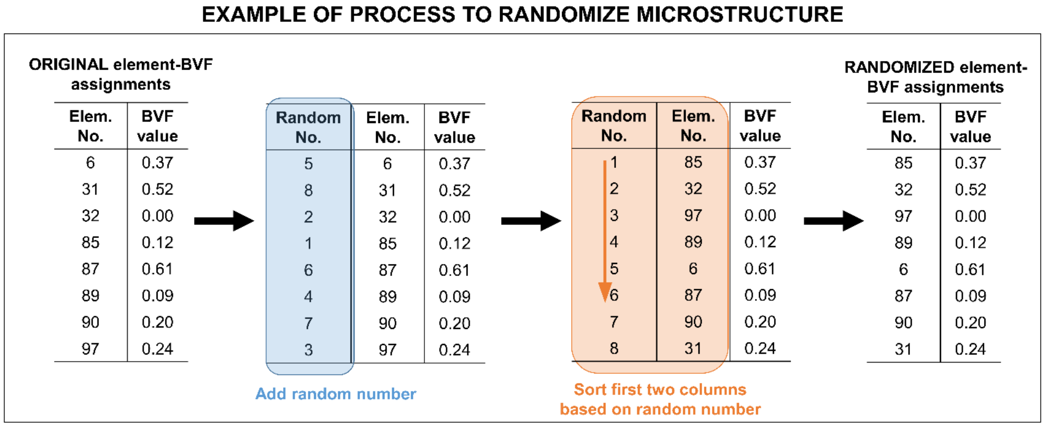

EXAMPLE OF PROCESS TO RANDOMIZE MICROSTRUCTURE

ORIGINAL element-BVF assignments

Elem. No.	BVF value
6	0.37
31	0.52
32	0.00
85	0.12
87	0.61
89	0.09
90	0.20
97	0.24

Random No.	Elem. No.	BVF value
5	6	0.37
8	31	0.52
2	32	0.00
1	85	0.12
6	87	0.61
4	89	0.09
7	90	0.20
3	97	0.24

Random No.	Elem. No.	BVF value
1	85	0.37
2	32	0.52
3	97	0.00
4	89	0.12
5	6	0.61
6	87	0.09
7	90	0.20
8	31	0.24

RANDOMIZED element-BVF assignments

Elem. No.	BVF value
85	0.37
32	0.52
97	0.00
89	0.12
6	0.61
87	0.09
90	0.20
31	0.24

Fig. 12 Example of process to redistribute BVF values among elements that considers case of randomizing only across elements with an original BVF of < 70%

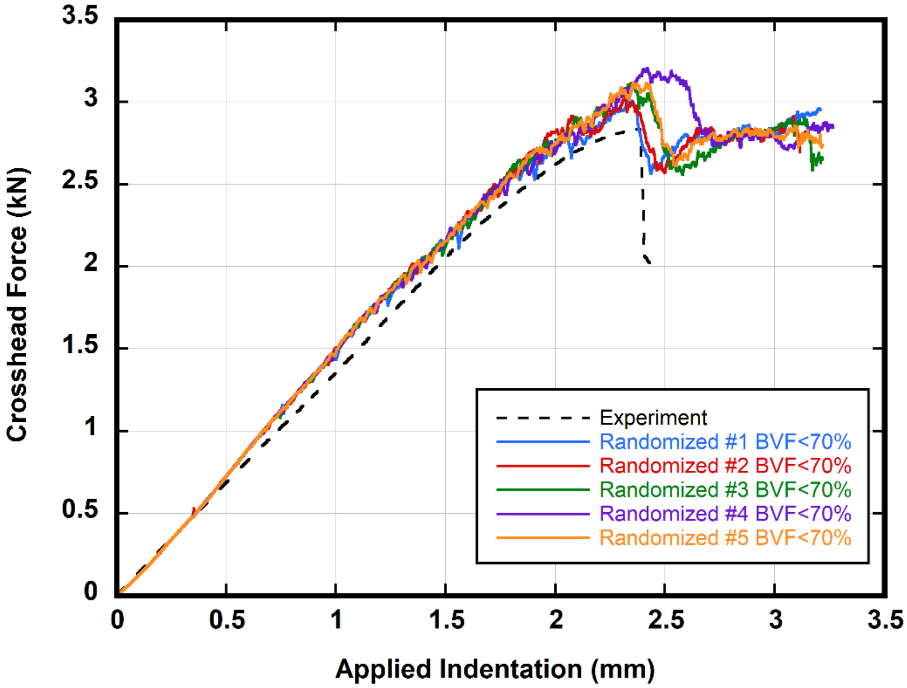

Fig. 13 Load-displacement response from five simulations where BVF assignments were randomized among all elements with an original BVF < 70%

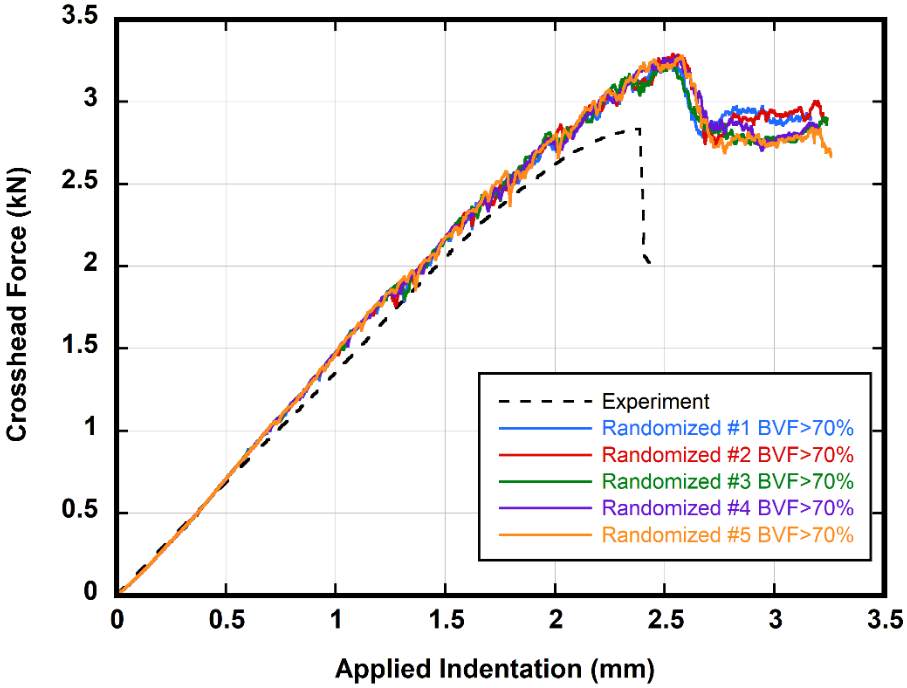

Fig. 14 Load-displacement response from five simulations where BVF assignments were randomized among all elements with an original BVF > 70%

This randomization process was repeated five times, creating five new Abaqus input files for the simulations Randomized no. 1 BVF<70% through Randomized no. 5 BVF<70%. These simulations were then run exactly as the Elemental Simulation (Section 4.1), using the same parameters for the updated algorithm, VUMAT_B. Figure 13 shows the load-displacement response. Appendix A (Section A.2) shows the failure patterns of the skullcap meshes, with elements color-coded by whether they failed by compression, tension, or shear.

An analogous process was applied to randomize the element-BVF assignments from the Elemental Simulation across all elements with $f_{BV,0} > 70\%$. This process created five new simulations referred to as Randomized no. 1 BVF>70% through Randomized no. 5 BVF>70%. Figure 14 shows the load-displacement response. Appendix A (Section A.3) shows the failure patterns of the skullcap meshes, with elements color-coded by whether they failed by compression, tension, or shear.

4.3.2 Randomizing BVF Assignments in Hybrid Elemental/3-Layer Mesh

The simulations in this section started from the Three-Layer Simulation. As described in Section 4.2, the Three-Layer Simulation represented the skullcap with three layers/materials in the AZ: the OT, MD, and IT. In the hybrid simulations described here, one or two of these layers were selectively converted to the elemental representation used in the Elemental Simulation, where each element had a BVF assignment. Finally, the element-BVF assignments were randomly redistributed within the layer(s) that had been converted back to the elemental representation. The random redistribution was carried out using the procedure described above (example shown in Fig. 12).

Table 6 Three sets of hybrid simulations

	Set A	**Set B**	**Set C**
Randomized layer	Only OT	Only IT	OT and IT
Homogeneous regions	MD, IT, and FZ	OT, MD, and FZ	MD and FZ
Simulation names	OT Randomized #1 OT Randomized #2 OT Randomized #3 OT Randomized #4 OT Randomized #5	IT Randomized #1 IT Randomized #2 IT Randomized #3 IT Randomized #4 IT Randomized #5	OT&IT Randomized #1 OT&IT Randomized #2 OT&IT Randomized #3 OT&IT Randomized #4 OT&IT Randomized #5

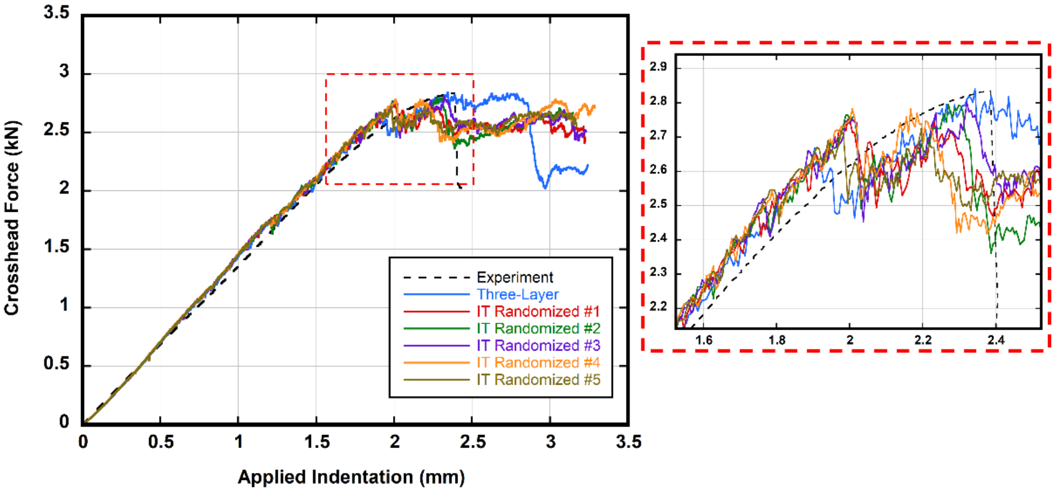

Fig. 15 **Load-displacement response from Set A's five hybrid simulations where only IT was treated with Elemental Approach; inset (right) enlarges area of catastrophic load drop in hybrid simulations**

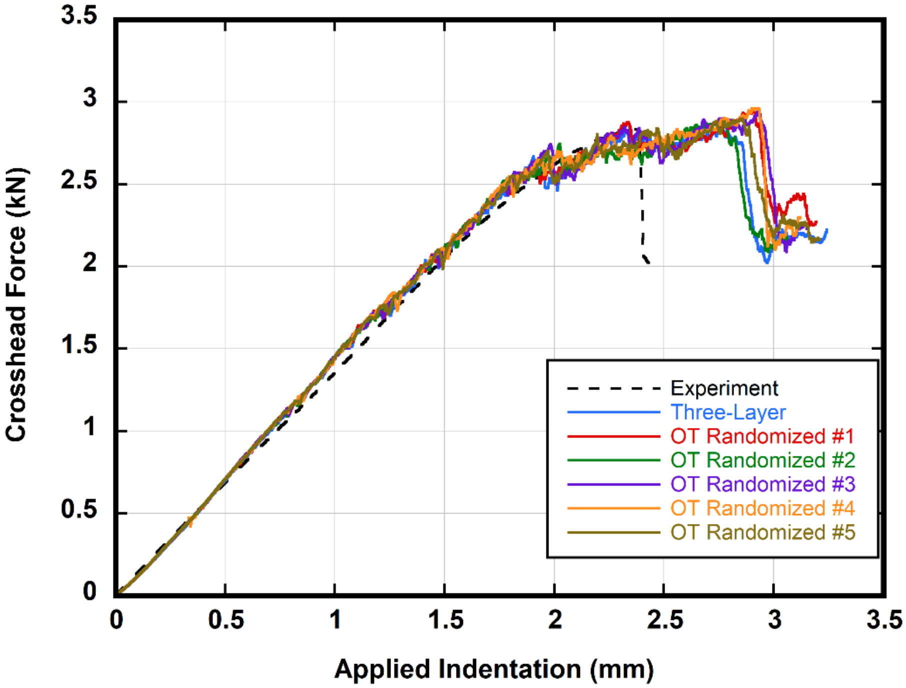

Fig. 16 **Load-displacement response from the five hybrid simulations of Set B, where only OT was treated with Elemental Approach**

Three different sets of simulations were run as shown in Table 6. In Set A, only the OT was reverted back to the elemental system and the element-BVF assignments were randomized for all of the elements in the OT. In Set B, only the IT was reverted back to the elemental system and the element-BVF assignments were randomized for all of the elements in the IT. In Set C, both the OT and the IT were reverted back to the elemental system. The element-BVF assignments of the IT elements were randomized across all of the elements of the IT. Similarly, the element-BVF assignments of the OT elements were randomized across all of the elements of the OT. There was no cross-talk during the randomization process between the IT and the OT.

The hybrid simulations were run as in the Elemental or Three-Layer simulations (the Elemental and Three-Layer simulations were run in an identical manner with the only difference being the material definitions). The same VUMAT_B parameters were used as in the Elemental or Three-Layer simulations. Figures 15–17 compare the load-displacement responses. Failure patterns on the BF and cross section are compared in Appendix B.

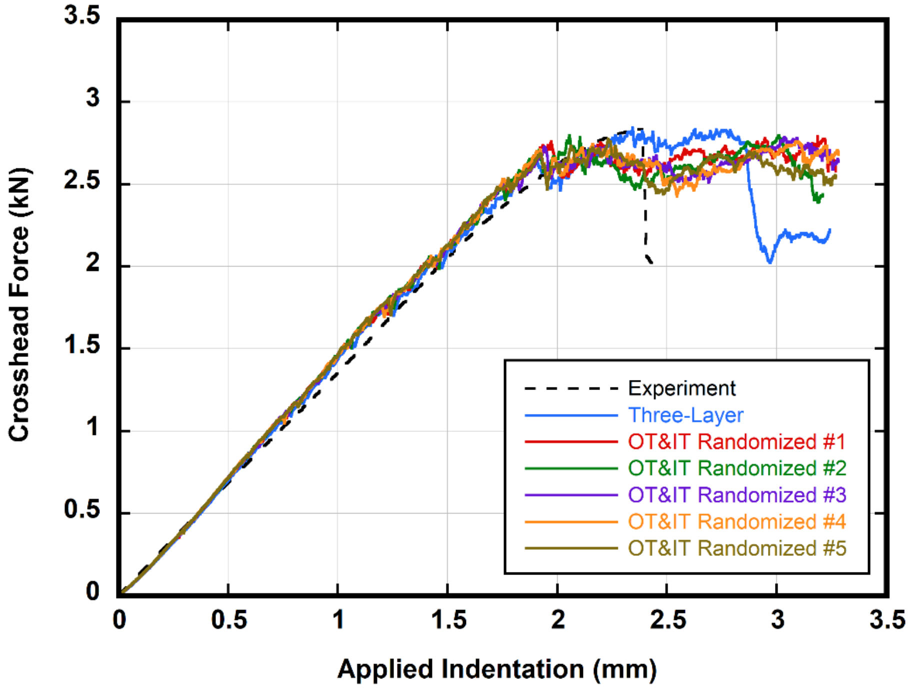

Fig. 17 Load-displacement response from the five hybrid simulations of Set C, where both OT and IT layers were treated with Elemental Approach

4.4 Changing POI to More Closely Match Experiment

The simulations previously described (Sections 4.1–4.3) used the same POI as in the OSS. The POI in the OSS was only an approximation of the experimental POI, which was difficult to match in the simulation due to the hemispherical indenter/impactor contacting the hemispherical-shaped skullcap specimen (Fig. 1) The approximate POI was previously accepted as sufficient due to the satisfactory match of the simulated load-displacement response with that of the experiment.

However, the approximate POI was found to be insufficient when we started to analyze and obtain the out-of-plane (z-direction) displacement of the specimen BF, referred to here as the BFD. The difference between the POI in the experiment and simulation was obvious, causing a difference in alignment of the BFD contours.

Therefore, effort was made to precisely obtain the experimental POI, and the Elemental Simulation was rerun with this updated optimization. This simulation is referred to as the Updated POI Simulation. After changing the POI, the skullcap failed too late compared with the experiment. Therefore, the compressive failure threshold was reduced by 14% to 150 MPa and the tensile failure threshold by 11% to 240 MPa. The shear-failure threshold was maintained at 150 MPa as in the Elemental Simulation. Table 7 summarizes the BVF-dependent properties used in the Updated POI Simulation and used in subsequent Elemental Simulations. The parameters in the VUMAT_B also remained the same, except that the Parameter A was changed to a value of A = 0.9955.

Table 7 BVF-dependent properties assigned to skullcap elements in Updated POI Simulation

Property	BVF relationship	Units
Young's modulus	$E = 3.0 \cdot \left(f_{BV,0}\right)^{1.6}$	GPa
Density	$\rho_0 = 1.8 \cdot \left(f_{BV,0}\right)$	g/cm^3
Compressive failure	$\sigma_f^c = 150 \cdot \left(f_{BV,0}\right)^{2.0}$	MPa
Tensile failure	$\sigma_f^t = 240 \cdot \left(f_{BV,0}\right)^{2.0}$	MPa
Shear failure	$\sigma_f^s = 150 \cdot \left(f_{BV,0}\right)^{2.0}$	MPa

Notes: These relationships were used in the elemental skullcap simulation referred to as the Updated POI Simulation, in which the POI was updated from the OSS to more closely match the experiment. They can be contrasted with corresponding relationships from the OSS (Weerasooriya and Alexander 2021), which was presented as Table 1.

Figures 18–23 compare the BFD contours between the Updated POI Simulation and the experiment at various levels of applied indentation, and also include the load-displacement response (BF views from experimental and simulation are at the same scales in all figures). The BFD contours are a bottom-up view of the bottom surface of the backing plate, which is the opposite surface to what was shown in the top-down view in Fig 3. The BFD contours therefore only show the portion of the skullcap visible through the viewing port. Figure 18 annotates the skullcap and backing plate for reference. The BFD was measured in the experiment using digital image correlation (DIC) of images of the specimen BF. Additional information regarding the DIC analysis was in the experimental publication (Gunnarsson et al. 2021b).

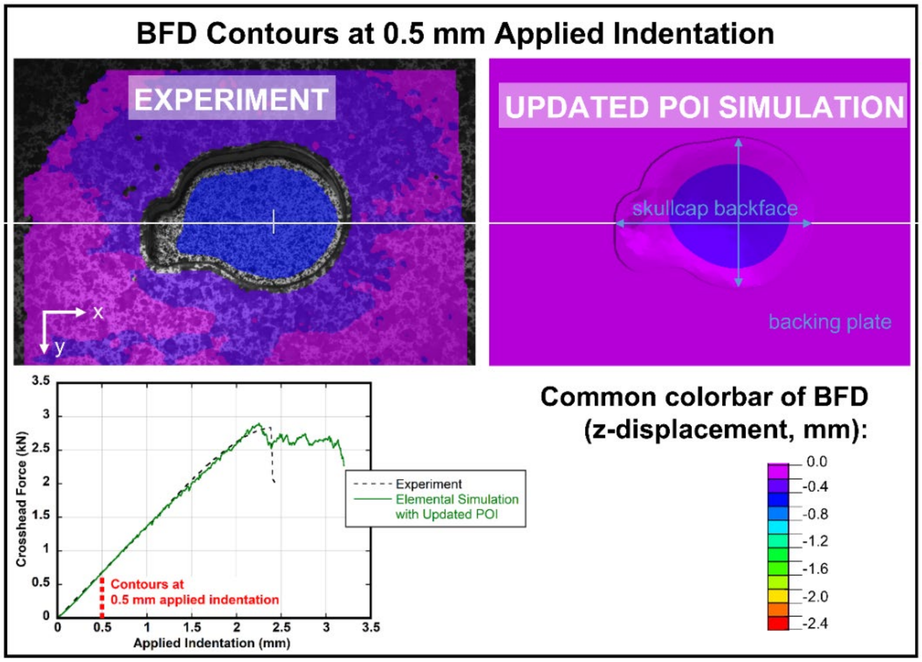

Fig. 18 **BFD contours from experiment and Updated POI Simulation at 0.5 mm of applied indentation; scale for both contours is shown in color bar on bottom-right, and POI is indicated for reference**

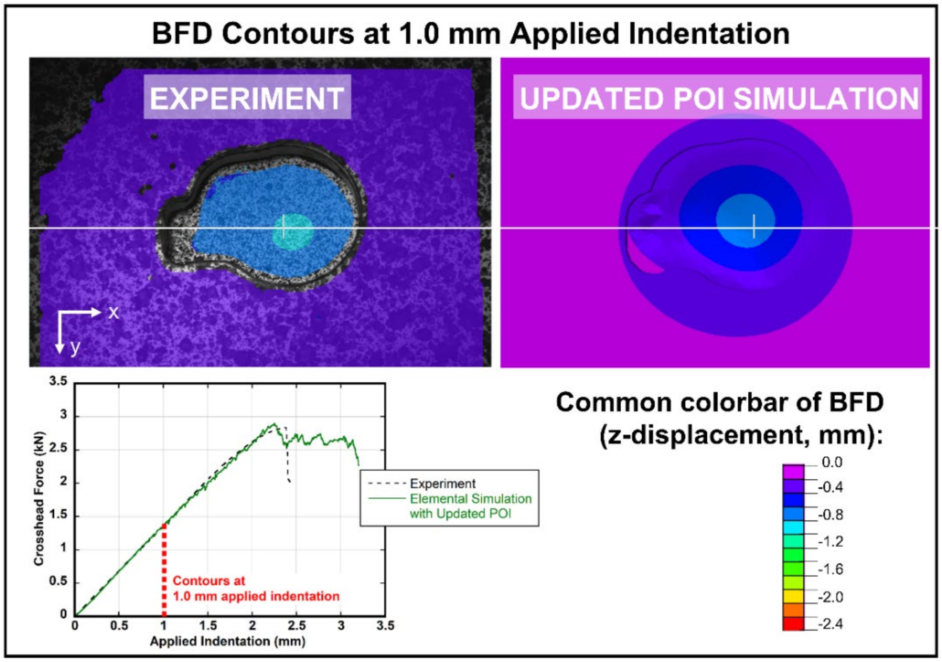

Fig. 19 **BFD contours from experiment and Updated POI Simulation at 1.0 mm of applied indentation; scale for both contours is shown in color bar on bottom-right, and POI is indicated for reference**

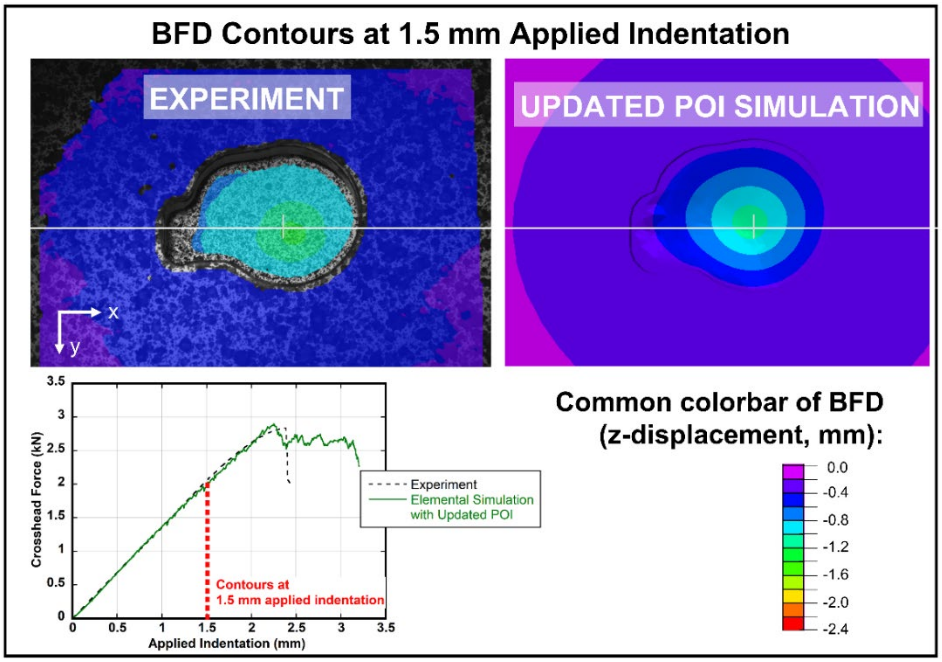

Fig. 20 BFD contours from experiment and Updated POI Simulation at 1.5 mm of applied indentation; scale for both contours is shown in color bar on bottom-right, and POI is indicated for reference

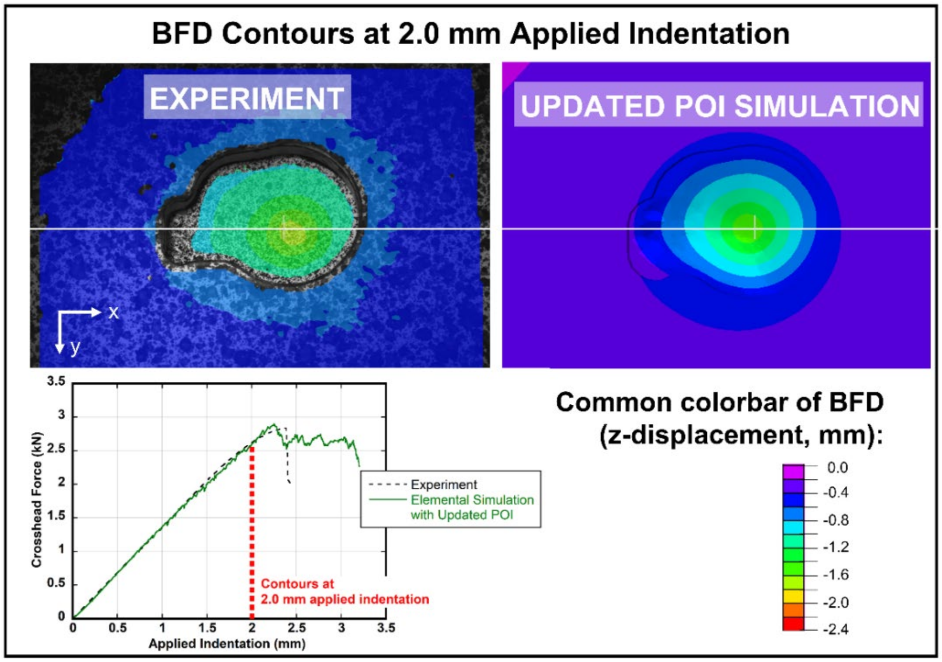

Fig. 21 BFD contours from experiment and Updated POI Simulation at 2.0 mm of applied indentation; scale for both contours is shown in color bar on bottom-right, and POI is indicated for reference

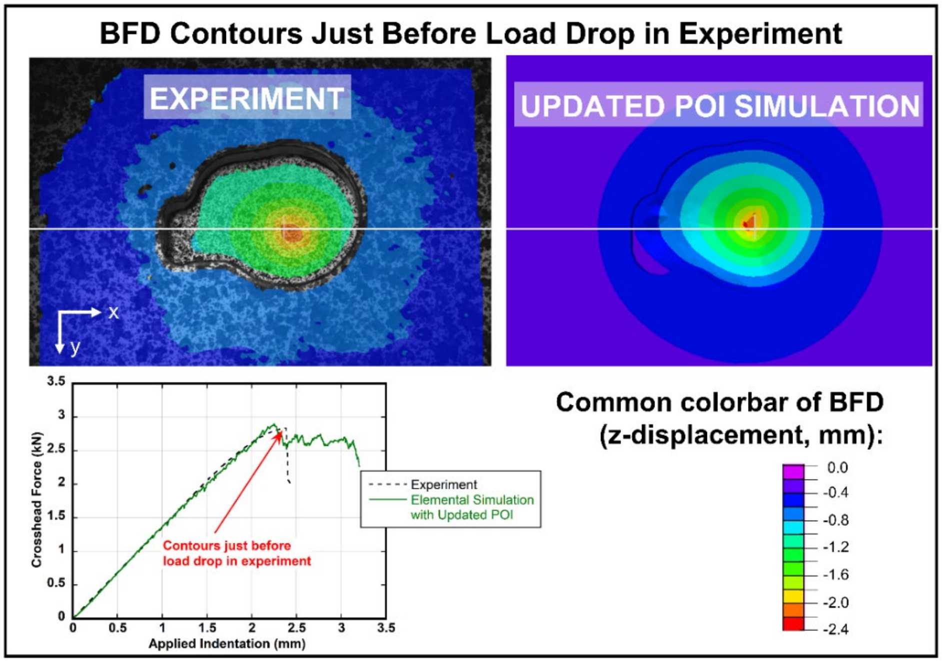

Fig. 22 BFD contours from experiment and Updated POI Simulation just before load drop in experiment; scale for both contours is shown in color bar on bottom-right, and POI is indicated for reference

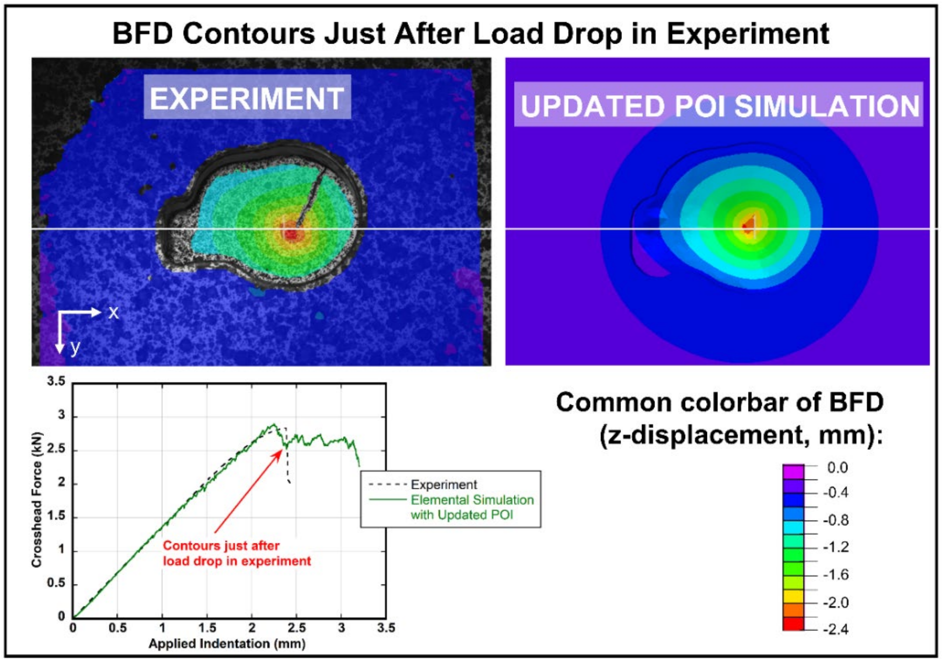

Fig. 23 BFD contours from experiment and Updated POI Simulation just after load drop in experiment; scale for both contours is shown in color bar on bottom-right, and POI is indicated for reference

5. Analysis and Discussion

5.1 Comparing Elemental and Three-Layer Simulations

In terms of load-displacement, the fidelity of the Three-Layer Simulation to the experiment was comparable to the fidelity of the Elemental Simulation to the experiment (Fig. 11). The two responses followed a similar trend of approximately four sequential stages. The first stage was linear loading to approximately 1.5 mm of applied indentation. In the next stage, the load increased nonlinearly with displacement to about 2.4 mm of applied indentation. The third stage could be considered as load plateau, where the load fluctuated with further increases in displacement, but did not significantly increase. The final stage was catastrophic failure. The catastrophic failure occurred around 3 mm of applied indentation in both simulations and consisted approximately of a 0.75-kN load drop in the Three-Layer Simulation and a 0.5-kN load drop in the Elemental Simulation. In the experiment, the catastrophic unstable failure occurred earlier, at approximately 2.4 mm of applied indentation, and corresponded to a sudden fracture that brought the load down to 0 (Gunnarsson et al. 2021b). It is very difficult to experimentally study initiation and propagation of catastrophic failure in detail. In addition, the methodology in the current study and in general (a topic beyond the scope of this present study) cannot predict the unstable catastrophic growth of fracture after initiation. The catastrophic failure in the Elemental Simulation was noticeably less than in the experiment. However, in this study fracture initiation, rather than the timing or extent of the catastrophic failure, was used to compare the simulation outcomes with the experiment.

Despite the close match in the load-displacement responses between the Elemental and Three-Layer simulations, the failure patterns presented in Appendix B indicated the failure mode was fundamentally different between the two approaches. Figure 24 summarizes the difference in failure modes. The BF of the Elemental Simulation showed linear tensile cracking, which was similar to the cracking pattern observed in the post-test micro-CT images from the experiment (Gunnarsson et al. 2021b). These tensile cracks on the BF were gradually propagating as a function of time/indentation, since they could also be seen at 1 and 2 mm of displacement.

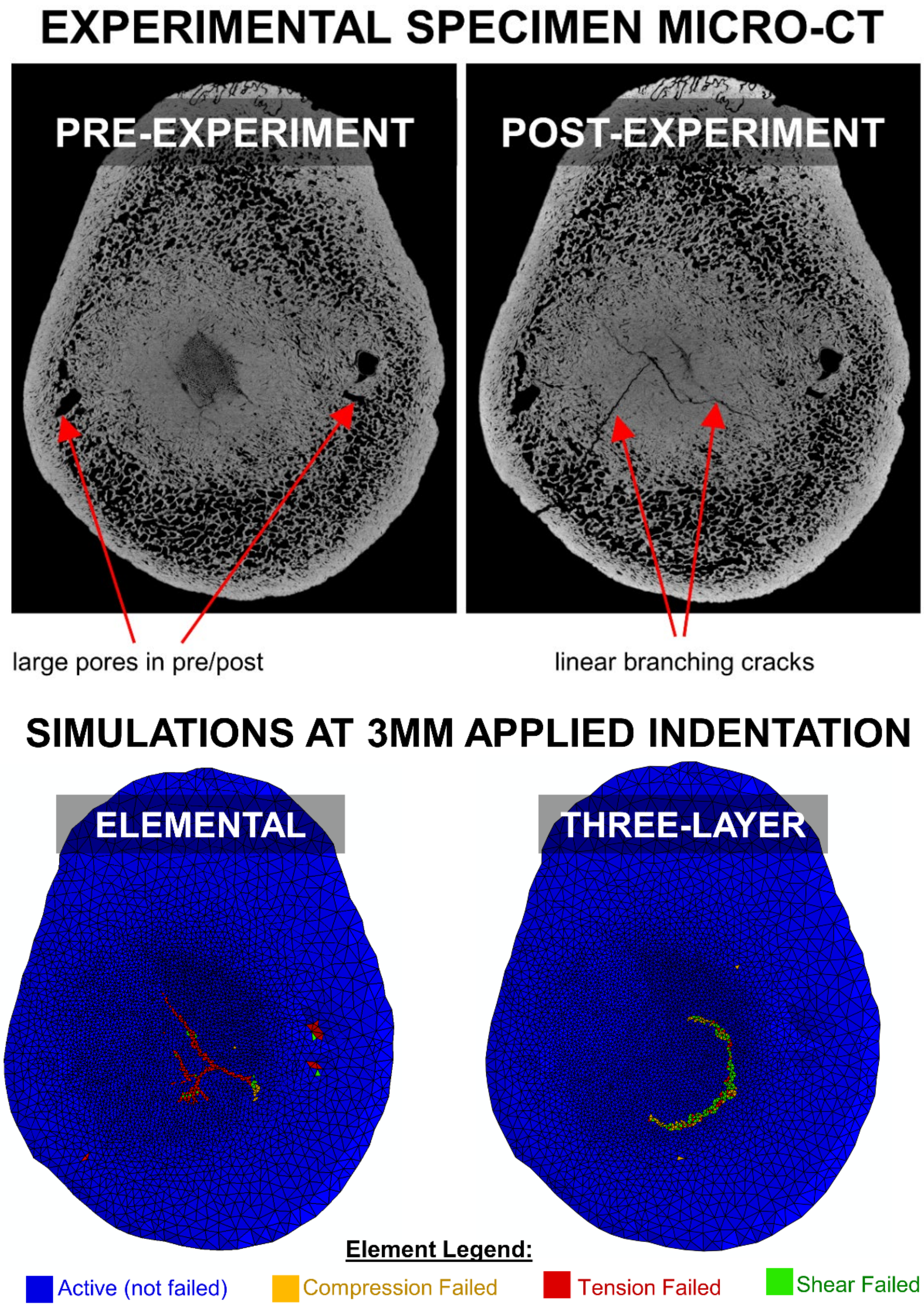

Fig. 24 Comparison of failure mechanisms on specimen BF: (top) micro-CT images from the experiment (Gunnarsson et al. 2021b), where grey corresponds to bone and black corresponds to pores or surrounding space; (bottom) failure patterns in the Elemental and Three-Layer simulations at a time increment corresponding to 3 mm of applied indentation

Conversely, the failure pattern on the BF of the 3-layer model more closely resembled shear punch failure (shear dominated) and was significantly different from the Elemental Simulation and the experimentally observed cracking pattern.

No failed elements on the BF were observed at either 1 or 2 mm of applied indentation. At 3 mm of displacement, the failure pattern was semicircular, centered around the POI. Moreover, many of the elements on the BF failed in shear and compression and only a few failed in tension, in sharp contrast to the Elemental Simulation. Finally, the cross section of the Three-Layer Simulation at 3 mm of applied indentation included only a single crack running vertically through the inner table, composed of both tension-failed as well as shear-failed elements. This was also in contrast to the elemental model, which showed at least two different cracks running vertically through the inner table and comprising only tensile-failed elements without any shear-failed elements.

The different failure mode in the Three-Layer Simulation could be caused by the fact that, in this simulation, all of the elements in the inner table had a uniform, relatively high BVF of 80%. In contrast, the inner table in the Elemental Simulation had a nontrivial number of elements with very low BVF, as shown by elements color-coded by BVF in Fig 1. These low-BVF elements were able to fail sooner in the Elemental Simulation, since the tensile failure threshold scaled with BVF.

5.2 Effect of Randomization Based on BVF = 70% Threshold

Randomizing the BVF assignments among elements with $f_{BV,0} < 70\%$ had a more pronounced effect on the load-displacement response (Fig. 13) compared with randomizing among elements with $f_{BV,0} > 70\%$ (Fig. 14). In fact, the later randomization (for $f_{BV,0} > 70\%$) produced only a negligible effect on the load-displacement response.

Randomizing among elements with $f_{BV,0} < 70\%$ also had a greater effect on the back-surface failure patterns when evaluating failure mechanism and number of elements differing from the unrandomized simulation (Appendix A). At 1 mm of applied indentation, the back-surface failure for the Randomized BVF>70% simulations show no observable difference (Fig. A-4), while there is a more pronounced difference in the Randomized BVF<70% simulations (Fig. A-1). This observed difference is likely due to a large pore in the diploe that is assigned a higher BVF when the BVF<70% is randomized. At 2 mm of applied indentation, the back-surface failures for the Randomized BVF<70% simulations are largely observed as tensile failures but are scattered with little connectivity among failed elements, creating markedly different patterns compared with the unrandomized simulation (Fig. A-2). In contrast, the back-surface failures for the Randomized BVF>70% simulations are similar to the unrandomized simulation. At 3 mm of applied indentation, the back-surface failure patterns from the Randomized BVF<70% simulations deviated more substantially from the unrandomized simulation (Fig. A-3) than did the failure patterns from the Randomized BVF>70% simulations (Fig. A-6). The failure patterns in the Randomized BVF>70% simulations could be characterized as systems of linear tensile cracks while the patterns observed in the Randomized BVF<70% simulations cannot be described as largely a single-failure mechanism (i.e., failing in tension, compression, or shear).

Since the primary failure mechanism resulting in the final back-surface failure pattern is tensile failure, it is important to note differences in tensile-failure patterns. Interestingly, the Randomized BVF<70% simulations all demonstrated a similar "skewed-H" tensile-failure pattern. These crack systems were similar in nature to the cracking pattern of the unrandomized simulation, comprising lines of elements that had predominantly failed in tension. The effect of randomization for $f_{BV,0} > 70\%$ appeared to be in changing the orientation and extent of the crack systems. Recently, a medical panel that was convened to review skull fracture and injury severity indicated fractures in some regions of the head/skull may lead to more severe outcomes (Chattopadhyay and Tripathi 2010). From a modeling perspective, when beginning to consider biovariability of the human skull and the potential for injury based on skull-fracture direction and extent, the changes observed in the fracture patterns from the Randomized BVF>70% simulations become intriguing. Specifically, with a pool of just six simulations (the five randomizations plus the original BVF assignments), it is possible to begin to look at the potential for larger fractures or fractures heading in different directions within a population. In all of the simulations, there was a crack system aligned along the axis between the northwest (NW) and southeast (SE) directions on the BF, as oriented in the images in Appendix A. This crack orientation is referred to as the NW–SE direction. There was also an additional crack orientation roughly aligned along the axis between the northeast (NE) to southwest (SW) directions, which is referred to as the NE–SW direction. This secondary crack orientation was generally much less extended than the NW–SE crack. The exceptions were two of the simulations (Randomized #3 BVF>70% and Randomized #5 BVF>70%), where the crack in the NE–SW direction was roughly equal in length to the crack in the NW–SE direction. While more data is required to make a definitive conclusion, the statistical power to say that a NE–SW crack is possible in a population could be remarkably useful, especially as injury-severity analysis continues to evolve and potential vulnerable regions of the head are identified by medical experts.

Another consideration is that randomizing among the lower-BVF elements probably had a more pronounced effect on the response because the range of BVF assignments involved (from 0% to 70%) was much larger than the range involved when randomizing among the higher-BVF elements (only from 70% to 100%).

5.3 Effect of Randomization in Hybrid Elemental–Three-Layer Simulations

In this section, the load-displacement response and the failure patterns from the hybrid simulations are compared with those from the Three-Layer and Elemental simulations, which were described in Section 5.1.

The OT Randomized simulations had very similar load-displacement responses compared with the Three-Layer Simulation (Fig 16). These responses included a catastrophic load drop occurring at approximately the same time (just prior to 3-mm applied indentation) and with similar magnitude (around 0.75 kN). In addition, both the cross-sectional and BF failure patterns in the OT Randomized simulations more closely resembled the Three-Layer Simulation rather than the Elemental Simulation. As in the Three-Layer Simulations, the OT Randomized simulations showed a shear-punch type of failure characterized on the BF by a semicircular failure pattern consisting of many elements that had failed in shear (Fig. B-4). On the cross-sectional view, this type of failure was characterized by a single crack system running through the inner table (Fig. B-7). The singular exception to these observations was OT Randomized #4, which appeared to have a system of linear tensile cracks in addition to the shear-punch type of failure.

On the other hand, the responses of the IT Randomized simulations deviated from the Three-Layer Simulation both in the load-displacement response and in the failure patterns. The catastrophic load drop in the IT Randomized simulations was much smaller in magnitude and occurred earlier. In the IT Randomized simulation, the load drop was less than 0.5 kN in magnitude and occurred between 2 and 2.5 mm of applied indentation, whereas in the Three-Layer Simulation the load drop was about 0.75 kN and occurred just prior to 3 mm of applied indentation. In addition, the BF failure patterns of the IT Randomized simulations (Fig. B-14) had more clearly identifiable systems of linear tensile cracks compared with the shear-punch type of failure seen in the Three-Layer Simulation, although the orientation of these failure patterns differed from the Elemental Simulation.

Finally, randomizing both the OT and the IT (Set C simulations) had a similar effect to randomizing only the IT. The BF failure patterns of the Set C simulations (Fig. B-21) resembled those of the IT Randomized simulations with systems of linear tensile cracks. The cross-sectional failure patterns (Fig. B-18) also clearly deviated from the Three-Layer Simulation. Moreover, the load-displacement response was also noticeably differed from the Three-Layer Simulation (Fig. 17). The catastrophic load drop clearly evident in the Three-Layer Simulation, the Elemental Simulation, and the OT Randomized simulations is not distinctly noticeable in the Set C Randomized Simulations. The catastrophic load drop could either be totally absent, reduced in magnitude, or spread out over a longer period of applied indentation so as to not appear as sharply as in the other types of simulations.

In summary, linear-tensile-crack systems were present whenever the IT layer was treated using the Elemental Approach (the IT Randomized and the Set C Randomized Simulations). Treating the IT layer as a single homogeneous material, as in the OT Randomized Simulations and the Three-Layer Simulation, caused the shear-punch type of failure.

5.4 Significance of Intrinsic Porous Structure

The outcomes from the randomized simulations indicate there were intrinsic porous structures in the in vivo skullcap that were disrupted during the randomization process. Figure 25 compares the load-displacement responses from the Randomized BVF<70% simulations (originally shown in Fig. 13), the Randomized BVF>70% simulations (originally shown in Fig. 14), and the Elemental Simulation run prior to randomization (originally shown in Fig. 8). When compared with the load-displacement response from the Elemental Simulation, the load-displacement responses of the Randomized BVF<70% simulations were relatively similar to each other and distinct from the Elemental Simulation. Similarly, the Randomized BVF>70% load-displacement responses were very closely aligned to each other, but distinct from the Elemental Simulation.

This phenomenon of the randomized simulations having similar responses to each other but noticeably distinct from the in vivo configuration (Elemental Simulation, prior to randomization) is likely due to the randomization process partitioning inherent porous structures that were present in the in vivo configuration. The Elemental Simulation had clusters of elements with zero or very low BVF, corresponding to pores in the in vivo configuration that were larger than the element size. These clusters of low-BVF elements were broken up during the randomization process, which randomly redistributed the BVF values of each element. Therefore, the randomization process disordered any structures or networks of larger pores that were in the in vivo configuration. Instead, the low-BVF elements in the randomized simulations were randomly dispersed fragmenting larger pores into multiple smaller pores distributed within the specimen.

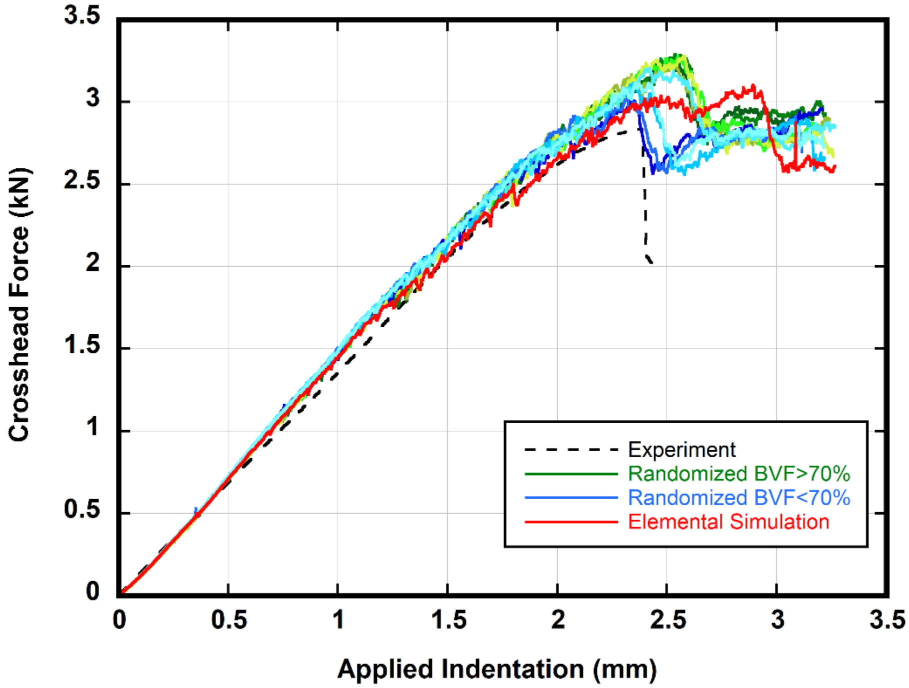

Fig. 25 Comparison of randomized simulations with Elemental Simulation run prior to randomization and based on in vivo configuration; randomized BVF>70% simulations (green) were the five simulations in Fig. 14, and randomized BVF<70% (blue) were the five simulations in Fig. 13

This conclusion that the randomization process scrambled internal porous structures was further demonstrated by the OT Randomized Simulations (shown in Fig. 16). In these simulations, only the OT was randomized. However, the OT had very few pores or clusters of low-BVF elements larger than the element size. Therefore, the randomized redistribution process for the OT did not significantly disarrange porous structures compared with when the process was applied to the MD or IT, which originally had many porous structures prior to randomization. As a result, the load-displacement responses from the OT Randomized Simulations were closely aligned (indeed, basically indistinguishable) from the Elemental Simulation, in contrast to the randomized simulations shown in Fig. 25 that noticeably deviated from the Elemental Simulation.

5.5 Limitations and Assumptions

5.5.1 Time-Increment Dependence of Algorithm to Prevent Artificial Load Drops

The algorithm described in Section 3.3 for gradually reducing the stress of TFHB elements caused the stress reduction of these elements to depend on the size of the time increment. Specifically, the method of reducing the stress was based on decreasing the Young's modulus over each time increment starting from failure. The number of time increments over which the stress of any particular TFHB element was reduced from the value at failure to a value of 0 was dependent only the magnitude of the stress and the prespecified values of the algorithm parameters. The number of time increments for stress reduction was insensitive to the size of the time increment. Therefore, if Simulation B had a time increment equal to half of that in Simulation A, the Young's modulus of a given element would still go to zero in the same number of time increments in both simulations. This means that the stress of the element would go to zero in half the time in Simulation B compared with Simulation A. The effect of this time dependence cannot be known with certainty without further work, which would involve additional simulations with time increments specified to particular values to analyze the effect of the time increment on simulation outcomes.

5.5.2 Parameters in the Elemental and Three-Layer Simulations

We believe the simulation methods of this study are applicable for the majority of the cases, as per literature, if the porosity distribution across the thickness of the skull follows a binomial distribution with dense outer and inner tables sandwiching a more-porous middle layer (as in Fig. 9). However, we had found in previous studies that for some areas of the skull for a minority of individuals, the through-thickness porosity distribution may not be able to be approximated as a Three-Layer system (Alexander et al. 2020a).

5.5.3 Limitations from Simplified FE Modeling Concept

The skullcap simulations presented here were subject to the same limitations as for the OSS. These limitations have been documented and discussed in full in Section 4.4.3 of Weerasooriya and Alexander (2021). Likewise, the Young's modulus and failure-strength values were compared with previous literature (Sections 4.2 and 4.3 of the previous document). Here, only the key difference is reiterated for completeness. One of the key differences between the BVF-dependent relationships for mechanical properties used in the present simulations and previous literature is the hierarchy of failure thresholds. The relationships used here suggest bone is strongest in tension and weakest in shear. Reviews by Gibson and Ashby (1997) and Morgan et al. (2018) of previous experimental studies also indicate that bone is weakest in shear but strongest in compression, rather than tension. This difference could be due to the limitations of the present skullcap simulations.

In particular, a constant Poisson's ratio of 0.3 was used for all elements within the skull, regardless of the BVF of the element. Therefore, any variation of Poisson's ratio was not accounted for. However, the apparent Poisson's ratio likely changes in increasing the BVF from 1% to 100%, and this BVF-dependence may be different than the modulus-BVF dependence (Yang et al. 1998; Yoon et al. 2002). Scaling the Poisson's ratio by the BVF could have led to a softer response of the diploe to compression. A softer diploe response may have allowed for a higher compressive-failure threshold to be used. The compressive-failure threshold may have even been higher than the tensile threshold, thereby modeling the skull as strongest in compression and reconciling the hierarchy of failure thresholds with the reviews of Gibson and Ashby and Morgan et al., as described previously.

Also, this may question our ability to directly use the information from idealized uniaxial experimental response for multiaxial loading situations.

6. Conclusions

An algorithm for slowing down the failure of tension-failed elements was implemented into the custom user subroutine (VUMAT) for calculating stress. This algorithm successfully delayed and dampened the catastrophic load drops in the skullcap simulation, thus allowing the load-displacement response to more closely match the experiment. In addition, aligning the POI in the simulation to that in the experiment enabled a close match of the BF displacement contours, and only required the compressive and failure thresholds to be reduced by less than 15%. The updated BVF-dependent properties summarized in Table 7 are suggested to be used in studies using the Elemental Approach.

The simulation that represented the skullcap with a completely Elemental Approach was transitioned into the Three-Layer Approach, which could be used to conserve computational expense by increasing element size. The response using the Three-Layer Approach indicated this option provides a suitable alternative if the research goal is only in representing the load-displacement of the skull bone. However, the approach may not be sufficient for studying failure patterns in the skull. Failure occurred by a shear-punch mechanism, in sharp contrast to the linear tensile failure observed experimentally and well modeled by the Elemental Approach.

The key to the difference in failure mechanisms was in modeling the inner table. The Three-Layer Approach represented the IT as a single homogeneous material. The absence of low BVF regions within the IT prevented the initiation and propagation of the linear tensile cracks. Indeed, in the hybrid Elemental–Three-Layer Simulations the shear-punch-failure type was avoided, and linear tensile cracks were noticeable, whenever the IT was modeled using the Elemental Approach. Therefore, researchers could implement a hybrid approach with the IT represented with element-to-element BVF variability in key regions of interest.

A method was demonstrated to investigate the effects of biovariability on skull response by randomizing the element-BVF assignments. The method reused the same mesh and only changed the microstructure. By avoiding any remeshing, it was relatively high-throughput compared with traditional method of scanning each skull and then building patient-specific meshes. It could be used to generate large data sets to mimic inter-Soldier biovariability, such as those required for recognizing material response through novel optimization methods like neural-network-based machine learning and artificial intelligence.

However, the method was based on a first-generation randomization process, which simply redistributed elemental BVF values within the specimen. This process, based only on values, disrupted internal porous structures present in the in vivo configuration. The outcomes from the randomized simulations demonstrated these internal porous structures were critical to the mechanical response of the skull. Therefore, future work should focus on developing a more-advanced process for randomizing the microstructures based not only on values but also quantified arrangements such as pore-size distribution and number of pores per unit volume. The process should keep the original intrinsic porous structure intact perhaps by moving element clusters that define a pore together, thus keeping pore-size distribution intact. However, to develop and apply such a process, additional research is needed to quantitatively define the critical intrinsic-porous structure. Once the signature of the structure is quantified and verified by studying different populations, such a quantifier or quantifiers can be used to identify the population as a whole or subcategories such as age groups, gender groups, and so on. One can identify these statistically different quantifiers for each subgroup. The updated randomizing algorithm could then be applied to any subgroup with similar signature and study the biovariability within this subgroup.

7. References

Abderezaei J, Zhao W, Grijalva CL, Fabris G, Ji S, Laksari K, Kurt M. Nonlinear dynamical behavior of the deep white matter during head impact. Phys Rev App. 2019;12(1):014058.

Alexander SL, Rafaels K, Gunnarsson CA, Weerasooriya T. Structural analysis of the frontal and parietal bones of the human skull. J Mech Beh Biomed Mat. 2019;90:689–701. https://doi.org/10.1016/j.jmbbm.2018.10.035.

Alexander SL, Gunnarsson CA, Rafaels K, Weerasooriya T. Multiscale response of the human skull to quasi-static compression. J Mech Beh Biomed Mat. 2020a;102. https://doi.org/10.1016/j.jmbbm.2019.103492.

Alexander SL, McKee PJ, Weerasooriya T. Micro-CT-based Three-Layer Finite Element Model for quasi-static human skull impact. CCDC Army Research Laboratory (US); 2020b May 1. https://apps.dtic.mil/sti/pdfs/AD1100519.pdf.

Alexander SL, Weerasooriya T. Implementation and validation of finite element model of skull deformation and failure response during uniaxial compression. J Mech Beh Biomed Mat. 2021;115:104302. https://doi.org/10.1016/j.jmbbm.2020.104302.

Boruah S, Subit DL, Paskoff GR, Shender BS, Crandall JR, Salzar RS. Influence of bone microstructure on the mechanical properties of skull cortical bone—a combined experimental and computational approach. J Mech Beh Biomed Mat. 2017;65:688–704.

Brown AD, Rafaels KA, Weerasooriya T. Shear behavior of human skull bones. J Mech Beh Biomed Mat. 2021;116:104343. https://doi.org/10.1016/j.jmbbm.2021.104343.

Chattopadhyay S, Tripathi C. Skull fracture and haemorrhage pattern among fatal and nonfatal head injury assault victims–a critical analysis. J Inj Vio Res. 2010;2(2):99.

Cotton RT, Pearce CW, Young PG, Kota N, Leung AC, Bagchi A, Qidwai SM. Development of a geometrically accurate and adaptable finite element head model for impact simulation: the Naval Research Laboratory–Simpleware Head Model. Comp Met Biomech Biomed Eng. 2016;19(1):101–113.

Deck C, Willinger R. Improved head injury criteria based on head FE model. Int J Crash. 2008;13(6):667–678.

Gibson LJ, Ashby MF. Cellular solids: structure and properties. Cambridge University Press; 1997.

Gunnarsson CA, Alexander SL, Weerasooriya T. Bending response of human skull-beams as a function of loading rate and loading-tip geometry. DEVCOM Army Research Laboratory (US); 2021a July. Report No.: ARL-TR-9215. https://apps.dtic.mil/sti/pdfs/AD1142091.pdf.

Gunnarsson CA, Alexander SL, Weerasooriya T. Mechanical response and fracture of human skull to blunt indentation loading. DEVCOM Army Research Laboratory (US); 2021b Feb 3. Report No.: ARL-TR-9142. https://apps.dtic.mil/sti/pdfs/AD1122025.pdf.

Hajiaghamemar M, Wu T, Panzer MB, Margulies SS. Embedded axonal fiber tracts improve finite element model predictions of traumatic brain injury. Biomech Mod Mechanobio. 2020;19(3):1109–1130.

Lozano-Mínguez E, Palomar M, Infante-García D, Rupérez MJ, Giner E. Assessment of mechanical properties of human head tissues for trauma modelling. Int J Num Met Biomed Eng. 2018;34(5):e2962.

Morgan EF, Unnikrisnan GU, Hussein AI. Bone mechanical properties in healthy and diseased states. Ann Rev Biomed Eng. 2018;20:119–143.

Ptak M, Ratajczak M, Kwiatkowski A, Sawicki M, Wilhelm J, Fernandes FA, Druszcz A. Investigation of biomechanics of skull structures damages caused by dynamic loads. Acta Bioeng Biomech. 2018;20(4):143–150.

Tse KM, Tan LB, Lee SJ, Lim SP, Lee HP. Development and validation of two subject-specific finite element models of human head against three cadaveric experiments. Int J Num Met Biomed Eng. 2014;30(3):397–415.

Weerasooriya T, Alexander SL. Hybrid experimental-modeling-computational (HEMC) concept: determine skull fracture. DEVCOM Army Research Laboratory (US); 2020 Dec. Report No.: ARL-TR-9125. https://apps.dtic.mil/sti/pdfs/AD1118637.pdf.

Weerasooriya T, Alexander S. Mechanism and microstructure based concept to predict skull fracture using a hybrid-experimental-modeling-computational approach. J Mech Behav Biomed Mat. 2021;121:104599. https://doi.org/10.1016/j.jmbbm.2021.104599.

Yang G, Kabel J, Van Rietbergen B, Odgaard A, Huiskes RI, Cown SC. The anisotropic Hooke’s law for cancellous bone and wood. J Elast. 1998;53(2):125–146.

Yoon YJ, Yang G, Cowin SC. Estimation of the effective transversely isotropic elastic constants of a material from known values of the material's orthotropic elastic constants. Biomech Mod Mechanobio. 2002;1(1):83–93.

Appendix A. Randomized Microstructures Based on Bone Volume Fraction (BVF)

A.1 Introduction

This appendix contains the failure patterns for simulations that randomized the $f_{BV,0}$ values among elements based on the $f_{BV,0} = 70\%$ criterion. (The simulations were described in this report in Section 4.3.1, which also contained the load-displacement responses.) Failure patterns are included for an anterior–posterior cross section approximately under the point of indentation/impact (POI). Relative location of cross section within the skullcap was similar to what was shown in Fig. 1 of this report. Failure patterns are also included for the back face (BF) of the specimen, corresponding to a bottom-up view looking at the inner surface of the skullcap.

In the failure patterns, elements are color-coded by their status: active (not failed), failed by compression, failed by tension, or failed by shear. The mesh is in the undeformed configuration. Failure patterns are provided at three values of applied indentation: 1, 2, and 3 mm. Of these, only the patterns at 3 mm of applied indentation were after the catastrophic load drop.

The failure patterns from the Elemental Simulation are also included for comparison. These patterns are marked as "Before Randomizing", since the randomized simulations started from the Elemental Simulation and then randomly redistributed a subset of the $f_{BV,0}$ values.

A.2 Randomized among Elements with BVF < 70%

In these simulations, the $f_{BV,0}$ values were randomly redistributed among all elements with $f_{BV,0} < 70\%$. The simulations were referred to as Randomized #1 BVF<70% through Randomized #5 BVF<70%.

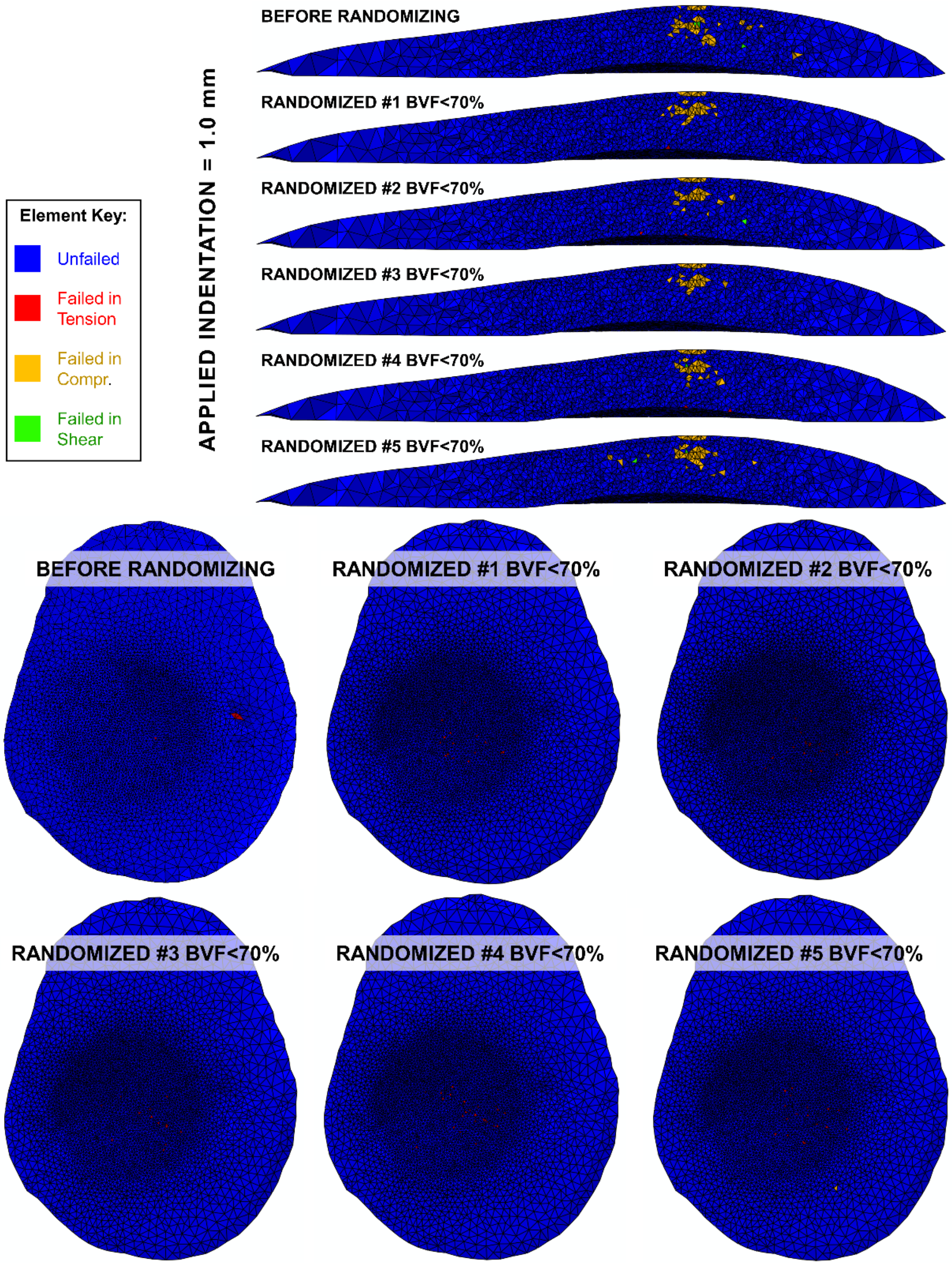

Fig. A-1 Cross-section and BF failure patterns at applied indentation of 1.0 mm; five simulations (Randomized #1–5) with randomized BVF assignments among elements with BVF < 70% are compared with Elemental Simulation (Before Randomizing)

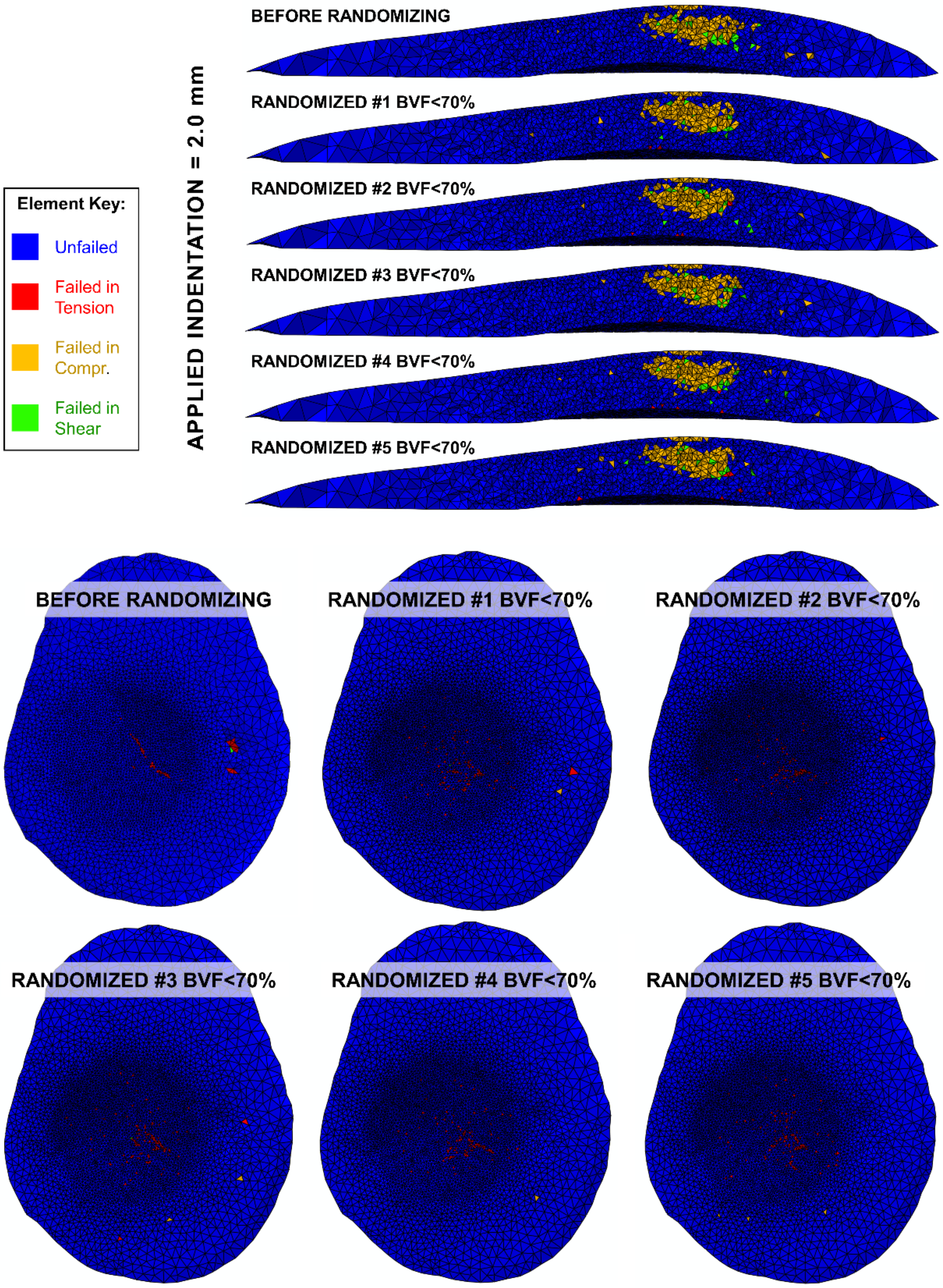

Fig. A-2 Cross-section and BF failure patterns at applied indentation of 2.0 mm; five simulations (Randomized #1–5) with randomized BVF assignments among elements with BVF < 70% are compared with Elemental Simulation (Before Randomizing)

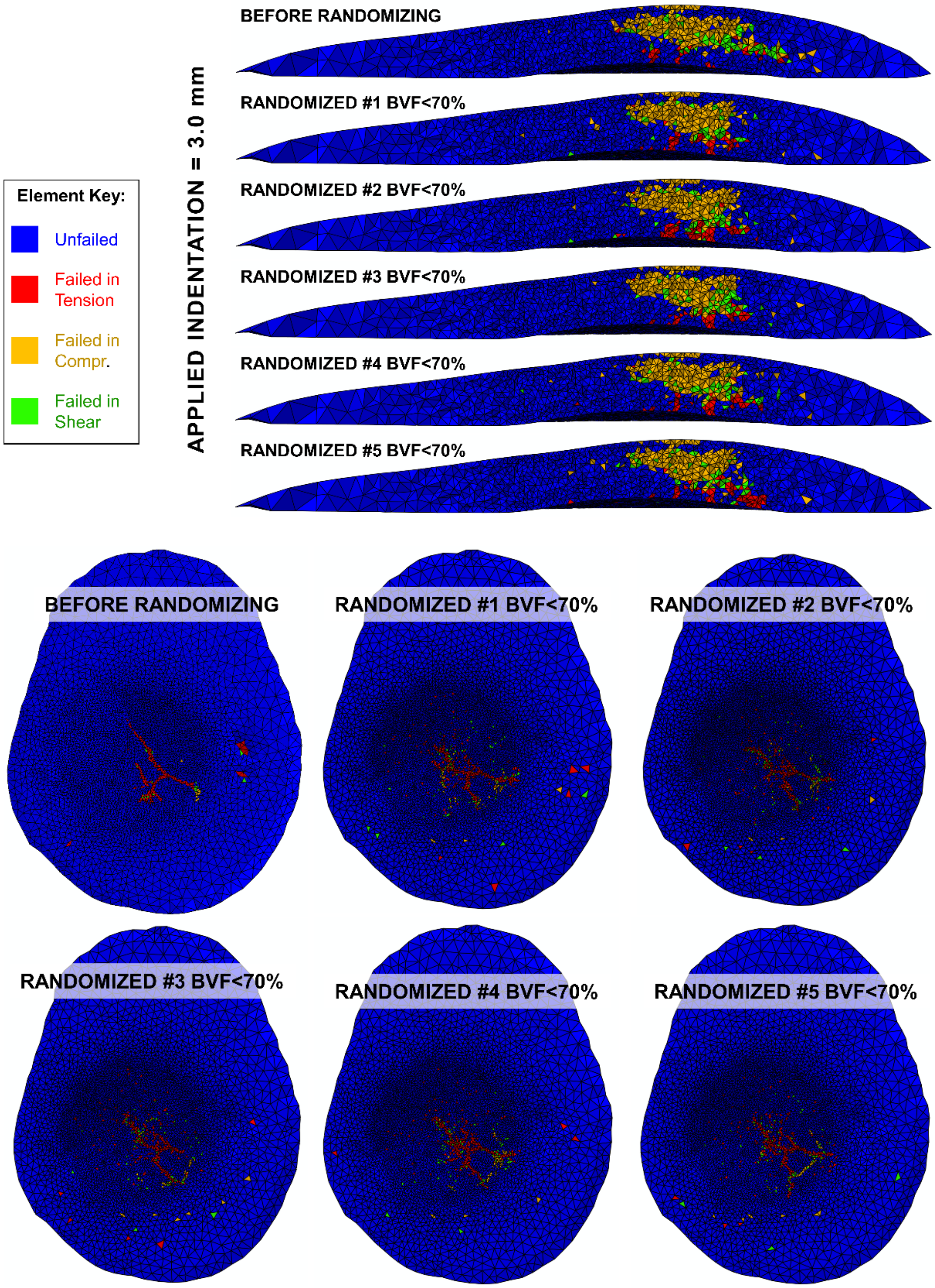

Fig. A-3 Cross-section and BF failure patterns at applied indentation of 3.0 mm; five simulations (Randomized #1–5) with randomized BVF assignments among elements with BVF < 70% are compared with Elemental Simulation (Before Randomizing)

A.3 Randomized among Elements with BVF > 70%

In these simulations, the $f_{BV,0}$ values were randomly redistributed among all elements with $f_{BV,0} > 70\%$. The simulations were referred to as Randomized no. 1 BVF>70% through Randomized no. 5 BVF>70%.

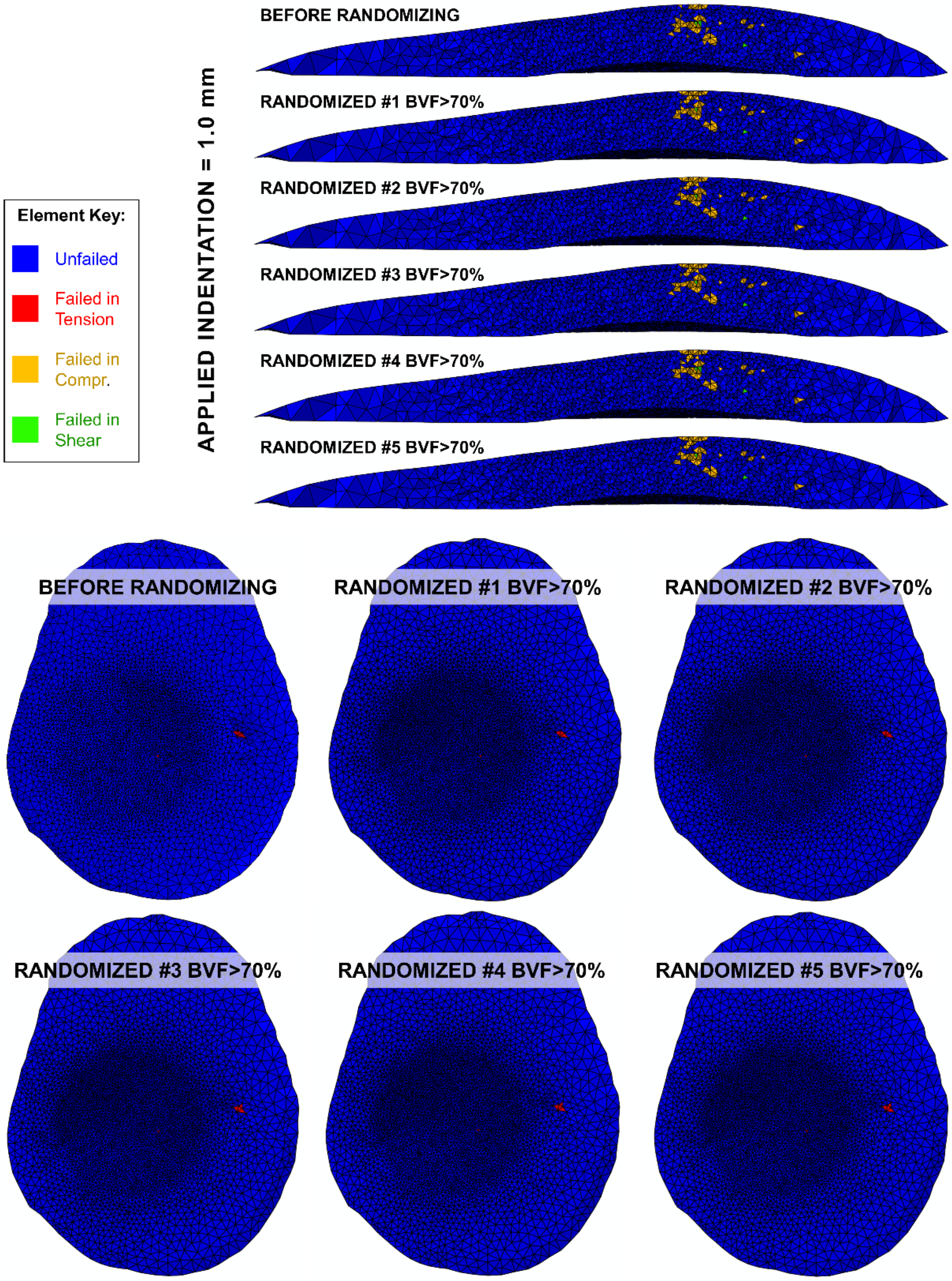

Fig. A-4 Cross-section and BF failure patterns at applied indentation of 1.0 mm; five simulations (Randomized #1–5) with randomized BVF assignments among elements with BVF > 70% are compared with Elemental Simulation (Before Randomizing)

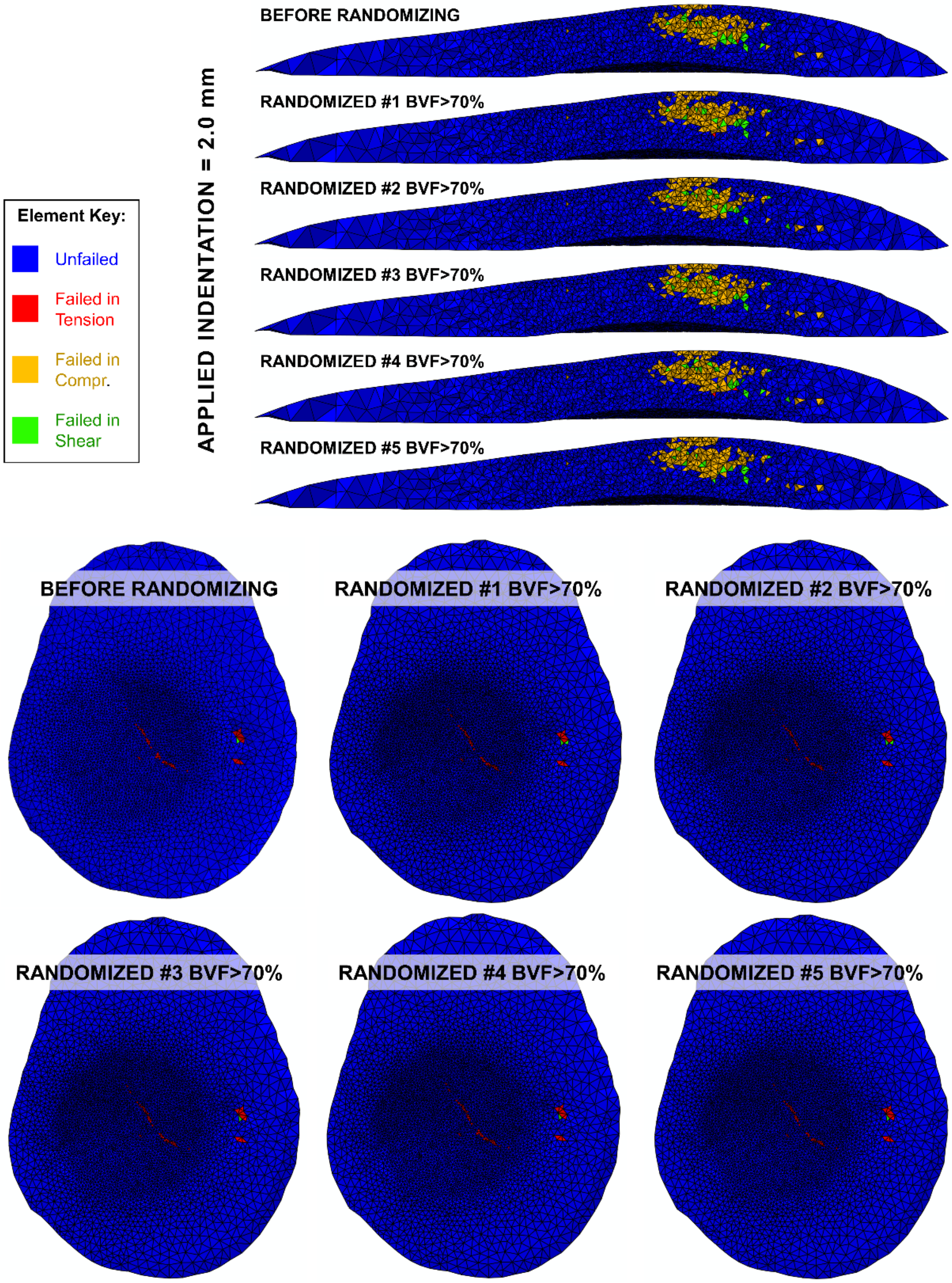

Fig. A-5 Cross-section and BF failure patterns at applied indentation of 2.0 mm; five simulations (Randomized #1–5) with randomized BVF assignments among elements with BVF > 70% are compared with Elemental Simulation (Before Randomizing)

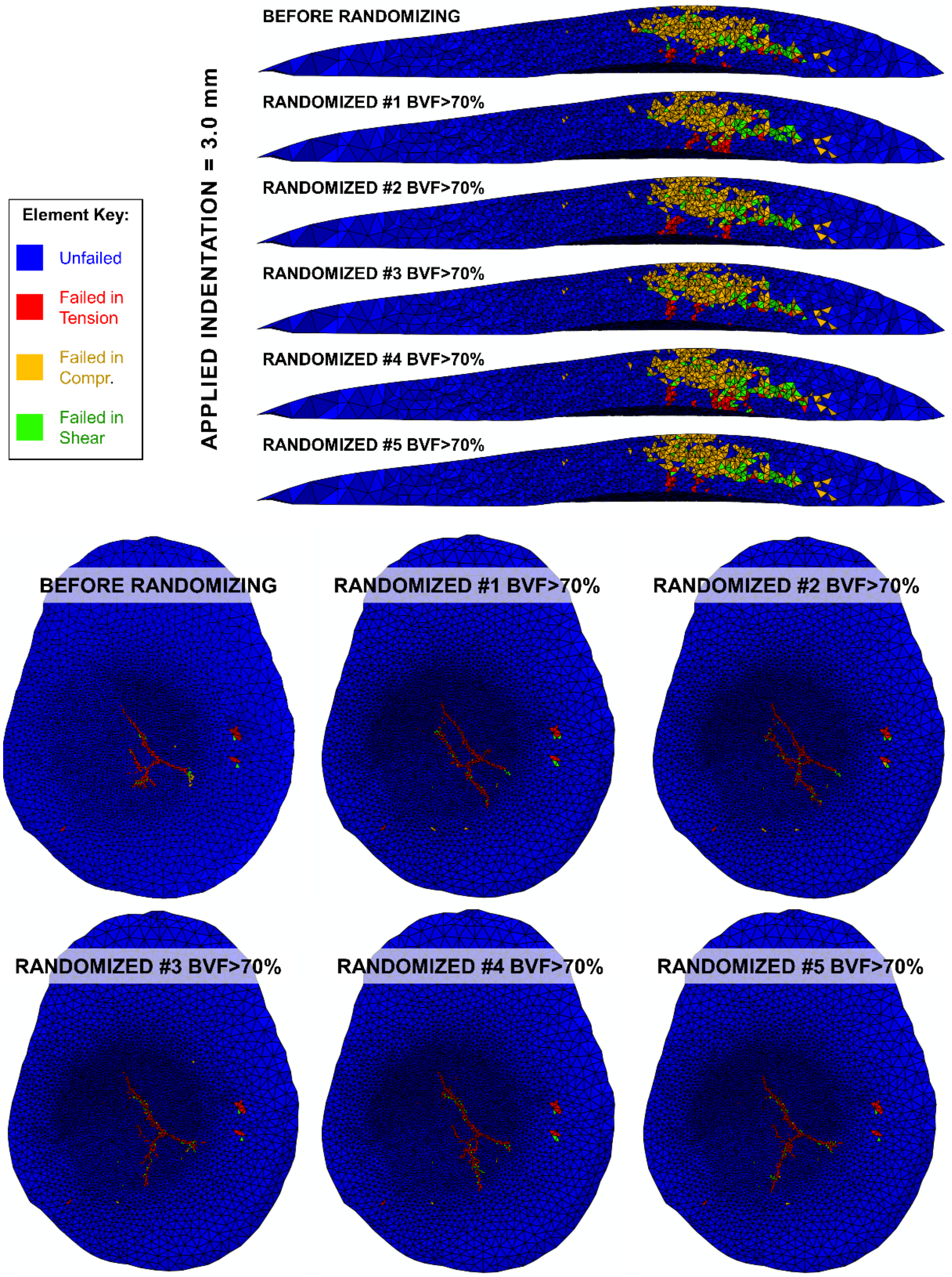

Fig. A-6 Cross-section and BF failure patterns at applied indentation of 3.0 mm; five simulations (Randomized #1–5) with randomized BVF assignments among elements with BVF > 70% are compared with Elemental Simulation (Before Randomizing)

Appendix B. Failure Patterns in Hybrid Simulations Compared with Elemental and Three-Layer Simulations

B.1 Overview of Hybrid Elemental and Three-Layer Simulations

This appendix contains the failure patterns from the hybrid simulations, which were described in Section 4.3.2. These simulations started with the Three-Layer Simulation. The Three-Layer Simulation consisted of four materials: the far zone (FZ), outer table (OT), mid-diploe (MD), and inner table (IT). In the hybrid simulations, either the OT layer or the IT layer or both the OT and IT layers were converted to the Elemental Approach, where each element within the layer(s) was assigned a $f_{BV,0}$ value based on the local microstructure. The hybrid simulations then randomized the $f_{BV,0}$ assignments among the elements in the converted layer(s). The different types of hybrid simulations are summarized in Table B-1.

Table B-1 Hybrid simulations

	Set A	Set B	Set C
Randomized Layer	Only OT	Only IT	OT and IT
Homogenous regions	MD, IT, and FZ	OT, MD, and FZ	MD and FZ
Simulation Names	OT Randomized #1	IT Randomized #1	OT&IT Randomized #1
	OT Randomized #2	IT Randomized #2	OT&IT Randomized #2
	OT Randomized #3	IT Randomized #3	OT&IT Randomized #3
	OT Randomized #4	IT Randomized #4	OT&IT Randomized #4
	OT Randomized #5	IT Randomized #5	OT&IT Randomized #5

Both cross-sectional and back-face (BF) failure patterns are included in this appendix. The cross section is in the anterior–posterior direction, similar to the cross-sectional view shown in Fig. 1. The BF represents the bottom-up view of the skullcap showing the inner surface, which was the opposite surface to the POI.

Failure patterns consist of the undeformed mesh geometry with elements color-coded by status: active (unfailed), failed by compression, failed by tension, or failed by shear.

B.2 Set A: Randomizing Only the OT

In Set A, the simulations were exactly like the Three-Layer Simulation, except that the OT was converted to an Elemental Approach. Each element in the OT had a $f_{BV,0}$ value based on the local microstructure. Then, the $f_{BV,0}$ values were randomly redistributed among all of the elements within the OT. The load-displacement response is shown in Fig. B-1. Cross-sectional and BF failure patterns are included in Sections B.2.1 and B.2.2, respectively. Failure patterns are provided at 1, 2, and 3 mm of applied displacement, as marked in Fig. B-1.

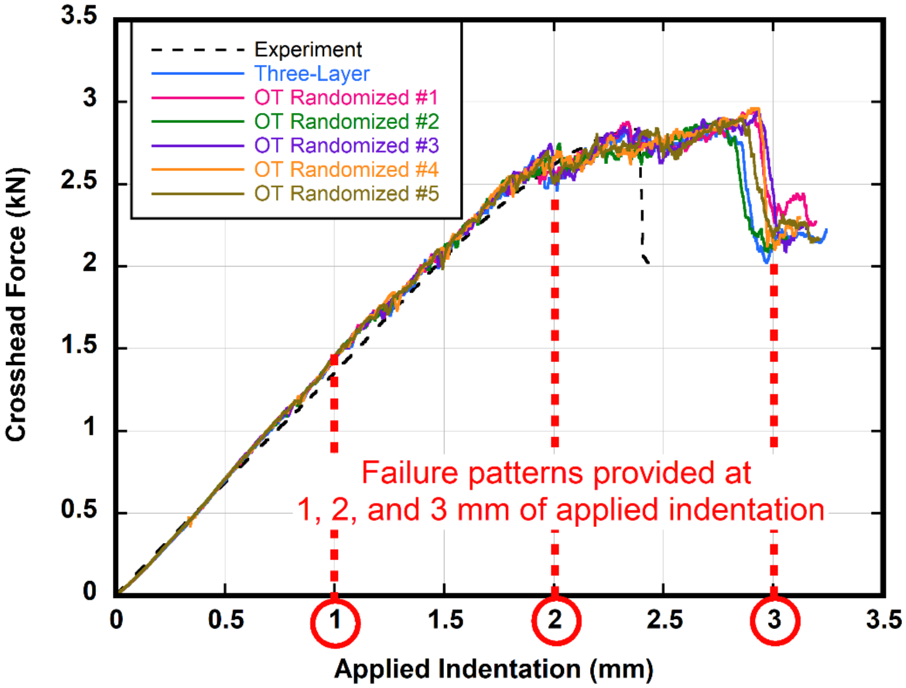

Fig. B-1 Load-displacement curve for Three-Layer Simulation and five hybrid simulations in Set A, where only the outer table was randomized (as defined in Table B-1)

B.2.1 Cross-Sectional Failure Patterns for Set A (Only OT Randomized)

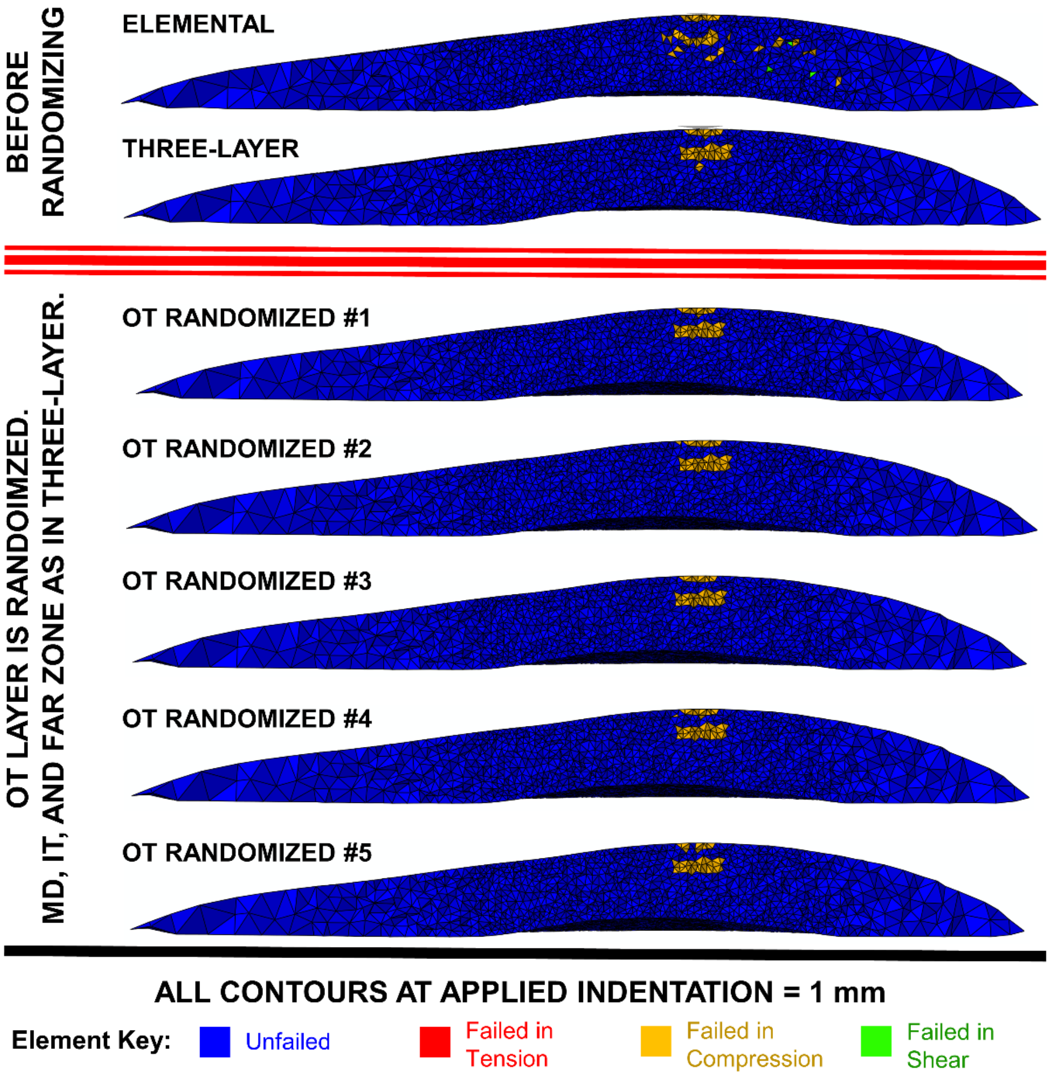

Fig. B-2 Cross-section failure patterns at applied indentation of 1.0 mm (Fig. B-1)

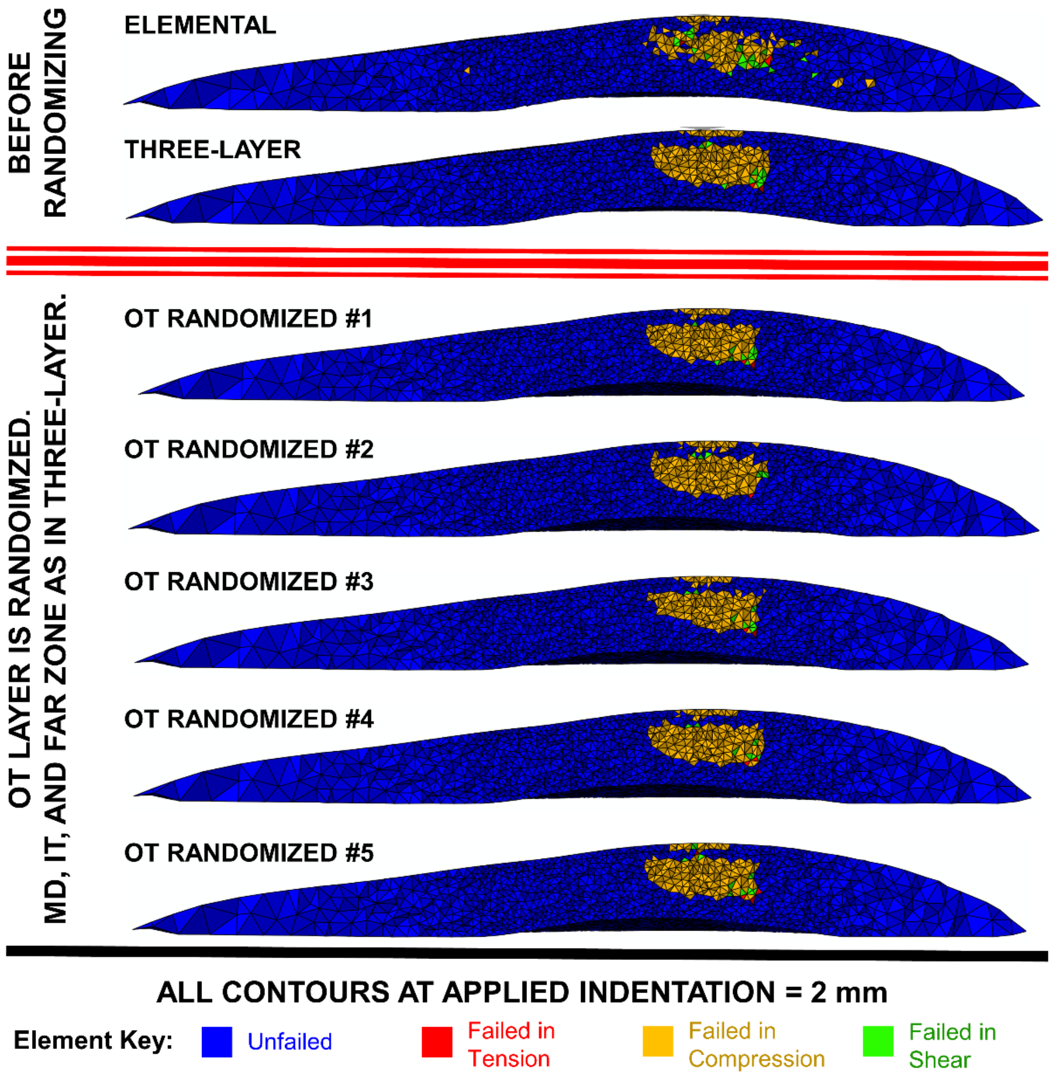

Fig. B-3 Cross-section failure patterns at applied indentation of 2.0 mm (Fig. B-1)

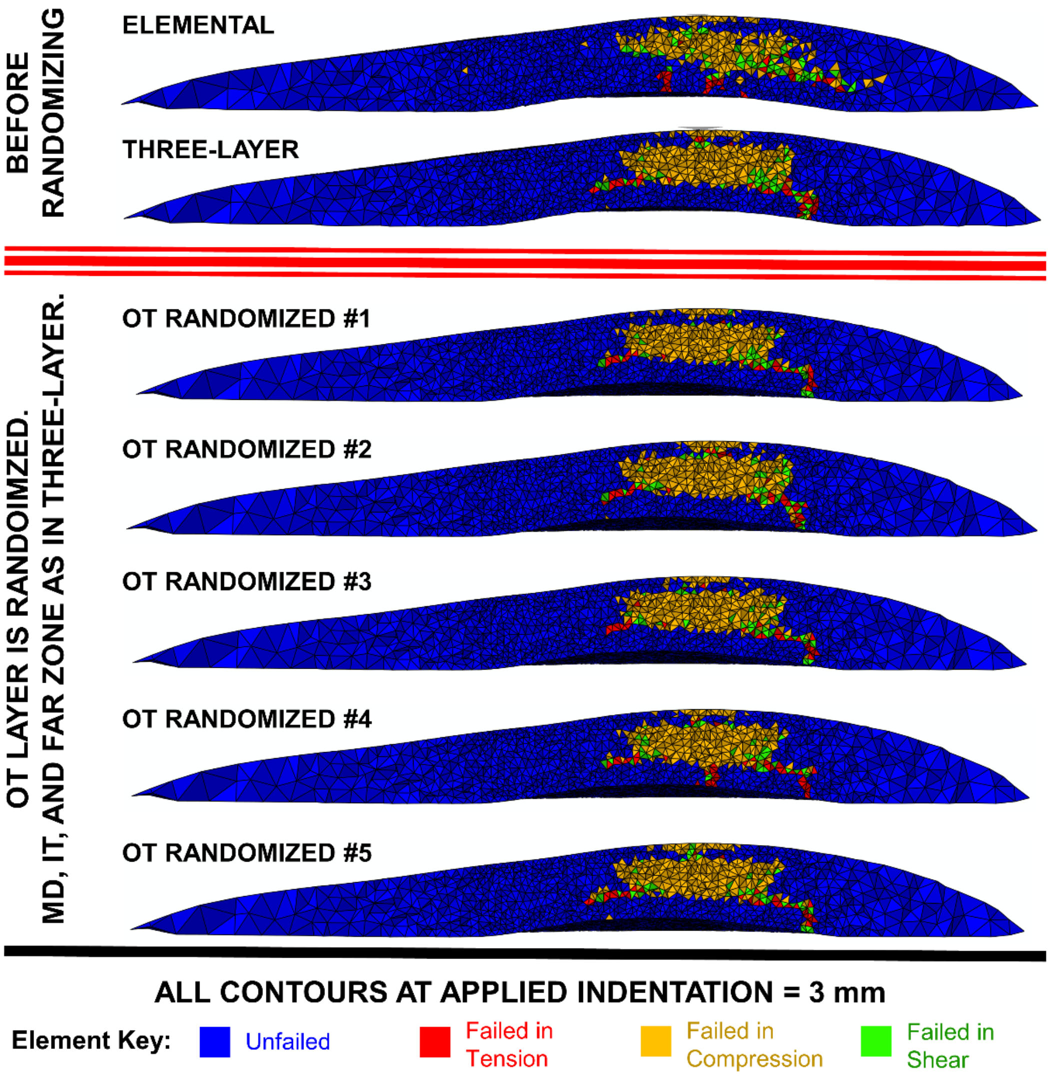

Fig. B-4 Cross-section failure patterns at applied indentation of 3.0 mm (Fig. B-1)

B.2.2 BF Failure Patterns for Set A (Only OT Randomized)

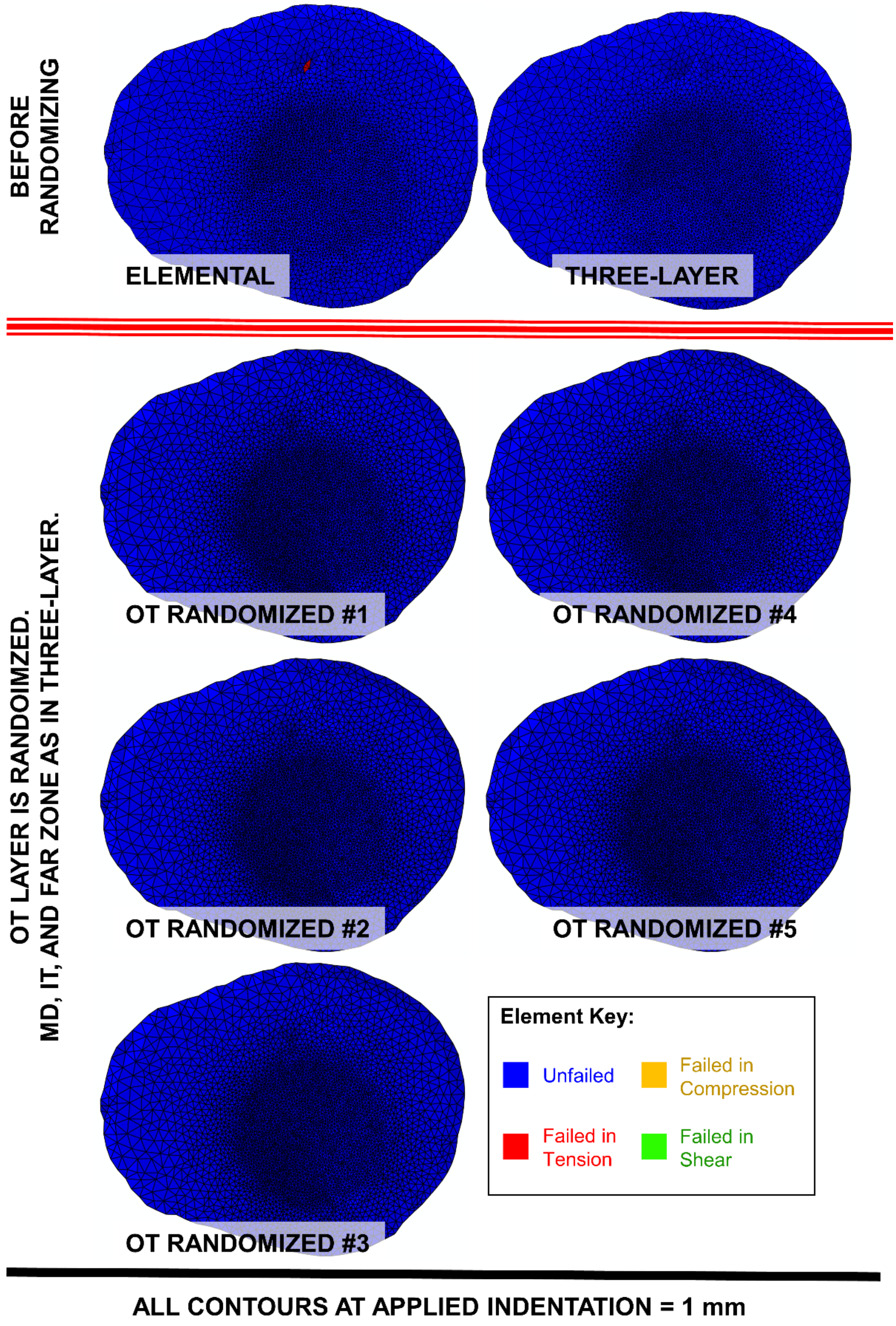

Fig. B-5 BF failure patterns at applied indentation of 1.0 mm (Fig. B-1)

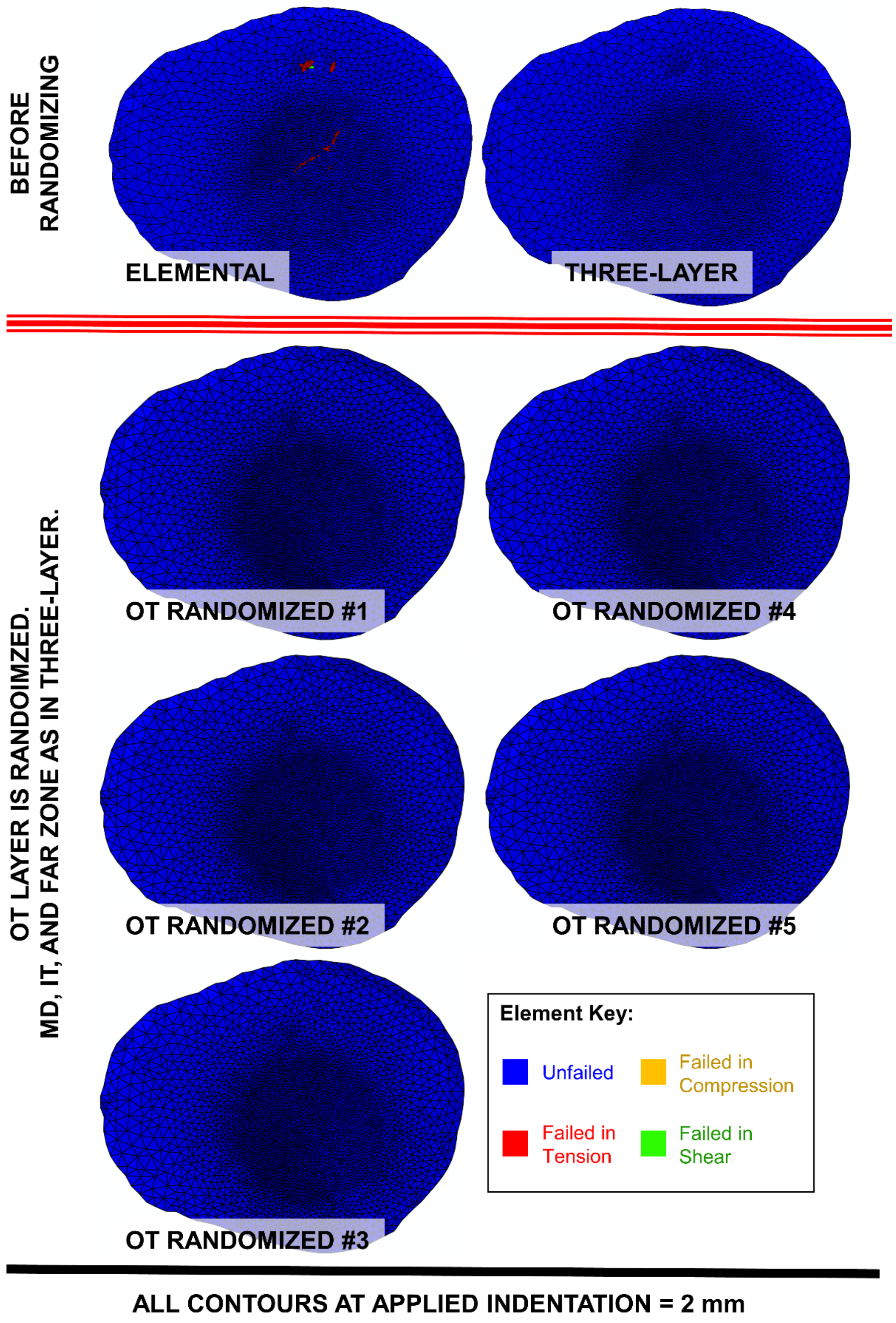

Fig. B-6 BF failure patterns at applied indentation of 2.0 mm (Fig. B-1)

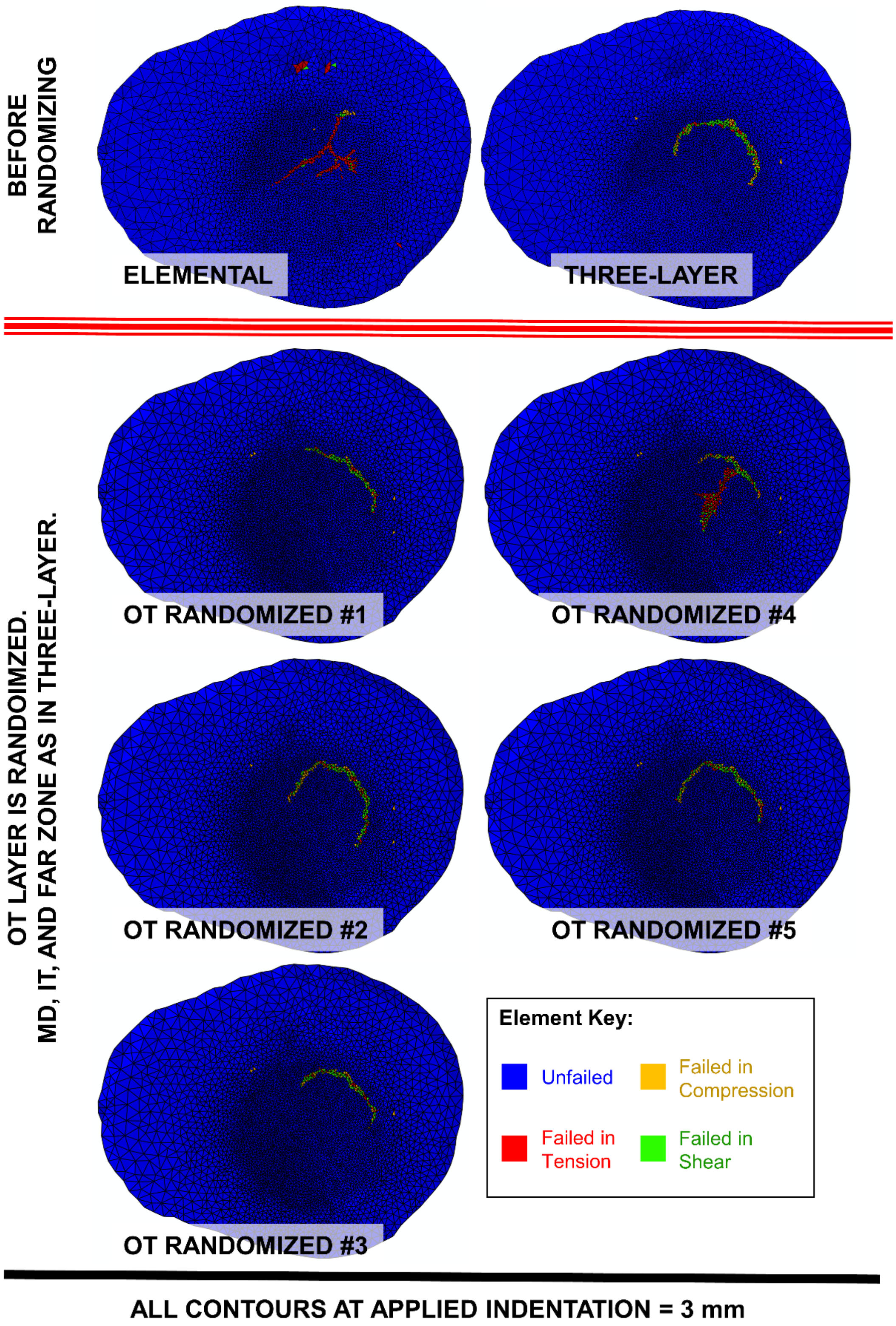

Fig. B-7 BF failure patterns at applied indentation of 3.0 mm (Fig. B-1)

B.3 Set B: Randomizing Only the IT

In Set B, the simulations were exactly like the Three-Layer Simulation, except the IT was converted to an Elemental Approach. Each element in the IT had a $f_{BV,0}$ value based on the local microstructure. Then, the $f_{BV,0}$ values were randomly redistributed among all of the elements within the IT. The load-displacement response is shown in Fig. B-8. Cross-sectional and BF failure patterns are included in Sections B.3.1 and B.3.2, respectively. Failure patterns are provided at 1, 2, and 3 mm of applied displacement, as marked in Fig. B-8.

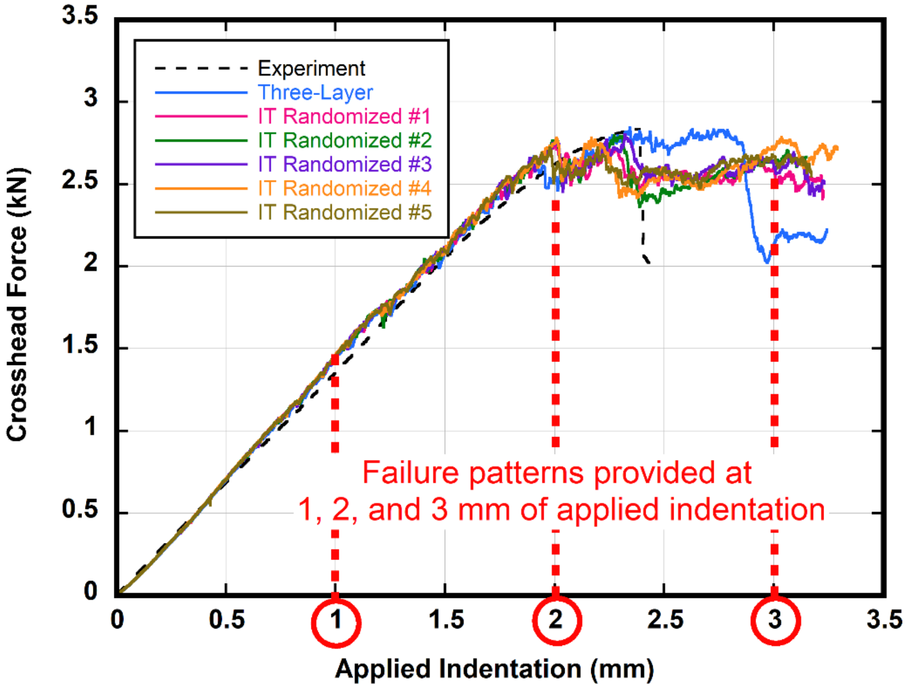

Fig. B-8 Load-displacement curve for Three-Layer Simulation and five hybrid simulations in Set B, where only the inner table was randomized (as defined in Table B-1)

B.3.1 Cross-Sectional Failure Patterns for Set B (Only IT Randomized)

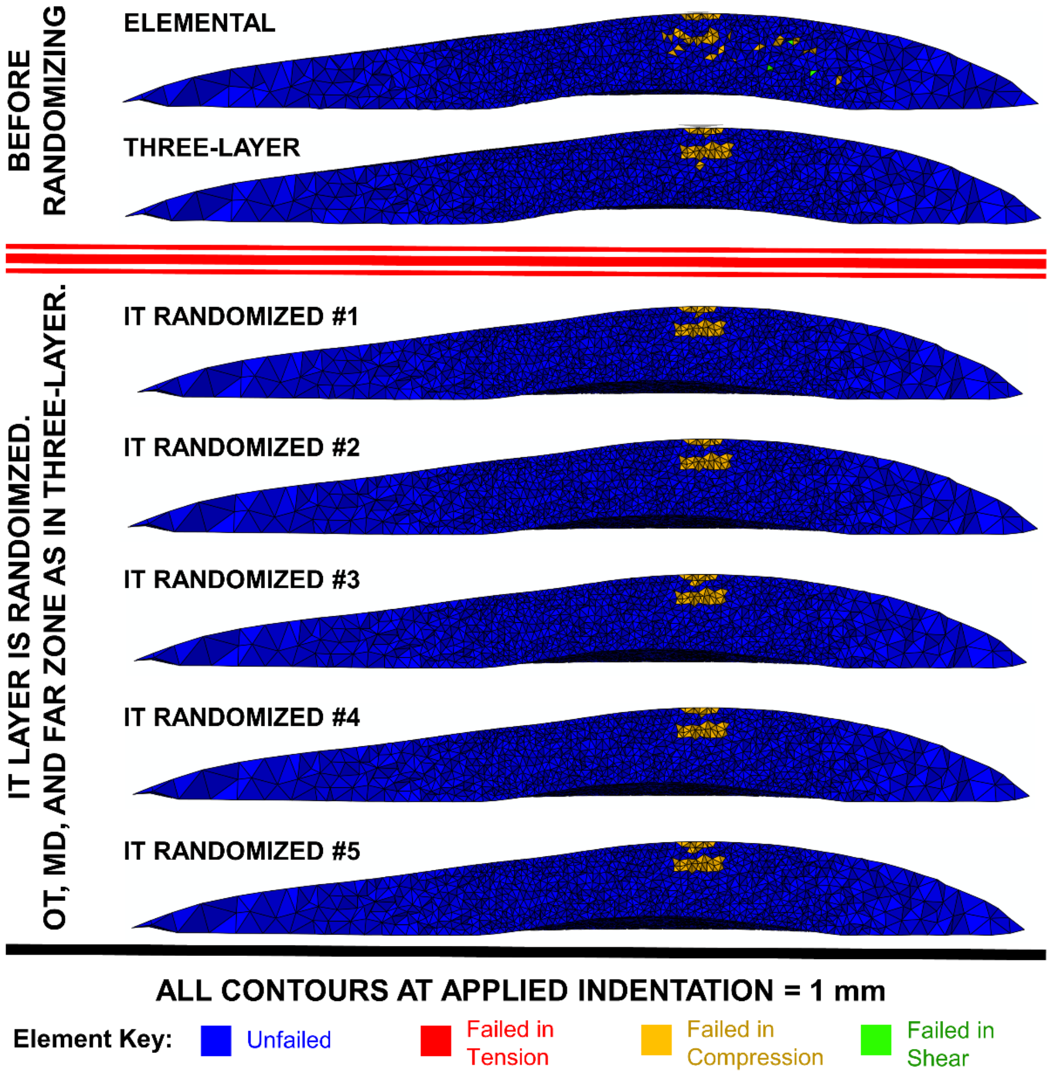

Fig. B-9 Cross-section failure patterns at applied indentation of 1.0 mm (Fig. B-8)

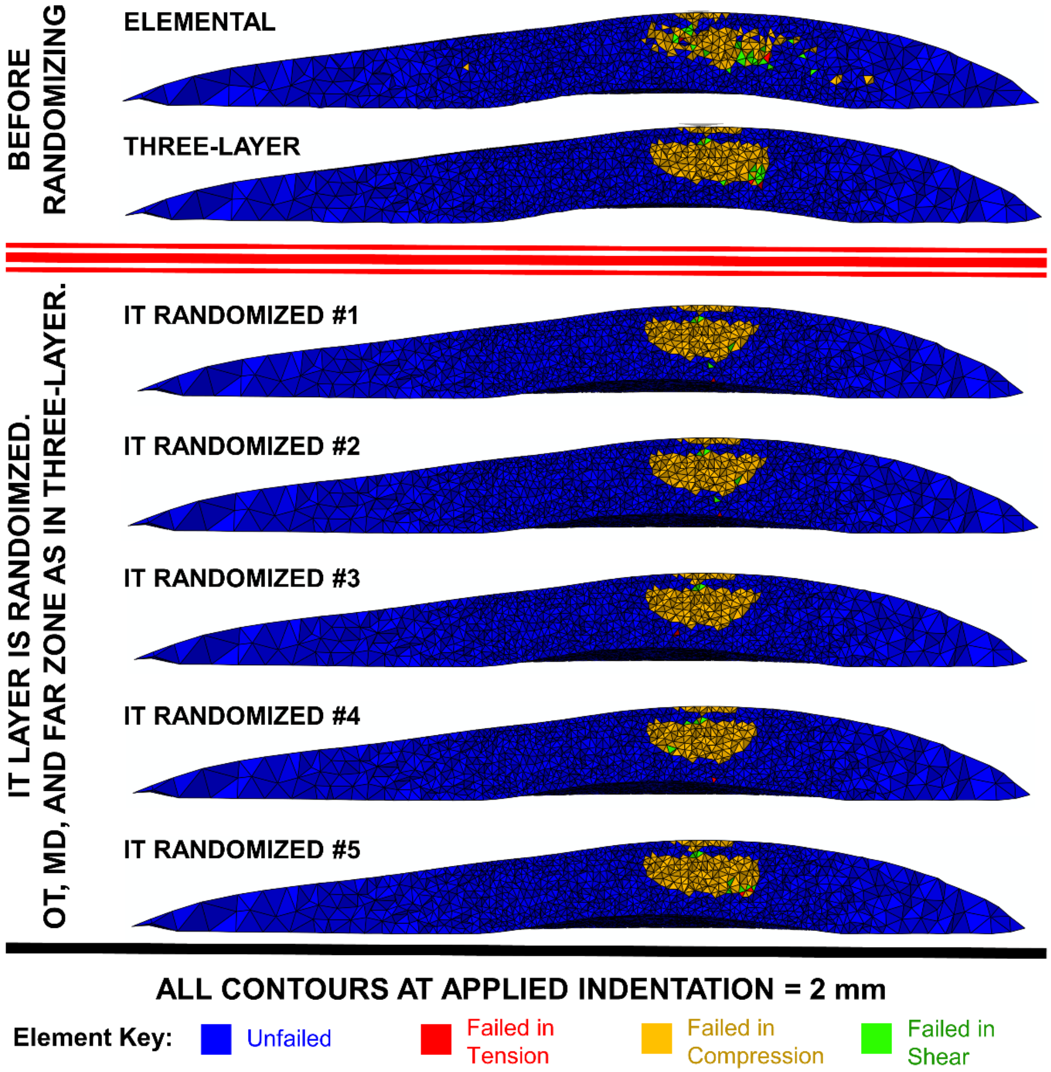

Fig. B-10 Cross-section failure patterns at applied indentation of 2.0 mm (Fig. B-8)

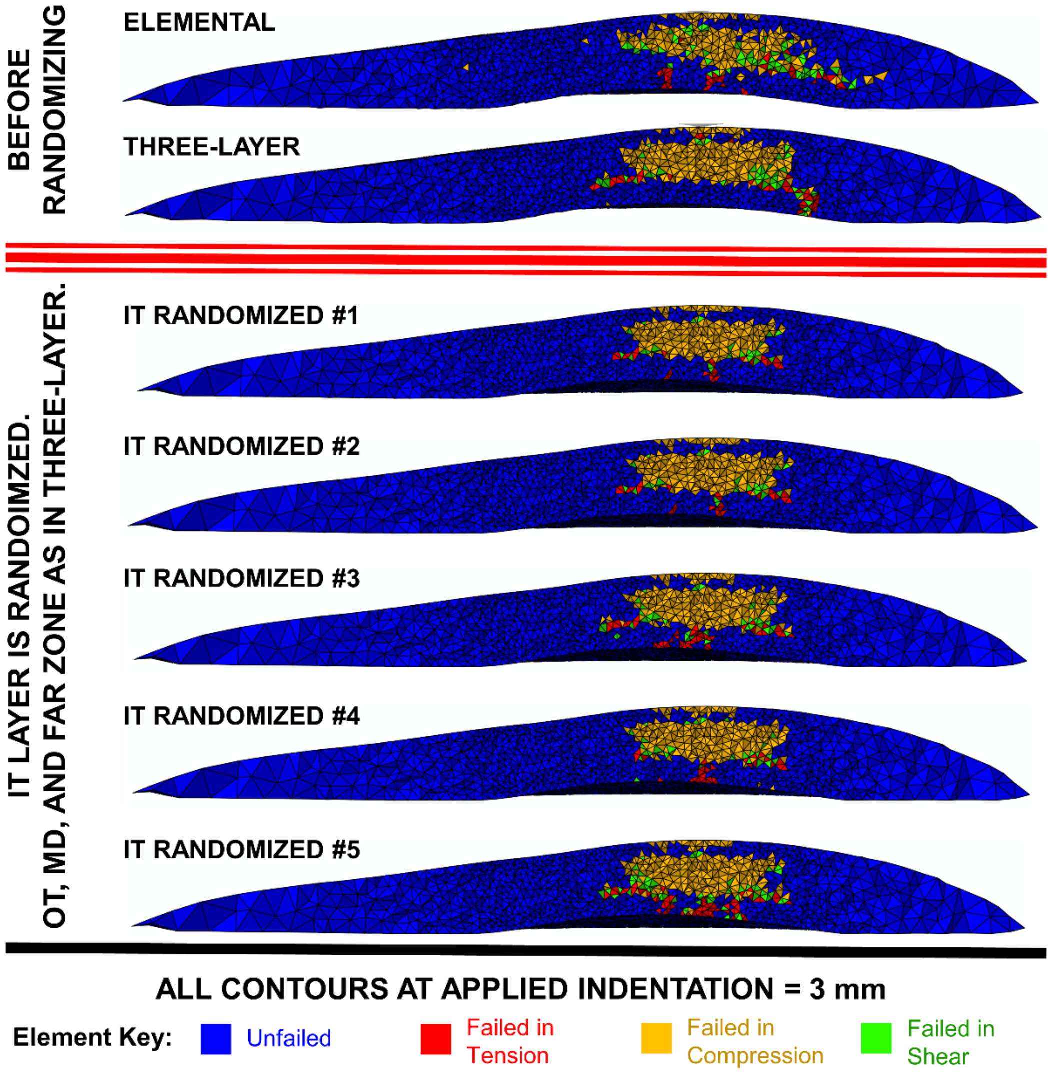

Fig. B-11 Cross-section failure patterns at applied indentation of 3.0 mm (Fig. B-8)

B.3.2 BF Failure Patterns for Set B (Only IT Randomized)

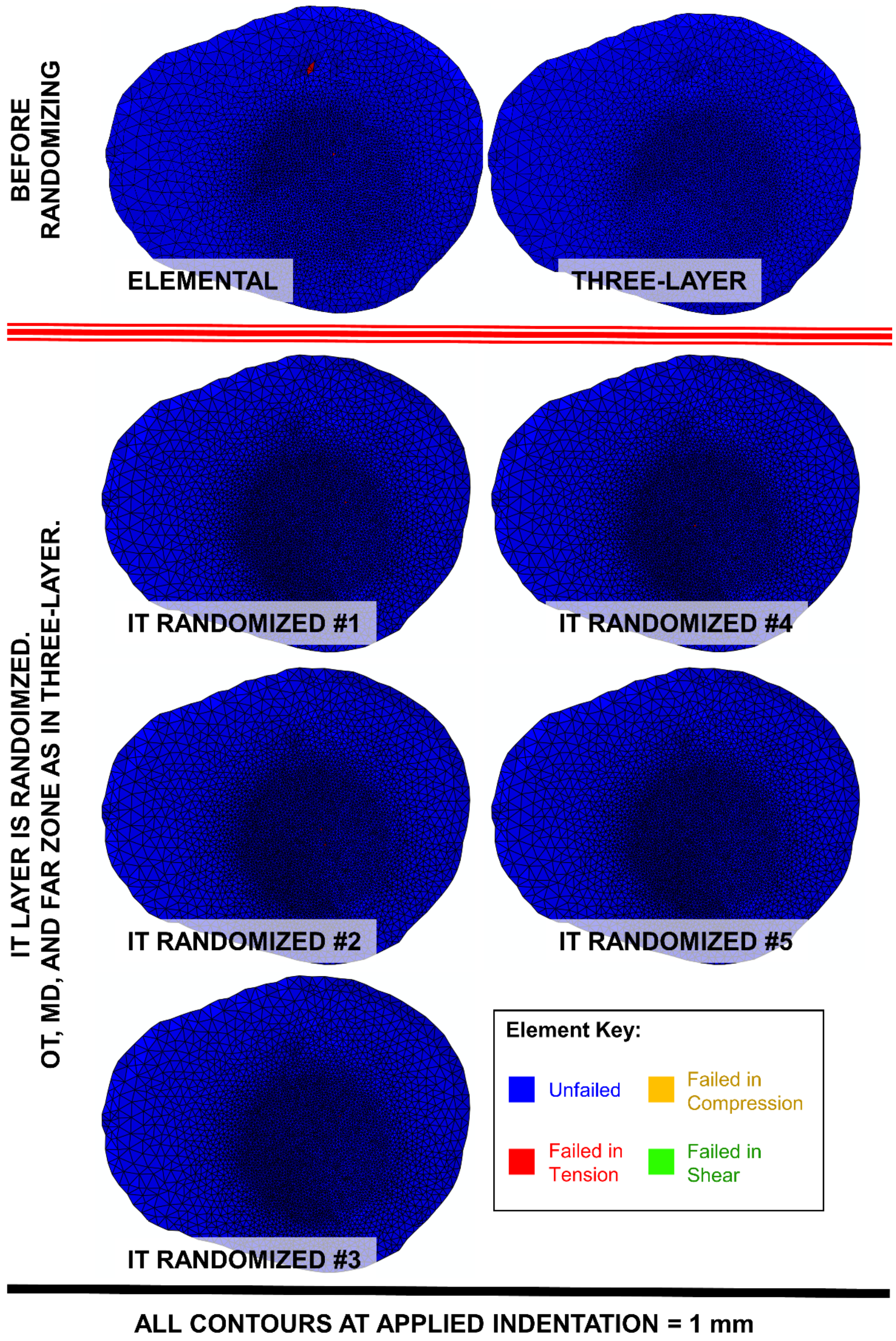

Fig. B-12 BF failure patterns at applied indentation of 1.0 mm (Fig. B-8)

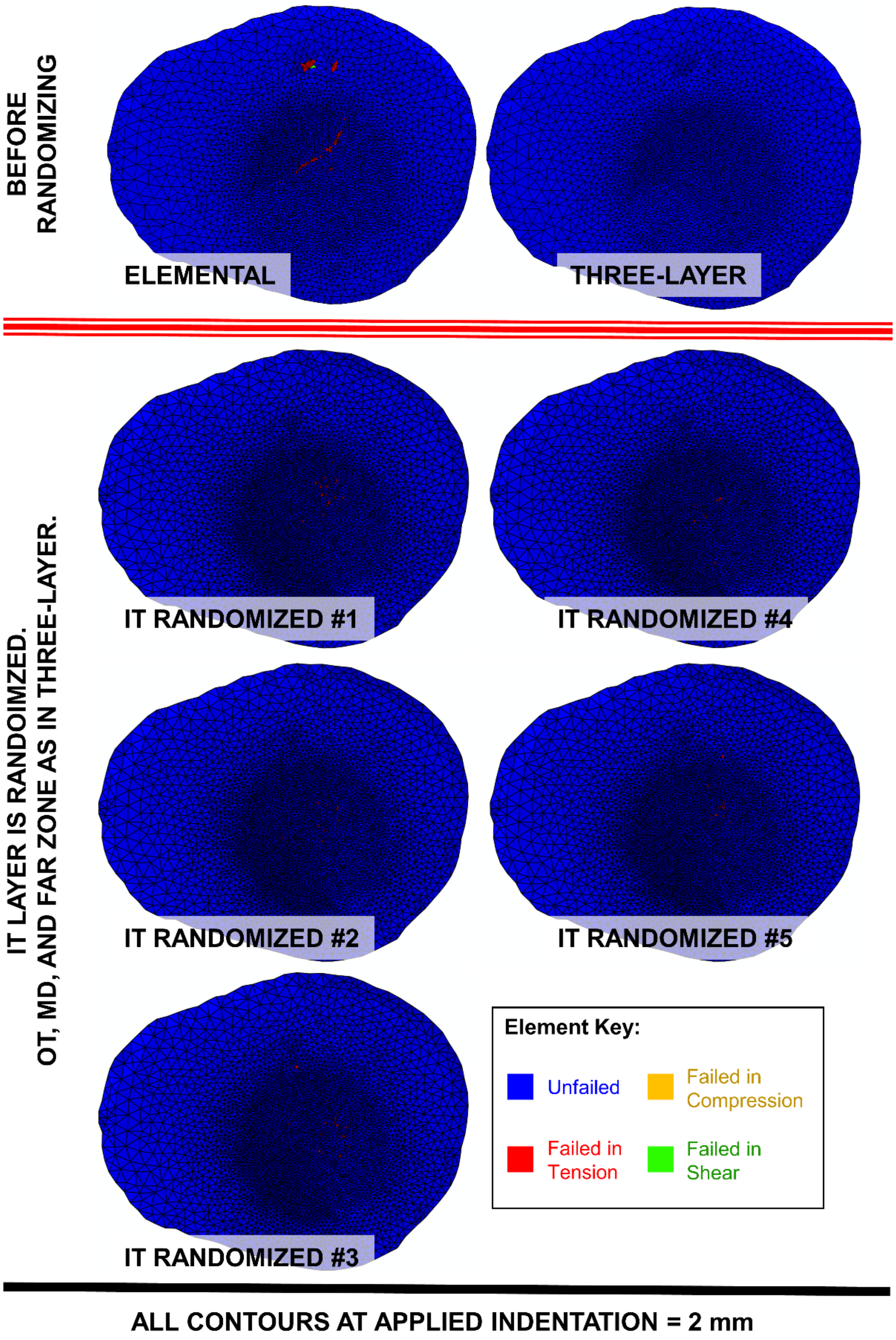

Fig. B-13 BF failure patterns at applied indentation of 2.0 mm (Fig. B-8)

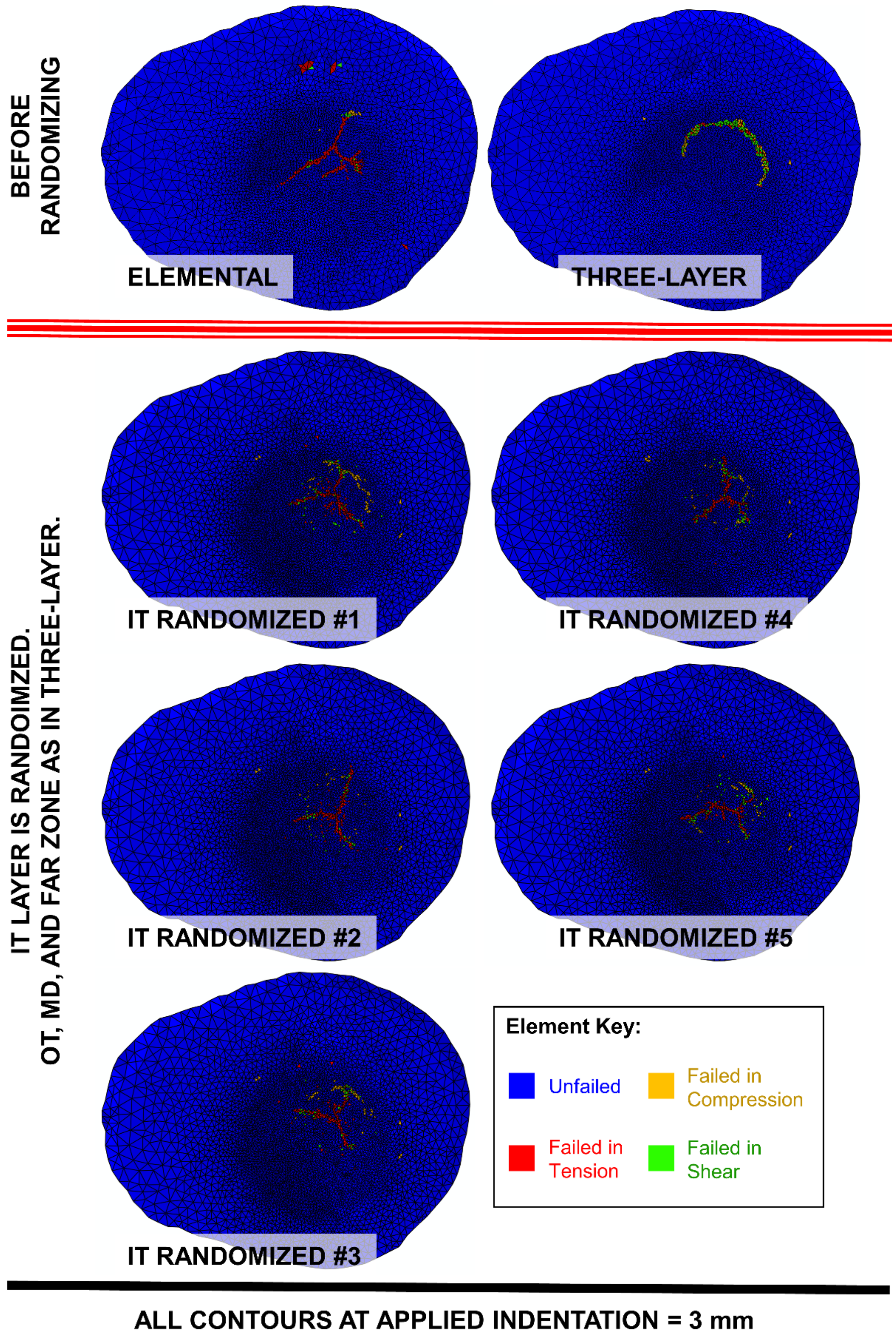

Fig. B-14 BF failure patterns at applied indentation of 3.0 mm (Fig. B-8)

B.4 Set C: Randomizing Both OT and IT

The hybrid simulations in Set C started from the Three-Layer Simulation and then converted both the OT and the IT to an Elemental Approach. The $f_{BV,0}$ values were randomly redistributed among all of the elements within the OT, and the random redistribution was repeated for all of the elements within the IT. The redistribution was only between elements of the same layer; there was no cross-talk between the IT and OT layers. The load-displacement response is shown in Fig. B-15. Cross-sectional and BF failure patterns are included in Sections B.4.1 and B.4.2, respectively. Failure patterns are provided at 1, 2, and 3 mm of applied displacement, as marked in Fig. B-15.

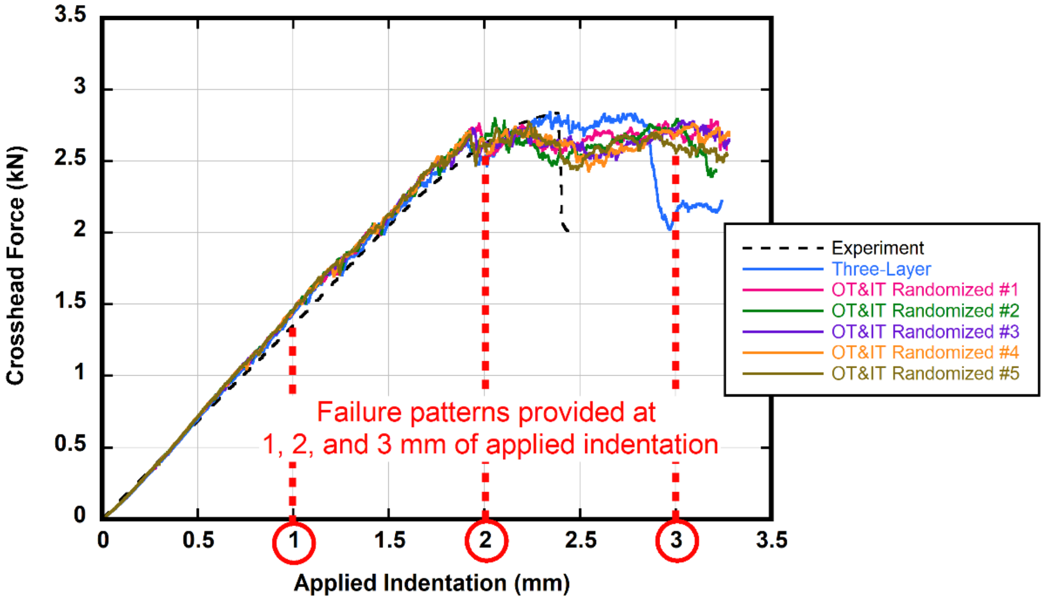

Fig. B-15 Load-displacement curve for Three-Layer Simulation and five hybrid simulations in Set C; element-BVF assignments were randomized among elements of OT and randomized among elements of IT (as defined in Table B-1)

B.4.1 Cross-Sectional Failure Patterns for Set C (IT and OT Randomized)

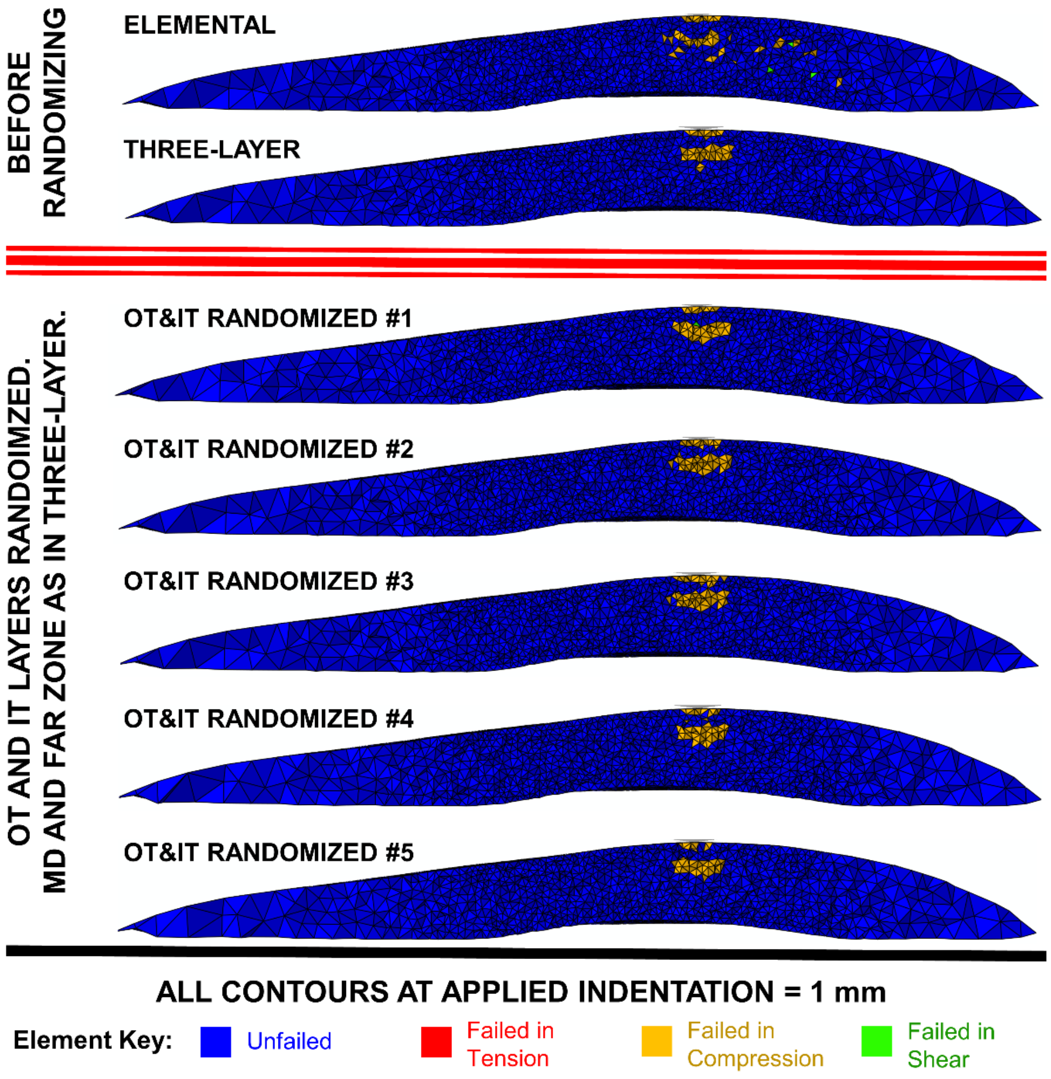

Fig. B-16 Cross-section failure patterns at applied indentation of 1.0 mm (Fig. B-15)

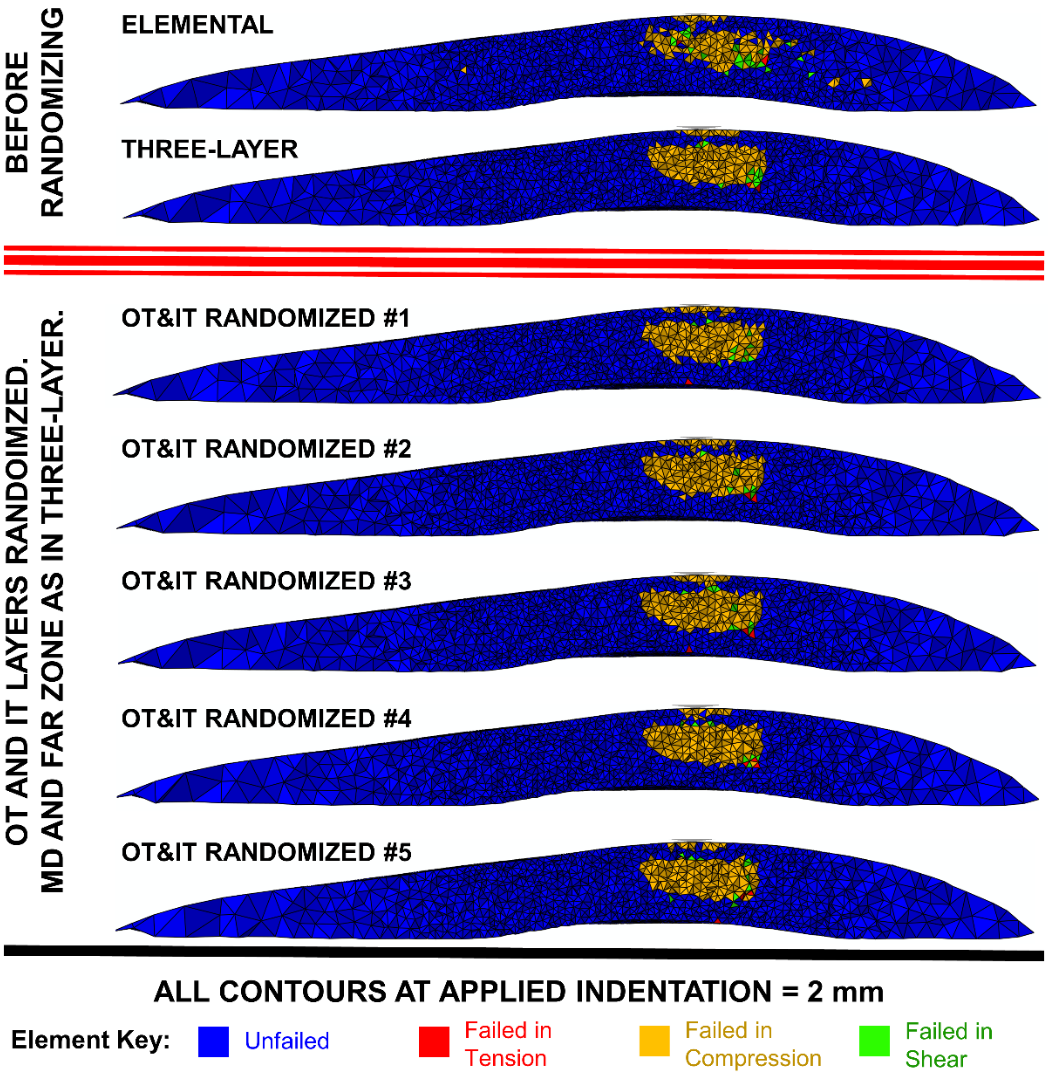

Fig. B-17 Cross-section failure patterns at applied indentation of 2.0 mm (Fig. B-15)

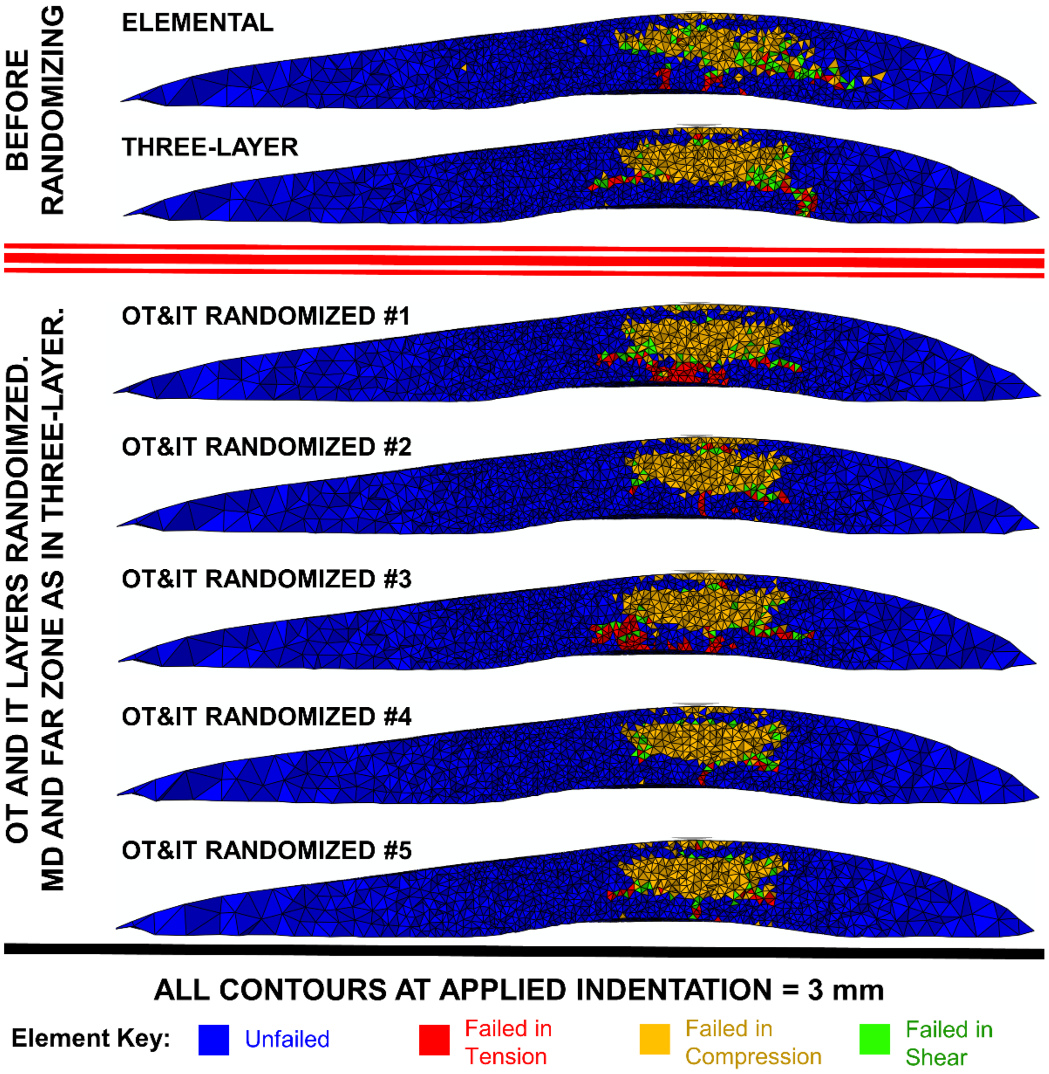

Fig. B-18 Cross-section failure patterns at applied indentation of 3.0 mm (Fig. B-15)

B.4.2 BF Failure Patterns for Set C (OT and IT Randomized)

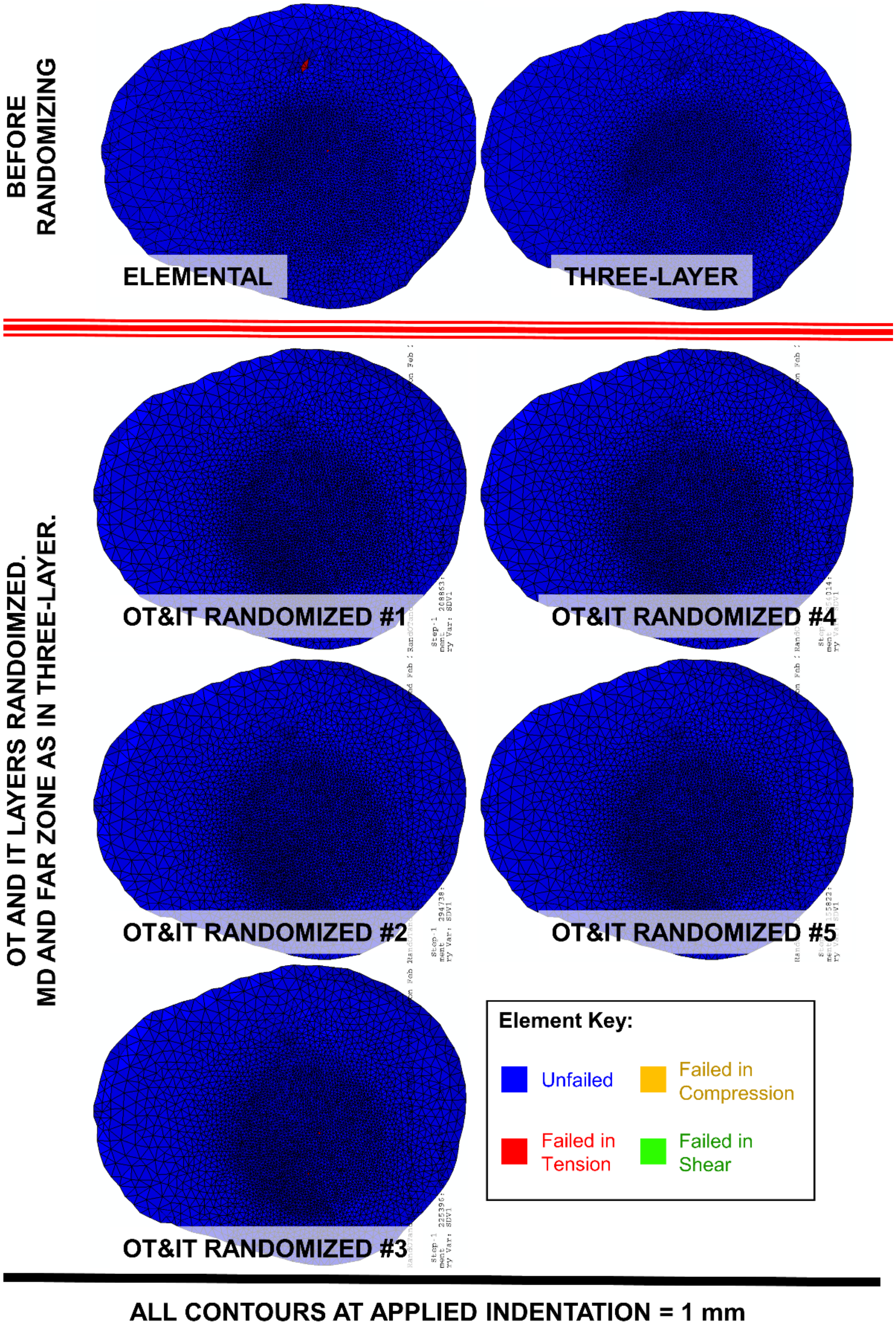

Fig. B-19 BF failure patterns at applied indentation of 1.0 mm (Fig. B-15)

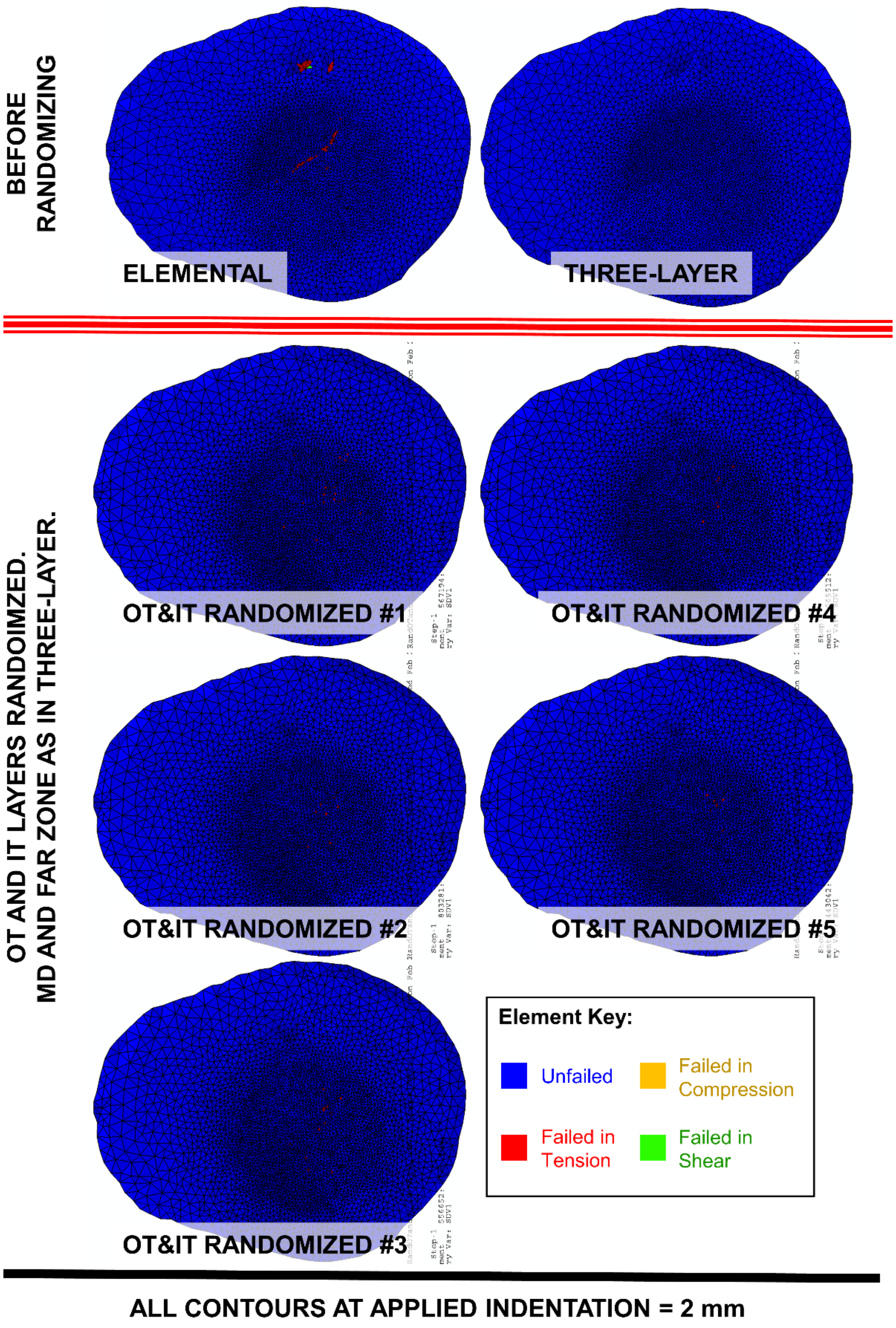

Fig. B-20 BF failure patterns at applied indentation of 2.0 mm (Fig. B-15)

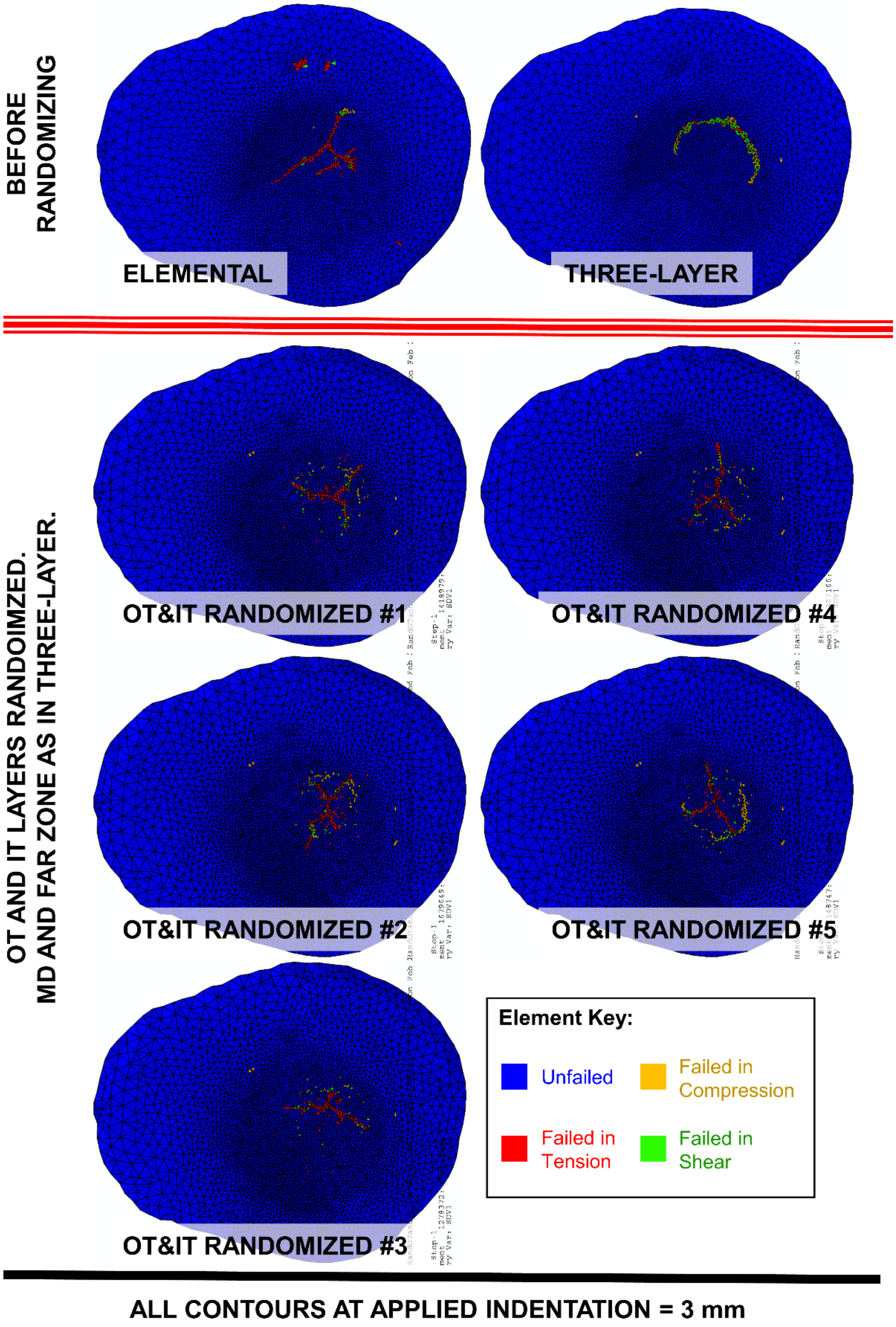

Fig. B-21   BF failure patterns at applied indentation of 3.0 mm (Fig. B-15)

List of Symbols, Abbreviations, and Acronyms

3-D	three-dimensional
AZ	action zone
BF	back face
BFD	back-face deformation
BHBT	behind-helmet blunt trauma
BVF	bone volume fraction
CT	computed tomography
DIC	digital image correlation
FE	finite element
FZ	far zone
HEMC	hybrid experimental modeling computational
IT	inner table
MD	mid-diploe
MIMB	microstructurally inspired mechanism based
MIS	Mimics Innovation Suite
NE	northeast
NW	northwest
OSS	Original Skullcap Simulation
OT	outer table
POI	point of indentation/impact
SE	southeast
SW	southwest
TBI	traumatic brain injury
TFHB	tension-failed-high-BVF (elements)

1 DEFENSE TECHNICAL
(PDF) INFORMATION CTR
DTIC OCA

1 DEVCOM ARL
(PDF) FCDD RLD DCI
TECH LIB

11 DEVCOM NATICK SOLDIER
(PDF) SYSTEMS CTR
M G CARBONI
D COLANTO
R DILLALLA
B FASEL
J FONTECCHIO
B KIMBALL
J KIREJCZYK
J PARKER
M MAFEO
M MARKEY
D PHELPS

3 PROG EXECUTIVE OFC
(PDF) SOLDIER
J HOPPING
J MULLENIX
D OTTERSON

1 US ARMY TEST AND
(PDF) EVALUATION COMMAND
A FOURNIER

1 MTRL SCIENCES DIV
(PDF) LAWRENCE BERKELY
NATL LAB
R RITCHIE

5 SOUTHWEST RSRCH INST
(PDF) C ANDERSON JR
S CHOCRON
D NICOLELLA
T HOLMQUIST
G JOHNSON

2 NIST
(PDF) A FORSTER
M VANLANDINGHAM

1 INST FOR DEFNS ANLYS
(PDF) Y MACHERET

3 MRMC DOD BLAST INJURY
(PDF) RSRCH PROGRAM COOR OFC
R GUPTA
T PIEHLER
R SHOGE

2 MRMC JTAPIC PRGM OFC
(PDF) W LEI
J USCILOWICZ

1 WIAMAN PMO
(PDF) K LOFTIS

4 US ARMY AEROMEDICAL
(PDF) RSRCH LAB
F BROZOSKI
V CHANCEY
B MCENTYRE
D WISE

1 DEVCOM GROUND VEHICLE
(PDF) SYSTEMS CENTER
R SCHERER

1 DEVCOM
(PDF) AMSRD PE
D RUSIN

2 DEVCOM CHEMICAL
(PDF) BIOLOGICAL CENTER
M HORSMON
N VINCELLI

1 OSD DOT&E
(PDF) J IVANCIK

5 US NAVAL RESEARCH
(PDF) LABORATORY
A BAGCHI
A ILIOPOULOS
J MICHOPOULOS
K TEFERRA
X TAN

3 DEVCOM DAC
(PDF) FCDD DAS LBW
G DIETRICH
FCDD DAS LBE
J GURGANUS
S SNEAD

2 DEVCOM ATLANTIC
(PDF) S COLEMAN
H PIETSCH

97 DEVCOM ARL
(PDF) FCDD RLD
J RIDDICK
FCDD RLD E
A EIDSMORE
FCDD RLD FR
M TSCHOPP
FCDD RLH BA
A DAGRO
T THOMAS
FCDD RLR
D STEPP
FCDD RLR EN
R ANTHENIEN
FCDD RLW
S KARNA
J NEWILL
A RAWLETT
S SCHOENFELD
J ZABINSKI
N ZANDER
FCDD RLW B
R BECKER
J CAMPBELL
P GILLICH
C HOPPEL
B SCHUSTER
A TONGE
L VARGAS-GONZALEZ
FCDD RLW M
R BRENNAN
E CHIN
FCDD RLW MA
T BOGETTI
T PLAISTED
J SANDS
E WETZEL
M YEAGER
C YEN
FCDD RLW MB
G GAZONAS
B LOVE
P MOY
D O'BRIEN
J SIETINS
J SUN
T WALTER
FCDD RLW MC
R JENSEN
FCDD RLW MD
A BUJANDA
B CHEESEMAN
K CHO
J LA SCALA
S WALSH
FCDD RLW ME
J LASALVIA
P PATEL
S SILTON
J SWAB
FCDD RLW MF
K DARLING
S GRENDAHL
C HAINES
H MURDOCH
FCDD RLW MG
J ANDZELM
J LENHART
R MROZEK
FCDD RLW S
A WEST
FCDD RLW T
R FRANCART
J HOGGE
FCDD RLW TA
S BILYK
FCDD RLW TB
S ALEXANDER
T BAUMER
A BROWN
B FAGAN
A GOERTZ
A GUNNARSSON
C HAMPTON
M KLEINBERGER
E MATHEIS
J MCDONALD
P MCKEE
K RAFAELS
S SATAPATHY
M TEGTMEYER
T WEERASOORIYA
S WOZNIAK
T ZHANG
FCDD RLW TC
J CAZAMIAS
D CASEM
J CLAYTON
C MEREDITH
L SHANNAHAN
J LLOYD
FCDD RLW TD
R DONEY
R GUPTA
DS KLEPONIS
B KRZEWINSKI
K MASSER
C RANDOW
M ZELLNER
FCDD RLW TE
M LOVE
P SWOBODA

FCDD RLW TF
T EHLERS
P JANNOTTI
L MAGNESS
C MEYER
D SCHEFFLER
FCDD RLW TG
N GNIAZDOWSKI
S KUKUCK
FCDD RLW V
F HUGHES
FCDD RLW VB
A HALL
FCDD RLW W
T V SHEPPARD
FCDD RLW WE
T G BROWN

4 WHITING SCHOOL OF
(PDF) ENG
JOHNS HOPKINS UNIV
KT RAMESH
T D NGUYEN
B NOTGHI
S BAILOOR

5 GEORGIA INST OF TECH
(PDF) S KALIDINDI
S MARGULIES
D MCDOWELL
N THADHANI
M ZHOU

1 DEPT OF ENGRNG SCI AND
(PDF) MECHANICS
VIRGINIA POLYTECHNIC
INST AND STATE UNIV
R BATRA

3 MASSACHUSETTS INST OF
(PDF) TECHLGY
INST FOR SOLDIER
NANOTECHNOLOGIES
R RADOVITZKY
C SCHUH
S SOCRATE
M J BUEHLER

1 DEPT OF MECHL AND
(PDF) NUCLEAR ENGRNG
THE PENNSYLVANIA
STATE UNIV
R KRAFT

1 INDIAN INST OF TECH
(PDF) R BHARDWAJ

2 CENTER FOR APPLIED
(PDF) BIOMECHANICS
UNIV OF VIRGINIA
R SALZAR
M B PANZER

1 UCSD MAT SCI AND ENG
(PDF) MARC MEYERS

1 DUKE UNIV
(PDF) BIOMED ENG
CR BASS

1 UNIV OF CAPE TOWN
(PDF) BLAST IMPACT &
SURVIVABILITY UNIT
TJ CLOETE

1 UNIV OF OXFORD
(PDF) BLAST IMPACT
& SURVIVABILITY UNIT
C SIVIOUR

1 UNIV OF CAMBRIDGE
(PDF) ENG DEPT
V DESHPANDE

4 UNIV OF SOUTH CAROLINA
(PDF) COL OF ENG
S RAJAN
M SUTTON
S SOCKALINGAM
F THOMAS

1 IMPERIAL COL LONDON
(PDF) DEPT OF PHYSICS
W PROUD

1 DIV OF ENG AND APPL SCI
(PDF) CALTECH
R RAVICHANDRAN

1 DEPT OF AERO ENG AND
(PDF) ENG MECH
U TEXAS AUSTIN
K RAVI-CHANDAR

1 AERO AND ASTRO ENG
(PDF) PURDUE UNIV
W CHEN

1 DEPT OF NEUROSURGERY
(PDF) MED COL OF WISCONSIN
N YOGANANDAN

1 SANDIA NATL LAB
(PDF) B SANBORN

1 WOLFSON SCHOOL OF
(PDF) MECHANICAL, ELECTRICAL,
AND MANUFACTURING ENG
LOUGHBOROUGH UNIV
V SILBERSCHMIDT

1 DEPT OF MECH AND AERO
(PDF) ENG
CASE WESTERN RESERVE
UNIV
V PRAKASH

1 MATERIALS SCI AND ENG
(PDF) UNIV OF DELAWARE
J GILLESPI

1 SIBLEY SCHOOL OF MECH
(PDF) AND AERO ENG
CORNELL UNIV
S L PHOENIX

1 DEPT OF MECH SCI AND ENG
(PDF) UNIV OF ILLINOIS URBANA-
CHAMPAIGN
I CHASIOTIS

1 DEPT OF MECH ENG
(PDF) UC SANTA BARBARA
S DALY

1 CENTER FOR BIOENG AND
(PDF) BIOTECH
UNIV OF WATERLOO
D CRONIN

1 DEPT OF MECH ENG
(PDF) UNIV OF ALBERTA
J HOGAN

2 LOS ALAMOS NATL LAB
(PDF) E BROWN
G GRAY